POLITECNICO

MILANO 1863

SCUOLA DI INGEGNERIA INDUSTRIALE
E DELL'INFORMAZIONE

Multiphysics analysis of accidental transients for a Molten Salt Fast Reactor

TESI DI LAUREA MAGISTRALE IN
NUCLEAR ENGINEERING - INGEGNERIA NUCLEARE

Author: **Sophie Deanesi**

Student ID: 964463
Advisor: Prof. Stefano Lorenzi
Co-advisors: Prof. Antonio Cammi
Academic Year: 2021-22

Acknowledgements

Special thanks are devoted to Prof. Stefano Lorenzi and Prof. Antonio Cammi, for the support provided during this thesis, the advice, and the patience to answer all the questions that an engineer prefers to keep secret.

A Nietta,
a Bruno,
a Mingo,
e a Milena.

Abstract

The Molten Salt Fast Reactor is the concept chosen in the context of the Generation-IV International Forum (GIF-IV) as representative of the liquid-fueled reactors, since it complies with the goals of sustainability, safety, and proliferation resistance. The peculiarities intrinsic to the circulating fuel result in a deep interplay between neutronics and thermal-hydraulics. This feature motivated a growing interest in implementing numerical simulations to inspect the reactor behaviour coupling in the same environment all the physics involved. In this context, the OpenFOAM toolkit proved to be a suitable tool to investigate the MSFR behaviour through solvers suitable for nominal steady state and transient conditions.

This thesis embraces the multiphysics approach and the objectives of the Horizon 2020 Euratom SAMOSAFER project. The ultimate objective is to assess the conditions on the containment of the MSFR and also the dynamic response of the reactor to accidental scenarios meant to explore the time evolution of the main operational parameters during unintended transients. The case study consists of a 3D domain representing a 16th of the primary loop of a MSFR. The latter is simulated with solvers that couple the incompressible single-phase Reynolds-Averaged Navier-Stokes equations with a multi-group neutron diffusion approximation, along with transport equations for delayed neutron and decay heat precursors. The first part of this thesis focuses on the steady state assessment of the nominal operating condition of the reactor. Furthermore, sensitivity analyses span over different modelling choices intrinsic to the numerical approach, starting from mesh and geometry, then to the turbulence modelling, and finally with sources and boundary conditions. The thesis proceeds with the simulations of the accidental scenarios. Firstly, a failure involving the primary pumps, namely an Unprotected Loss of Fuel Flow, is simulated and analysed in detail. Then, the degradation of the heat removal is investigated in two scenarios for an Unprotected Loss of Heat Sink. The final part of this work presents a preliminary verification of a transient solver coupled with the melting and solidification phenomena modelling, which is of interest in relation to the safety barriers of the freezing valves.

Abstract in lingua italiana

Nell'ambito del Generation-IV International Forum (GIF-IV) i reattori veloci a sali fusi (MSFRs) rappresentano la famiglia di reattori a combustibile liquido, soddisfando gli obiettivi di sostenibilità, sicurezza e non proliferazione. Le caratteristiche insite in un combustibile in movimento si traducono in una profonda interazione tra la neutronica e la termo-idraulica. Ciò si concretizza in un crescente interesse nell'implementare simulazioni numeriche volte ad approfondire il comportamento del reattore, accoppiando nello stesso ambiente le diverse fisiche coinvolte. In tale contesto, OpenFOAM si è dimostrato uno strumento inestimabile per ispezionare il comportamento di un MSFR grazie allo sviluppo di solver adatti a simulare condizioni stazionarie nominali e transitorie.

La tesi proposta abbraccia gli obiettivi del progetto Horizon 2020 Euratom SAMOSAFER così come l'approccio multifisico. Il fine ultimo è quello di valutare le condizioni della funzione di contenimento di un MSFR così come la risposta dinamica del reattore a scenari accidentali volti a apprezzare l'evoluzione temporale dei parametri operativi durante transitori non intenzionali. Il caso studio consiste in una rappresentazione 3D di un sedicesimo del circuito primario di un MSFR. Quest'ultimo viene simulato grazie a solvers che accoppino le equazioni Reynolds-Averaged Navier-Stokes per fluidi incomprimibili monofasici con l'approssimazione multigruppo per la diffusione neutronica ed equazioni di trasporto per i precursori dei neutroni ritardati e del calore di decadimento. La prima parte della tesi si concentra sulla valutazione delle condizioni operative nominali del reattore in stato stazionario. Inoltre, analisi di sensibilità indagano diverse scelte di modellazione intrinseche all'approccio numerico, a partire dalla geometria e dalla mesh, continuando con i modelli di turbolenza e infine con diversi tipi di sorgente e condizioni al contorno. La tesi prosegue con le simulazioni inerenti gli scenari accidentali. In primo luogo, viene simulato un danneggiamento che coinvolga le pompe primarie, o perdita di flusso di combustibile non mitigata (ULOFF). Successivamente, un deterioramento delle proprietà di scambio termico è analizzato attraverso due scenari di perdita del dissipatore di calore (ULOHS). La parte finale del lavoro presenta la verifica preliminare di un solver che includa durante i transitori la modellazione di fenomeni di fusione e solidificazione, di interesse per trattare il comportamento delle innovative valvole di congelamento di sicurezza.

Parole chiave: analisi multifisica, OpenFOAM, MSFR, transitori accidentali

Contents

Introduction

Among the six designs identified by the Generation-IV International Forum (GIF-IV) [1], the Molten Salt Reactors (MSR) stand out for a peculiarity, i.e. the circulating liquid salt, which acts both as fuel and as coolant. This feature is at the heart of the advantages in terms of safety and sustainability, to name a few, but also of the challenges in terms of design, modelling, and operation.

The concept dates back to the 1950s and 1960s, when it was extensively studied at Oak Ridge National Laboratory (ORNL). In 1954, the efforts were directed towards the operation of the Aircraft Reactor Experiment (ARE) in the field of nuclear propulsion of aircraft [2]. The research activities continued with the construction of the Molten Salt Reactor Experiment (MSRE), which was conceived in the thermal neutron spectrum and went critical in 1965. At a later time, the efforts were mostly abandoned, leaving the Molten Salt Breeder Reactor (MSBR) in the design phase, in favour of another reactor type en vogue in the 1970s, namely the Liquid Metal Fast Reactor (LMFR) [3].

Nowadays, the attractiveness has progressively increased again since MSRs meet the goals of the Generation IV International Forum [4], i.e., sustainability, safety and proliferation resistance. The interest stretches from thermal to fast technologies, which can exploit either chloride or fluoride salts. Among the advantages, it is possible to mention the operation at atmospheric pressure, the strong negative feedback coefficients and the avoidance of a large reactivity reserve thanks to the exploitation of on-line fuel reprocessing. This system also allows the adjustment of fuel composition without shutting down the reactor or manufacturing and transporting new solid fuel elements. Furthermore, in terms of sustainability and waste management, it is worth mentioning that the nuclear fuel dissolved in the salt ranges from fissile elements such as UF_4, PuF_3, to minor actinides and/or fertile elements as ThF_4, providing the reactor the flexibility to operate as burner or as breeder. This leads to higher fuel burnups, better resource utilization and the implementation of a closed fuel cycle.

The Molten Salt Fast Reactor (MSFR)

The Molten Salt Fast Reactor (MSFR) is the reference concept chosen by GIF-IV as representative of circulating-fuel reactors [5, 6]. This design was studied in detail at the Centre National de la Recherche Scientifique (CNRS, Grenoble-France) since 2004, then further developed by EVOL Euratom Project [7] and SAMOFAR Project [8]. Subsequently, in 2019 the SAMOSAFER Project [9] started, with the aim of deepening knowledge on the behaviour of innovative safety barriers, such as the freeze plugs and the Emergency Draining System, which allow fuel salt to be discharged in safe storage tanks.

The MSFR can be classified as homogeneous as it is operated by a circulating fluid fuel, in this case in a liquid state, i.e., the molten salt, which also acts as coolant. Moreover, the reactor is characterised by an intermediate-to-fast neutron spectrum, which is softer than that of traditional solid fast reactors, thus implying a strong negative Doppler feedback coefficient. This appreciable feature is even strengthened by the negative thermal expansion coefficient, which is related to the increase of neutron leakages, improving safety and stability. In comparison to solid-fueled reactors, the action of the feedback coefficients is accelerated by direct heat production and release in the fuel [1]. The delayed neutron precursors drift by the fuel is a feature that cannot be disregarded when discussing MSFR. This phenomenon lowers in-core delayed neutron fraction and poses challenges for control and safety since this parameter is related to the promptness of the reactor to respond to external perturbations.

The system consists of a total primary volume of 18 m^3 of molten salt moving upward in a toroidal shaped reactor, freed from structural material or moderator thanks to the peculiarities of the MSFR technology. For neutronic reasons, the choice was initially centred on a square-cylinder, but computational fluid-dynamics (CFD) simulations performed in the context of the EVOL Project revealed an unacceptable salt recirculation trend. As a result, with ongoing profile improvements, a toroidal-shape is the preferred option. The fuel extracted from the top of the homogeneous core is forced through sixteen outer loops, composed by a system of pump and heat exchanger, which delivers the thermal power to an intermediate salt loop, prior to the power conversion loop. On top and bottom, nickel-based alloy reflectors surround the reactor to improve neutron economy and prevent neutron leakages. The shielding function of these components is enhanced by a layer of B_4C. Radially, a fertile blanket, composed mainly by LiF-based fertile salt, improves the breeding capability of MSFR.

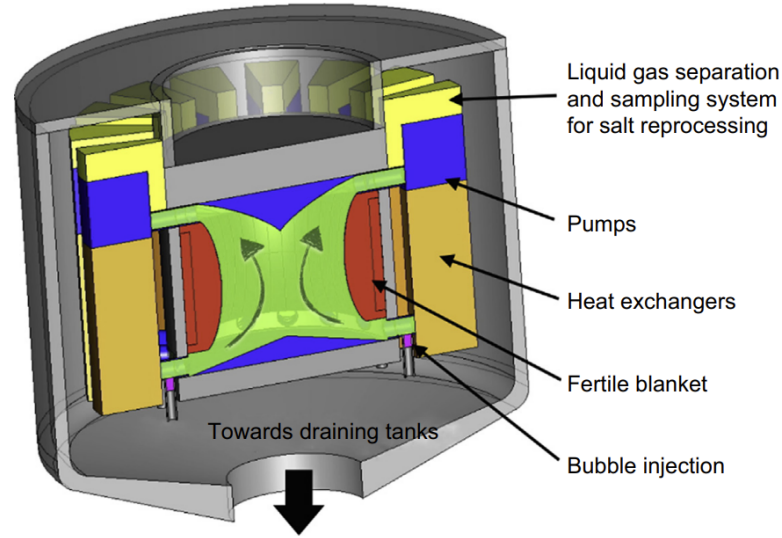In Fig.1 a schematic view of the system is presented.

Figure 1: Schematic representation of the reference MSFR fuel circuit [4].

Thermal Power	3000 MW$_{th}$
Mean fuel salt temperature	700 °C
Fuel salt temperature increase in the core	100 °C
Fuel salt melting point	565 °C
Total primary volume	18 m^3
Core Height	2.25 m
Core Diameter	2.25 m
Nominal flow rate	4.5 m^3/s
Fuel composition 1: ^{232}Th-^{235}U-^{238}U-TRUs (adopted in the thesis)	
LiF	77.5 mol%
$^{232}ThF_4$	20.0 mol%
$^{233}UF_4$	2.5 mol%
Fuel composition 2: ^{232}Th-^{233}U	
LiF	77.5 mol%
$^{232}ThF_4$	6.6 mol%
$^{235}UF_4/^{238}UF_4$	12.3 mol%
PuF_3	3.15 mol%
NpF_3	0.23 mol%
AmF_3	0.19 mol%
CmF_3	0.03 mol%

Table 1: Reference characteristics of MSFR [1, 3].

It is crucial to note that for a MSFR the structural materials are subjected to severe conditions in terms of thermal stresses and irradiation [10]. These loads need to be carefully accounted for in the design phase, considering the high working temperatures and the direct contact of the fuel with the structures. In this context, the assessment of the working conditions proves to be essential both in nominal conditions and during accidental transients.

For what concern operational reference parameters, the high boiling point of salt allows the reactor to operate at atmospheric pressure, while the mean core temperature is set around 700°C and the target power to 3 GW_{th}. The salt under consideration is an eutectic mixture of ^7LiF 77.5 mol% and $^{232}ThF_4$ 22.5 mol% combined with other heavy nuclei fluorides. The actinide inventory with lower radiotoxicity is added to the other advantages of thorium in the context of sustainability. In regards of the fissile contribution, ^{233}U as well as a mixture of enriched $^{235}U/^{238}U$ and transuranics (TRUs) can be exploited.

For more details, the reader is referred to Table 1.

The MSFR is equipped with an online chemical reprocessing unit which diverts 40 liters/day of fuel in order to clean it up, removing fission products, and to keep under control the fuel composition. The helium bubbling system, studied in detail in last few years [3], can also accomplish the function of removing fission products, either gaseous or solid precipitates, via capillarity sticking to the bubbles.

The safety function is delivered also thanks to draining tanks, meant to accommodate the liquid fuel, discharged by gravity, both in normal maintenance and accidental scenarios through an active cooled temporary storage or in a criticality-safe tank, respectively. The latter is part of the Emergency Drain System, whose opening devices show great potential for satisfying the passive safety objective. Indeed, there is the opportunity to design the freezing plugs, made from the same salt as the reactor and positioned in a portion of the draining pipes, such that they melt in case of loss of power or overheating, ensuring a fast draining of the circulating fuel salt in the safe tank.

Objectives and outline of the thesis

The work presented in this thesis embraces the objectives of the Horizon 2020 Euratom SAMOSAFER project [9] of assessing and demonstrating the feasibility of the reactor concept in terms of compliance with safety limits during severe accidents. The main focus of the work is to investigate the behaviour of the reactor in nominal operating conditions and accidental scenarios, as well as to assess the conditions on the containment of the

MSFR. The aim lies in characterising the harsh working conditions to which the reactor is subjected in terms of thermo-mechanical loads and irradiation. In this light, multiphysics simulations seem suitable tools to treat the deep coupling intrinsic to the circulating fuel MSFR. Furthermore, the OpenFOAM toolkit and the use of 3D geometry provide the flexibility to investigate different modelling choices. This results in the possibility of studying the flow structures developed inside the core as well as the most critical points subjected to severe conditions and the design optimisations performed on geometry. Furthermore, solving the thermal-hydraulic and neutronic problems during transient events allows to appreciate the evolution of operational variables triggered by an unwanted event. All these factors provide a valuable resource in the design phase and in the safety assessment of the reactor. Indeed, the compliance with the safety limits imposed by the performance degradation of structural materials can be verified during these transients. Finally, the multiphysics approach allows to extend of the accidental shortlist that can be analysed by incorporating in the solver the modelling of melting and solidification phenomena. The effort in coupling the phase change models is strictly related to the opportunity to deepen the knowledge on the behaviour of the freeze valves. A coupled solver leads to simulating in the same case study an accidental event, involving, for example, the failure of a primary loop component, and at the same time the response of the safety barrier of freeze plugs.

To achieve these goals, numerical simulations are run to reproduce the salt behaviour in a 16th of the MSFR. The 3D domain involves the main components of the primary loop, namely, the core, the hot and cold legs, the pump, and the heat exchanger. The simulations are run thanks to the open source OpenFOAM version 8 toolkit and the multiphysics solvers developed at the Politecnico di Milano [11, 12], which solve the thermal-hydraulics and neutronic problems in the same environment. An incompressible single-phase solver is coupled with the multi-group neutron diffusion approximation, as well as transport equations for delayed neutrons and decay heat precursors. Two versions are available: the *msfrSimpleFoam* solver for steady state simulation of nominal operating conditions and *msfrPimpleFoam* for transients, where the focus is on the dynamic behaviour of the reactor. In addition, in this work, a new solver is developed coupling the transient solver with solidification and melting models, also implemented at the Politecnico di Milano [13].

The remainder of this thesis is organised as follows. First, Chapter 1 presents a brief overview of the state of the art. Then, a detailed description of OpenFOAM solvers follows, along with a description of the physics coupled according to the multiphysics approach. Appendix A provides a brief description of the characteristics of the OpenFOAM toolkit, while Appendix B details the constants characterising the equations solved in the neutronic part of the solvers. Then, Chapter 2 is focused on the steady state simulations

run to get the distributions of variables in the nominal conditions at which the reactor is operated. Furthermore, sensitivity analyses are performed in order to investigate the modelling choices intrinsic to the numerical approach. In Chapter 3, the first accidental scenario is illustrated, and the choice lies with a failure affecting the primary pumps, i.e., an Unprotected Loss of Fuel Flow. The time profiles of the variables of interest are examined together with the time evolutions of the distributions of the variables, which are evaluated at different instants during the transient. In Chapter 4, the second accidental event is described, and it consists in a degradation of the heat removal provided by the heat exchangers, i.e., an Unprotected Loss of Heat Sink. Two case studies are considered, the former for a more realistic scenario and the latter for a more severe one. Subsequently, the numerical outcomes of both simulations are discussed. Finally, in Chapter 5 a preliminary assessment of the correct implementation of the solver coupling the neutronic and thermal-hydraulics while introducing phase change phenomena is presented along with a simplified case study of a square cavity. In Fig.2, the graphical representation of the thesis is illustrated.
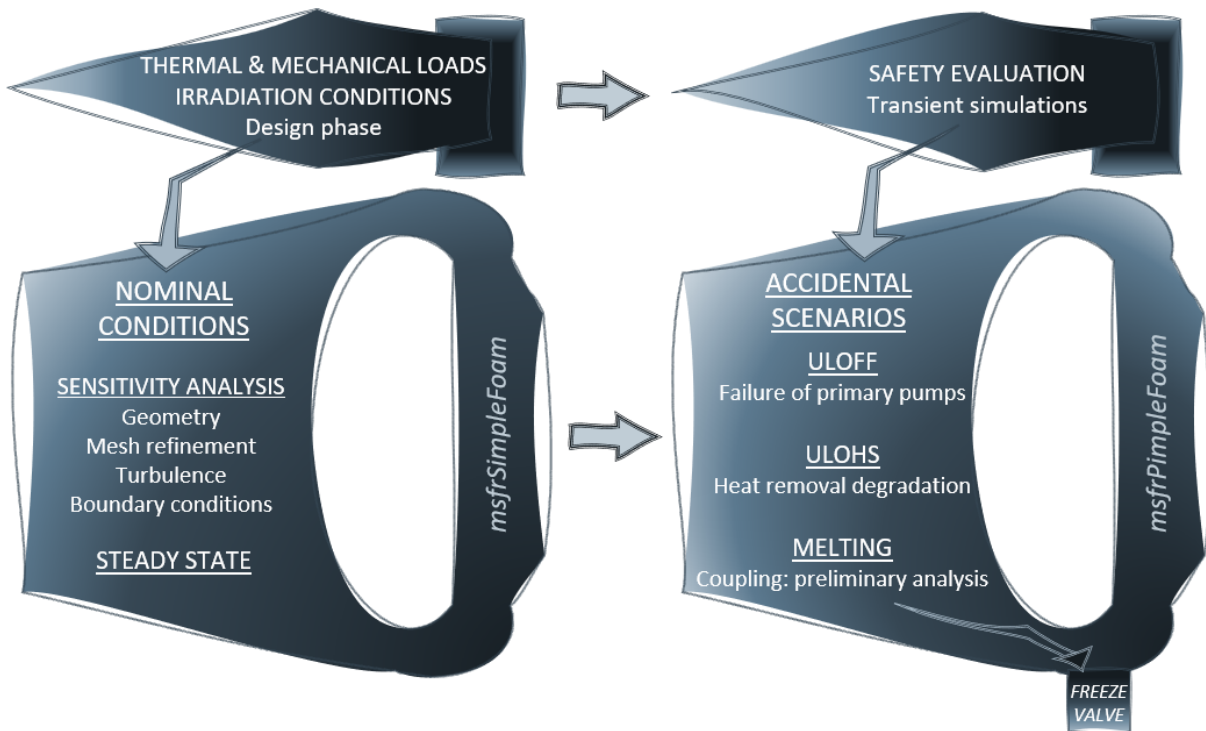

Figure 2: Graphical representation of the outline of the thesis.

1 | Multiphysics Modelling

In the Introduction, the circulating fuel is mentioned as the foundation of the advantages provided by the MSFR technology, but this peculiarity also brings challenges in the context of modelling and simulation. With respect to traditional solid-fuel reactors, which are properly treated with the *operator-split* strategy, the circulating-fuel reactors are characterized by a deeper coupling between thermal-hydraulics and neutronics. The *operator-split* approach involves the solution, in separate codes, of the equations that characterize each physics and the simple external coupling is accomplished, at each time step, through the exchange of outputs of the different monophysics codes, whose connection is enabled by suitable interfaces. In the case of MSFRs, this does not guarantee a proper treatment of the nonlinearities [14] that arise from the transport of delayed neutron precursors by the fuel or from the fission energy production directly in the coolant, as well as the strong negative feedback coefficients, deriving from the thermal effects on the fuel. The relevance of resolving these phenomena gave rise to huge research efforts aimed at implementing in an unique environment the coupling between thermal-hydraulics and neutronics. An overview will be presented in Section 1.1. Among all the solvers and multiphysics models developed in recent years, the solvers used in this thesis, along with the subsolvers for different physics, are described in the following Sections 1.2, 1.3, 1.4 and 1.5.

1.1. State of the art

In this section, an outline of the state of the art runs through the steps that succeed each other in the development of increasingly comprehensive modelling of MSFRs, with the objective of facing the inaccuracies intrinsic in the traditional *operator-split* approach and coupling the different physics in an unique environment in order to appreciate the interplays among phenomena [15].

The first approach combined two lumped parameters models, namely the point kinetics equation and a zero-dimensional thermal-hydraulic model of the reactor. This model focused on the influence of the fuel motion on delayed neutron precursors drift, but such a

preliminary implementation lacked the spatial information fundamental to an exhaustive analysis of a reactor [16]. The 2D axial-symmetric model, developed at Politecnico di Milano and at Delft University of Technology at the same time but with two different codes, compensated for this simplification [17]. Even if this extension enabled to simulate and study the reactor behaviour in steady state and transient scenarios, successfully capturing the phenomena of interest, it was not satisfactory to evaluate the reactor response to asymmetric scenarios and to resolve the flow structures and vorticities characteristic of a MSFR. Consequently, a 3D model seemed the natural prosecution of these works. Starting with a one-speed neutron diffusion approximation to reduce computational load and progressing to a multi-group diffusion approach and, finally, to more accurate transport models, the developed solvers demonstrate to be the appropriate tool for furthering the analyses in various directions [11]. For example, extending the primary loop simulation domain, including the helium bubbling system, by implementing a two-phase solver that can also take into account the compressibility effects of the fuel in fast transient scenarios [3]. Then, it is possible to proceed with the implementation of the fission products' behaviour, whether gaseous, e.g., Xenon [18], or solid, e.g., metallic, with their associated transport and deposition problems [19, 20]. Another path is to keep the primary loop structure simulated as simple as possible while strengthening knowledge in safety assessment in terms of the feedback dynamic response of the reactor in accidental scenarios or including the safety barriers and modelling the innovative freezing plugs, for example, implementing models to represent solidification and melting phenomena, as it is done in the context of the SAMOSAFER project [9, 13]. Furthermore, it is crucial that these research efforts do not remain isolated, given the possibility to compare the results thanks to agreed-upon benchmark cases [21].

1.2.   Multiphysics solvers

The multiphysics solvers adopted in this thesis, developed with the OpenFOAM toolkit, are *msfrSimpleFoam* and *msfrPimpleFoam*. The difference is related to the standard algorithms at the basis of thermal-hydraulics part, i.e SIMPLE and PIMPLE, and they are employed to solve steady state and transient conditions, respectively. The Boussinesq approximation is expected to account for buoyancy effects in both cases. Concerning the neutronics, a multi-group diffusion method is implemented in both solvers [12].

In Fig.1.1 the structure of the solver is shown. Each main block contains a characteristic equation for a given variable, which OpenFOAM solves once at a time. Starting from the thermal-hydraulic part, the conservation equations are solved for velocity, pressure

and energy. Subsequently, the neutronic block solves for fluxes, delayed neutron and decay heat precursors. The volumetric power source, obtained once fluxes and decay heat precursors are known, is fed to the energy equation to get new values of temperature and density fields. These outputs allow to update the value of cross sections. In order to to ensure convergence in each cycle along with the coupling between different physics OpenFOAM employs Picard iterations. In the outer cycle, the variables exchanged from thermal-hydraulics to neutronics are the density and temperature fields, which are used to update the neutronic cross sections and, in the opposite direction, the power density distribution enables the update of temperature.
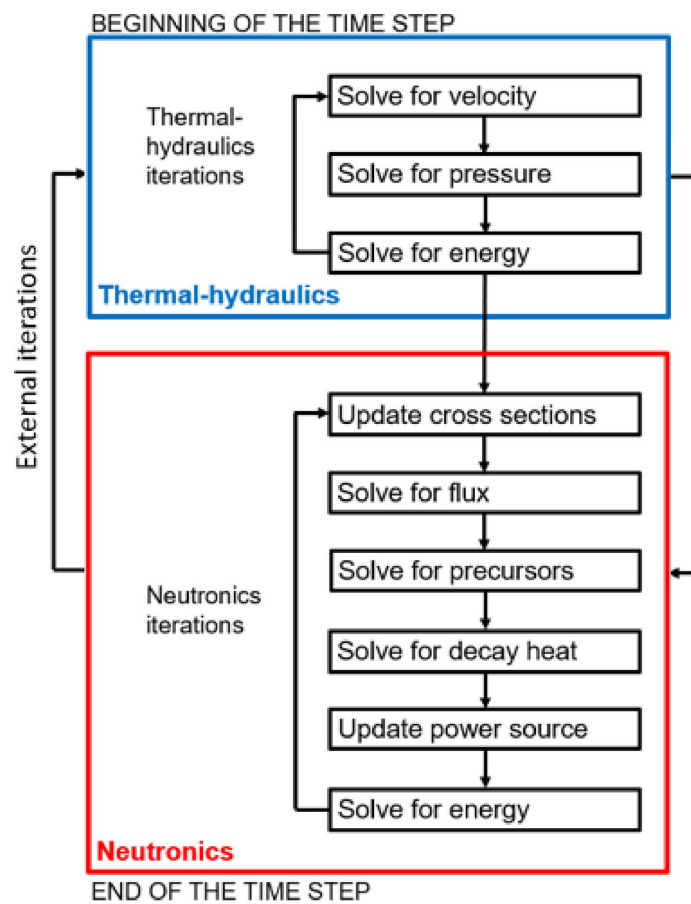

Figure 1.1: Coupling strategy and structure of the solver [21].

The combination of solving one equation at time together with coupling strategy through Picard iterations guarantees the correct solution of coupled equations within an unique time step, catching properly the nonlinearities.

1.3.   Thermal-hydraulics subsolver

The thermal-hydraulics contribution to the problem is expressed by the conservation equations for mass, momentum and energy written in form of Reynolds-Averaged Navier-Stokes (RANS) equations. In this thesis, a single-phase flow of incompressible salt, whose pressure, velocity and temperature are the outputs of Eqs. (1.1)(1.2)(1.3), is considered. Provided that the salts thermophysical properties are kept constant, the buoyancy effect is included thanks to the Boussinesq approximation, that is based on a linearization around a reference temperature T_0, through a thermal expansion coefficient β_T in the momentum equation, Eq.(1.2). Moreover, in Eq.(1.3), the volumetric power source, q, is included in order to account for the coupling with neutronics, thanks to prompt and decay heat contribution as well as to enrich the model with other simplified component, for example, mimicking the heat exchanger. The same source or sink term can be added in principle to the momentum equation in order to represent the pump.

$$\nabla \cdot \boldsymbol{u} = 0 \tag{1.1}$$

$$\frac{\partial \boldsymbol{u}}{\partial t} + \nabla \cdot (\boldsymbol{u}\boldsymbol{u}^T) = -\frac{1}{\rho}\nabla p + [1 - \beta_T(T - T_0)]\boldsymbol{g} + \nabla \cdot [\nu_{eff}(\nabla \boldsymbol{u} + (\nabla \boldsymbol{u})^T)] \tag{1.2}$$

$$\frac{\partial T}{\partial t} + \nabla \cdot (\boldsymbol{u}T) = \nabla \cdot (\alpha_{eff}\nabla T) + \frac{q}{\rho c_p} \tag{1.3}$$

The RANS approach allows to exploit models for turbulence and wall functions already available in the OpenFOAM environment, such as two-equations eddy-viscosity models. In Chapter 2, a sensitivity analysis on the turbulence models is performed. In the previous equations, the effective thermal and momentum diffusivity are expressed as the sum between a laminar and a turbulent term:

$$\nu_{eff} = \nu + \nu_T \tag{1.4}$$

$$\alpha_{eff} = \alpha + \alpha_t = \frac{\nu}{Pr} + \frac{\nu_t}{Pr_t} \tag{1.5}$$

As previously mentioned, two versions of the multiphysics solver are employed in this work, i.e *msfrSimpleFoam* and *msfrPimpleFoam*. The difference between them lays in the algorithm for pressure-velocity coupling, pre-implemented by OpenFOAM, respectively, SIMPLE or PIMPLE. The former is intended to solve steady state simulations, the latter is suitable for transient cases. The solvers deal with a system of equations in a segregated fashion, i.e., once at time, and proceed through successive substitution of solved variables

in the subsequent equation while implementing correction strategies that derive from a proper rewriting of the starting equations. The PIMPLE exploits the SIMPLE algorithm incorporating an inner loop, known as the PISO loop, which improves the accuracy of evaluating time derivatives along with the variables themselves.

1.4. Neutronics subsolver

In order to represent the neutronic contribution while ensuring a good compromise between accuracy and computational load, the multi-group neutron diffusion approximation is adopted. Specifically, each gth group is described by an equation in the form of Eq.(1.6).

$$\frac{1}{v_g}\frac{\partial \varphi_g}{\partial t} = \nabla \cdot (D_{n,g} \nabla \varphi_g) - \Sigma_{a,g}\varphi_g - \sum_{h \neq g} \Sigma_{s,g \rightarrow h}\varphi_g + (1-\beta)\chi_{p,g}\bar{\nu}_g\Sigma_{f,g}\varphi_g + S_g \qquad (1.6)$$

The S_g source represents the explicit terms from the prompt fission neutrons born in other energy groups, the scattered ones into the group of interest, and the delayed neutron precursors.

$$S_g = S_d\chi_{d,g} + S_{n,g}(1-\beta)\chi_{p,g} + S_{s,g} \qquad (1.7)$$

The complete expression of these terms is represented in Eqs.(1.8), (1.9) and (1.10). The presence in the gth equation of a neutron flux belonging to another energy group requires an iterative solution among the groups, which in this case is implemented in a segregated fashion.

$$S_d = \sum_k \lambda_k c_k \qquad (1.8)$$

$$S_{n,g} = \sum_{i \neq g} \bar{\nu}_i \Sigma_{f,i}\varphi_i \qquad (1.9)$$

$$S_{s,g} = \sum_{i \neq g} \Sigma_{s,i \rightarrow g}\varphi_i \qquad (1.10)$$

In order to circumscribe the computational domain to the fuel circuit only, albedo boundary conditions mimic the presence of the upper and lower reflectors and of the blanket. These boundary conditions are expressed in terms of the ratio of outgoing and incoming neutron currents, α_g, when dealing with neutron diffusion equations.

$$D_{n,g}\nabla\varphi_g = -\frac{1}{2}\left(\frac{1-\alpha_g}{1+\alpha_g}\right)\varphi_g \qquad (1.11)$$

The problem also involves the treatment of delayed neutron precursors, subdivided again into groups, through transport equations in the form of Eq.(1.12).

$$\frac{\partial c_k}{\partial t} + \nabla \cdot (\boldsymbol{u} c_k) = \nabla \cdot (D_{eff} \nabla c_k) - \lambda_k c_k + \beta_{d,k} \sum_g \bar{\nu}_g \Sigma_{f,g} \varphi_g \qquad (1.12)$$

In order to consider the drift of precursors induced by liquid fuel motion, transport and diffusion terms are included in the equation. Because the turbulence diffusion effects may be non negligible [11], the diffusion coefficient, D_{eff}, contains both the Schmidt and the turbulent Schmidt numbers, Eq.(1.13).

$$D_{eff} = D + D_t = \frac{\nu}{Sc} + \frac{\nu_t}{Sc_t} \qquad (1.13)$$

The decay heat precursors are treated mostly in the same way, Eq.(1.14). The substantial difference consists of the fact that the decay heat precursors concentration is multiplied by the average energy released per fission, thus implying a unit of measure of J/m^3, while for the delayed neutron precursors the equation is solved for the pure concentration, m^{-3}. For more details about the constants characterizing Eqs.(1.12) and (1.14) the reader is referred to Appendix B.

$$\frac{\partial d_l}{\partial t} + \nabla \cdot (\boldsymbol{u} d_l) = \nabla \cdot (D_{eff} \nabla d_l) - \lambda_{h,l} d_l + \beta_{h,l} \sum_g \bar{E}_{f,g} \Sigma_{f,g} \varphi_g \qquad (1.14)$$

The choice of writing the decay heat precursors concentration in J/m^3 leads to a straightforward form of volumetric heat source split into prompt and delayed contributions, Eq.(1.15).

$$q = (1 - \beta_h) \sum_g \bar{E}_{f,g} \Sigma_{f,g} \varphi_g + \sum_l \lambda_{h,l} d_l \qquad (1.15)$$

The volumetric heat source constitutes the coupling path from neutronic to thermal-hydraulics. The other way around, temperature and density act simultaneously on the macroscopic cross sections in order to account for the thermal feedbacks on neutronics.

A linear term to account for density variation, coherently with the Boussinesq approximation, and a logarithmic term to represent the Doppler effect correct the reference value $\Sigma_{r,g}^0$ for a generic reaction r and g^{th} group. A similar method is used to adjust the intra-group neutron diffusion coefficients, $D_{n,g}$ in Eq.(1.6). The group constants and the coefficients in Eq.(1.16), evaluated for a reference temperature T_0^Σ, are calculated using the JEFF-3.1.1 cross section library [22] in Monte Carlo reactor physics and burnup code

Serpent 2 [23].

$$\Sigma_{r,g} = (\Sigma_{r,g}^0 + A_{r,g}^0 log \frac{T}{T_0^\Sigma}) \frac{1 - \beta_T(T - T_0)}{1 - \beta_T(T_0^\Sigma - T_0)} \tag{1.16}$$

The steady state version of the neutronics subsolver is provided with a power iteration routine to evaluate the multiplication factor. The routine allows to solve the k-eigenvalue problem [24] by setting the time derivatives to zero and dividing the mean number of neutron produced per fission by k_{eff}. This value is updated iteratively in order to achieve criticality at the desired power level specified by the user.

1.5. Melting subsolver

A notable effort was made at Politecnico di Milano to model melting and solidification phenomena, with the aim of providing an insight into the behaviour of freeze valves, of interest as safety mechanisms in the MSFRs [13]. The melting and solidification phenomena are introduced in the solver by considering the two main characterising aspects of phase change, i.e., the latent heat and the velocity transition. Among all possible strategies developed to deal with such complex phenomena, since the phase transition is a multiscale and highly nonlinear problem, the modelling choice lies with a group of models known as *fixed grid* models thanks to their simplicity and reasonable accuracy. In these models, the melting interface is not reconstructed explicitly but it is smeared out in a region called *mushy zone*, which accounts for the presence of both the solid and liquid phases at the same time. Even though this description performs well for non-isothermal transitions, by suppressing the *mushy zone* in a small interval, it can also be applied to isothermal phenomena. This is useful since the molten salt is considered an eutectic mixture, thus belonging to the latter type of phase transitions. Another peculiarity of *fixed grid* models is that they allow for the treatment of latent heat under the *continuum mixture theory*. This means that the two phases are handled as separate subsystems, and the mixture properties are the result of properly weighting the properties of each individual phase. For example, the density ρ and the specific enthalpy h of the mixture are linked to the properties of the single phases through the mass liquid fraction f and the volume liquid fraction g, respectively, Eqs.(1.17) and (1.18).

$$\rho = g\rho_l + (1 - g)\rho_s \tag{1.17}$$

$$h = fh_l + (1 - f)h_s \tag{1.18}$$

In this work the thermophysical properties of each phase are considered temperature invariant, so setting the melting temperature T_m as reference temperature, the specific enthalpy of each phase can be written as:

$$h_s = c_{p,s}(T - T_m) \tag{1.19a}$$

$$h_l = c_{p,l}(T - T_m) + L \tag{1.19b}$$

Thanks to the relations presented in (1.17),(1.18), (1.19a) and (1.19b), the volumetric enthalpy H is derived.

$$H = \rho h = g\rho_l c_{p,l}(T - T_m) + g\rho_l L + (1 - g)\rho_s c_{p,s}(T - T_m) \tag{1.20}$$

The volumetric enthaply plays a major role in the energy conservation equation, which can be written in a temperature based form including the convective and conductive terms as in Eq.(1.21). The partial time derivative of H is at the heart of latent heat modelling.

$$\frac{\partial H}{\partial t} + \nabla \cdot (\rho_l c_{p,l} T \boldsymbol{u}) = \nabla \cdot (k\nabla T) \tag{1.21}$$

Among the models developed at Politecnico di Milano [13], the solver implemented in the current thesis adopts the *Apparent Heat Capacity* and the *Source Term Method* to treat the latent heat and the *Darcy Source Term (DST)* approach to describe velocity transition.

Aside from its simplicity and low computational burden, the *Apparent Heat Capacity* model is considered because it allows for the solution of the energy equation for temperature, in contrast to enthalpy-based methods and coherently with the OpenFOAM solvers used in this work. Rewriting the left hand side of Eq.(1.21) thanks to the chain rule it is possible to identify in the $\frac{\partial H}{\partial T}$ an effective heat capacity, or better *apparent* heat capacity.

$$\frac{\partial H}{\partial t} = \frac{\partial H}{\partial T}\frac{\partial T}{\partial t} \tag{1.22}$$

In particular it is possible to derive Eq.(1.20) for temperature obtaining:

$$\frac{dH}{dT} = \rho_s c_{p,s} + (\rho_l c_{p,l} - \rho_s c_{p,s})(T - T_m)\frac{dg}{dT} + (\rho_l c_{p,l} - \rho_s c_{p,s})g + \rho_l L\frac{dg}{dT} \tag{1.23}$$

This apparent heat capacity can be evaluated from Eq.(1.23) for the previous time-step, with the hypothesis that the time relationship between H and T, e.g., assuming thermal equilibrium, is known.

This method does not require internal iterations,thus implying the benefits of fast-running but it suffers from the drawback of latent heat "peak skipping". In order to explain this issue it is worthwhile to mention that the energy equation requires closing relations between coupled variables, e.g., T and H, in order to deal with non-linearities. In principle, for isothermal transitions the enthalpy shows a linear trend for single phases with a jump at melting temperature, equivalent to latent heat, from the solid to liquid value. Nevertheless, due to numerical instability potentially arising from such a discontinuity, continuous fictitious functions are adopted over a finite small temperature interval, known as *mushy zone*, to represent the phase transition. Without an accurate choice of the width of this interval, dT, the temperature in a cell may skip directly from $T < T - dT$ to $T > T + dT$ or vice versa, avoiding the mushy zone and violating energy conservation. This issue is known as latent heat peak skipping, and it can be prevented by using the appropriate dT or switching to the *Source Term Method*.

The *Source Term Method*, which is again a temperature-based method, focuses on the time derivative of H as a function of g and T, expressed in Eq.(1.20), in the form of:

$$\frac{dH}{dt} = (\rho_l c_{p,l} - \rho_s c_{p,s})\frac{dg}{dt}(T - T_m) + g(\rho_l c_{p,l} - \rho_s c_{p,s})\frac{dT}{dt} + \frac{dg}{dt}\rho_l L + \rho_s c_{p,s}\frac{dT}{dt} \quad (1.24)$$

The simultaneous presence of g and T in Eq.(1.24) and the dependence of g on T imply the need for an iterative procedure. At each ith time step, the values of temperature and liquid fraction are imposed as the ones obtained at the previous iteration $i-1$, the energy equation is solved for T^i and the volumetric liquid fraction is updated as in Eq.(1.25), constraining this value in between 0 and 1.

$$g^i = g^{i-1} + \frac{\rho c_p}{\rho_l L}(T^i - T_m + \epsilon - 2\epsilon g^{i-1}) \quad (1.25)$$

The procedure is iterated until convergence before moving to the next time step. The updating strategy in Eq.(1.25) allows for taking into account different properties for the liquid and solid phases [13, 25]. Despite the fact that the iterative procedure results in a slower method than the *Apparent Heat Capacity* one, the *Source Term Method* brings the advantages of accuracy and robustness and eliminates the problem of latent heat peak skipping.

As previously mentioned, the nonlinearities caused by the coupled variables in the problem are managed thanks to closure relations with fictitious continuous function to smear out the isothermal phase change in the *mushy zone*. Among the closure relations tested at Politecnico di Milano, a sigmoid function relating temperature and mass liquid fraction,

f, for the *Apparent Heat Capacity* method and a linear relation between temperature and volume liquid fraction, g, for the *Source Term Method* will be considered in this thesis.

$$
\begin{cases}
g = 0 & for \ T < T_m - \epsilon \\
g = \dfrac{T - T_m + \epsilon}{2\epsilon} & for \ -\epsilon < T - T_m < \epsilon \\
g = 1 & for \ T > T_m + \epsilon
\end{cases}
\tag{1.26}
$$

where $2\epsilon = dT$.

The other phenomenon that is significant for getting an all-encompassing description of phase change is the velocity transition, which results from different responses to shear stresses in the solid and liquid phases. Referring to the work previously mentioned [13], the mechanical aspects are neglected, but the RANS equations are modified in order to impose a null velocity in the solid phase while maintaining the standard formulation for the liquid phase. The smooth transition is ensured by adopting the *Darcy Source Term* approach, in which the momentum equation is provided with a source, S, that overcomes all other terms for the solid phase, resulting in a null velocity field, while it drops to zero for the liquid phase. This term is presented in Eq.(1.27) where C is a constant ranging from 10^8 to 10^{10} while ϵ prevents from numerical divergence.

$$
S = \frac{(1-g)^2}{(g^3 + \epsilon)} C \nu_l \boldsymbol{u}
\tag{1.27}
$$

1.6.   Update and coupling of the solvers

All the simulations presented in this work are run in OpenFOAM v8. This choice was made since in this version of the toolkit, as opposed to OpenFOAM version 6, it is easier to implement time dependent sources. Therefore, it was necessary to update the solvers with the proper libraries, which, for the sake of brevity, are not reported. When dealing with melting and solidification phenomena, the coupling was ensured thanks to two solvers previously developed at the Politecnico di Milano, i.e., *msfrPimpleFoam* and *meltingPimpleFoam* [11–13, 19]. The neutronic part is left as it is, with the coupling provided by the volumetric heat source introduced in the energy equation and the cross sections updated. The accumulation term in the energy equation is modified in order to incorporate the T-based latent heat models while the momentum equation is enriched with the *Darcy Source Term*. The final solver, referred to as *phaseChangeMsfrPimpleFoam*, will be made more user-friendly since, in its current state, some of the thermal properties have to be input in two distinct files belonging to the original solvers.

2 | Steady state analysis

After the illustration of the tools necessary to deepen the knowledge of the response of circulating liquid fuel reactors in transient accidental scenarios, first of all, it seems worthwhile to analyse the behaviour of the MSFR during normal operation. As a result, numerical simulations on a 3D geometry are performed in this chapter to assess the distributions of variables of interest in steady state conditions. Due to the approximations and modelling choices intrinsic to the numerical approach, in Sections 2.2, 2.3, 2.4, 2.5 and 2.6 sensitivity analyses are exploited to evaluate the influence of geometry and mesh on the outcomes, to test the available pre-implemented sources in the OpenFOAM environment, to assess the effects of turbulence modelling and of neutronic boundary conditions, respectively. In Section 2.7, the reference case is presented together with the results of the steady state analysis that constitute the starting point for the transient simulation in the following Chapters. Finally, in Section 2.8 the thermal feedback coefficient,including both the Doppler and thermal expansion effects, is estimated.

2.1.   The MSFR model

The numerical simulations performed in this Chapter share some characteristics that are enumerated in this first section. Firstly, the thermophysical properties of the salt are summarised in Table 2.1. The nominal power refers to the full core capacity, but since the domain of interest consists of a 3D representation of 1/16th of the reactor, shown in Fig.2.1, the target value in the simulations is fixed at 187.5 MW and imposed thanks to the power iteration routine previously described in Chapter 1. The same consideration can be made for the pump, whose global flowrate is aimed at 4.5 m^3/s but the simulations are set up to reach 0.28125 m^3/s. In contrast to the power, whose value is imposed by the user, the volumetric flowrate is given as an output by the solver and not decided a priori; moreover, this value is strictly related to the parameters that characterise the pump. In a closed circuit where there is not a proper definition of inlet and outlet, the choice of implementing a momentum source rather than fixing a volumetric flow rate is more reasonable. Furthermore, if the value is imposed, the time evolution of the volumetric

flowrate in accidental transient scenarios should be known a priori. As this is not true, it is preferable to feed the simulation with time profiles for the parameters of the momentum source. In transient cases where the full core values are considered more representative, the values of power and volumetric flowrate will be multiplied by 16.

The thermophysical properties of the circulating liquid salt are kept constant and uniform throughout the domain, with the exception of the density contribution in the momentum equation that represents buoyancy effects, as already discussed in Section 1.3. Furthermore, the values of adimensional numbers, namely Sc, Sc_t, Pr, and Pr_t, would necessitate a more precise evaluation; thus, the values are imposed in accordance with other previous works available in the literature [11, 12, 18].

Parameter	Symbol	Value	Units
Nominal Power	Q	3000	MW_{th}
Reference Temperature	T_{ref}	900	K
Flowrate	$\dot{V}$	4.5	m^3/s
Density	ρ	4306.71	kg/m^3
Specific Heat Capacity	c_p	1593.94	J/ kg K
Laminar Viscosity	ν	$5.89 \ 10^{-6}$	m^2/s
Thermal Expansion Coefficient	β	$1.1912 \ 10^{-4}$	1/K
Intermediate Salt Temperature	T_{ext}	908	K
Prandtl Number	Pr	23.87	-
Turbulent Prandlt Number	Pr_t	0.85	-
Schmidt Number	Sc	20	-
Turbulent Schmidt Number	Sc_t	0.85	-

Table 2.1: Reference parameters of molten salt for steady state simulations.

For the neutronic part of the model, six energy groups are implemented for the fluxes in the multi-group diffusion approach, while eight and three groups are selected to represent the delayed neutron precursors and decay heat precursors, respectively. As previously mentioned, for more details about the neutronics data and properties, the reader is referred to Appendix B.

Due to a lack of design specifications for the pump and the heat exchanger, a momentum source and a heat sink are chosen to mimic these components, which are represented by boxes in the 3D geometry. In particular the volumetric heat sink can be expressed as:

$$q = \gamma \left(T_{ext} - T \right) \tag{2.1}$$

where γ (W/m³K) is a tunable parameter that accounts for the global heat transfer coefficient between the primary and intermediate loops and for an effective volume of the heat exchanger, while T_{ext} (K) is a reference temperature of the intermediate loop. The momentum source and the heat sink parameters are adjusted in order to get the desired volumetric flowrate of 4.5 m³/s and a minimum temperature at the core inlet of 923 K.

In Fig.2.1a the zones of the primary loop are shown: in yellow, the pump; in pink, the heat exchanger; in green and red, the hot and cold legs, respectively; and finally, in blue, the core. In Fig.2.1b, an example of the mesh used in the following simulations with ∼1.2 million elements is shown.

(a) Primary loop zones.   (b) Reference mesh.
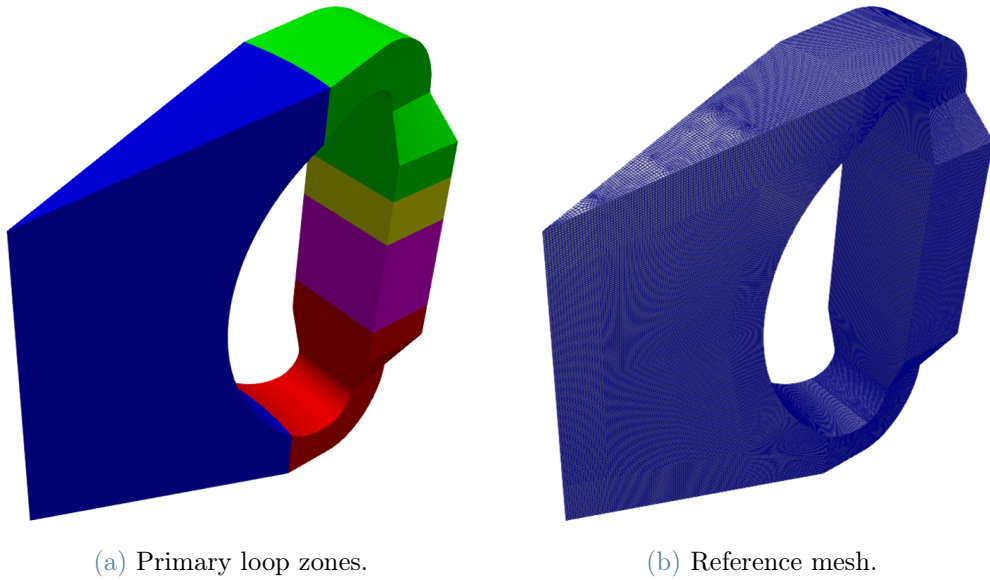
Figure 2.1: OpenFOAM simulation domain subdivided in zones for the primary loop (a) and 3D mesh of a 16th of the MSFR full core (b).

The outputs of interest that are evaluated for each simulation are:

- temperature distribution

- velocity distribution, enriched by arrows following the fuel motion

- minimum temperature at the core inlet $T_{min,inlet}$

- temperature jump across the inlet and outlet of the core $\Delta\bar{T}$

- maximum temperature in the core T_{max}

- mean temperature inside the core $\bar{T}_{core}$

- value of the volumetric flowrate $\dot{V}$

- power produced inside the reactor core Q_{core}

The mean temperatures at the core inlet and outlet are evaluated as mean adiabatic mixing temperatures as follows:

$$\bar{T}_{ad-mix} = \frac{\int_S T \, \boldsymbol{v} \cdot \boldsymbol{n} \, dS}{\int_S \boldsymbol{v} \cdot \boldsymbol{n} \, dS} \tag{2.2}$$

where the integral over the surface S involves the velocity $\boldsymbol{v}$ and temperature T and surface normal $\boldsymbol{n}$ of each cell face area.

The adiabatic mixing temperature can be approximated by its discretized form:

$$\bar{T}_{ad-mix} = \frac{\sum_i T_i \, \phi_i}{\sum_i \phi_i} \tag{2.3}$$

where ϕ_i is the volumetric flux across each cell face area.

2.2. Geometry sensitivity analysis

Since the CAD part representing the entire reactor core, and thus its 16th, is constantly being improved in order to reduce unwanted recirculations and lighten the mechanical and thermal loads as much as possible, it seems worthwhile to investigate, first, the influence of the shapes and profiles on the main operational variables at steady-state operational conditions.

(a)

(b)
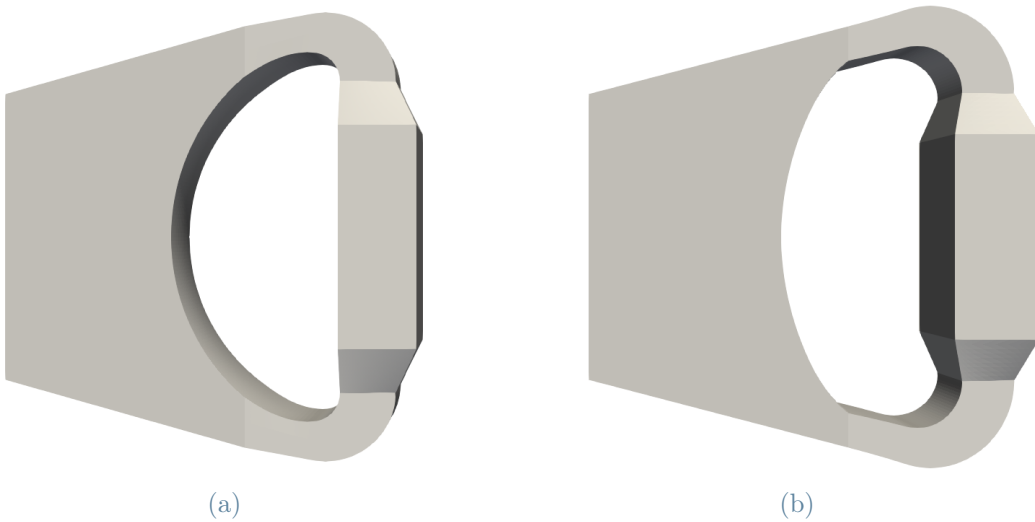
Figure 2.2: CAD parts for the geometry sensitivity analysis.

In Fig.2.2 the two geometries chosen for this analysis are depicted. They differ not only for a smoother connection between the blanket wall and the cold and hot legs for geometry (a), but also because the pump and the heat exchanger connections with the legs are symmetric for the geometry (b), where these components are also slightly larger than in case (a).

The simulations for the two geometries are performed with the same initial and boundary conditions, but tuning the sources' parameters with the idea of making a comparison in order to respect in both cases the requirements in terms of total power produced in primary loop, minimum core inlet temperature, and volumetric flowrate.

In Table 2.2 the results for the main operational parameters mentioned in Section 2.1 are reported, together with the relative percentage error between the two simulations. The results are very similar with only minor differences in the values of the maximum and minimum inlet temperatures and the temperature jump across the core, but in both cases it is possible to consider the requirements mentioned in Section 2.1 satisfied.

Output	Units	Geometry (a)	Geometry (b)
$T_{min,inlet}$	K	922.77	921.89
$\Delta \bar{T}$	K	95.17	95.81
T_{max}	K	1130.16	1098.27
$\bar{T}_{core}$	K	981.81	979.38
$\dot{V}$	m^3/s	0.2817	0.2803
Q_{core}	MW	184.75	184.68

Table 2.2: Main operational parameters of molten salt for steady state simulations for geometry (a) and (b).

In Fig.2.3 it is possible to compare the temperature and velocity distributions with the arrows following the fuel salt motion. When the parameters of the sources are properly selected, the two geometries produce outputs in great agreement in terms of the position of the hottest point, in the top centre part of the reactor core. In Fig.2.3 a difference that can be highlighted by the arrows superimposed on the velocity distribution is that in geometry (b) there is a stronger recirculation trend next to the blanket wall at the core inlet than in geometry (a), where this is not completely suppressed but at least weakened. In any case, this is an expected outcome given that the CAD part (a) was designed from geometry (b) with the specific goal of reducing recirculations in that zone. Thanks to the enhancement in terms of reduction of the recirculation trend and in order to be

more conservative in selecting the worst condition in terms of maximum temperature, the geometry selected for the transient simulations is the one shown in Fig.2.2a.
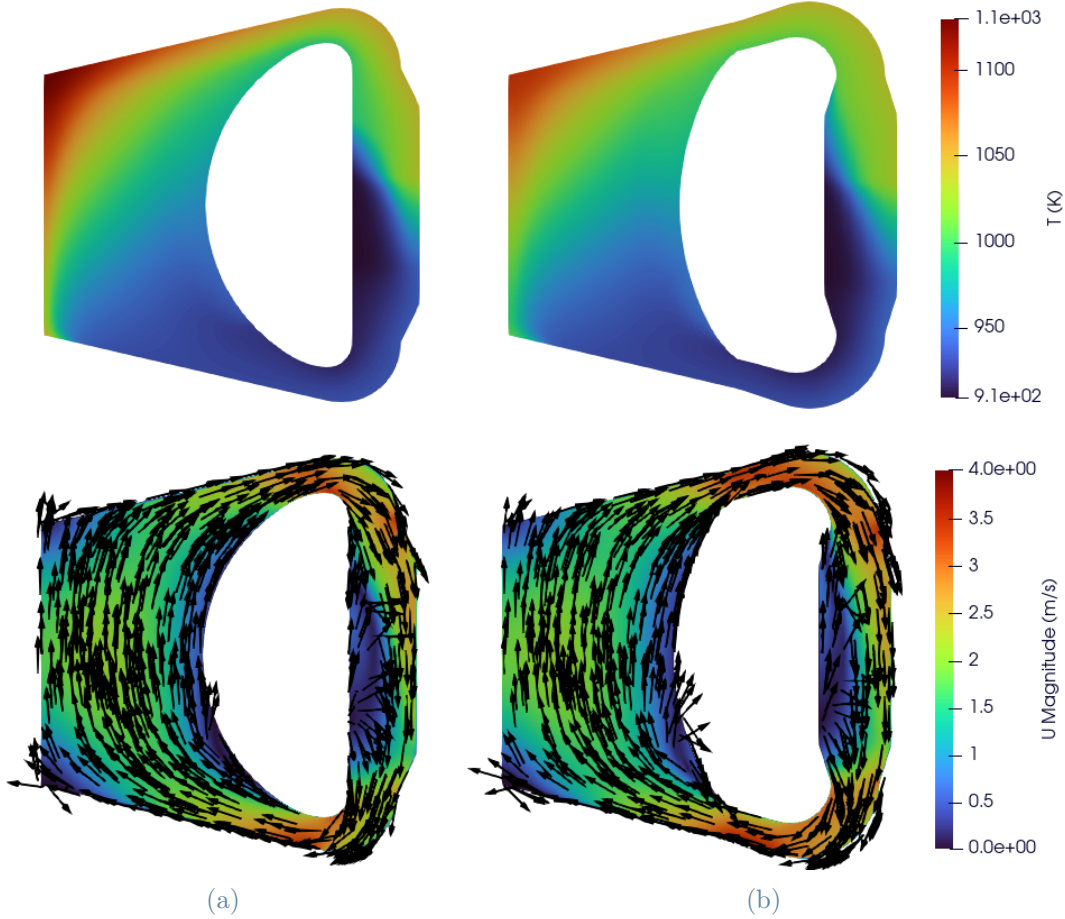

<center>(a)   (b)</center>

Figure 2.3: Temperature and velocity distributions at the steady state for geometry (a) and geometry (b) in Fig.2.2.

2.3. Mesh refinement sensitivity analysis

When dealing with steady state simulations, run with *msfrSimpleFoam*, the power iteration routine presented in Chapter 1 allows for the imposition of a target for the power. This nominal value is used to normalise fluxes and the routine returns a value for the effective multiplication factor, k_{eff}. Since the main focus of this thesis is assessing accidental scenarios, the *msfrPimpleFoam* solver is required to deal with transient simulations. This solver, as opposed to the power iteration routine included in the *msfrSimpleFoam*, allows the user to impose the k_{eff} and calculates the power. As a result, it appears reasonable to feed the *msfrPimpleFoam* with the outcomes of the *msfrSimpleFoam* in order to let the transient solver stabilise the distributions definitively. Therefore, a simulation is run

with *msfrPimpleFoam* for a few tens of seconds with fixed sources in order to get a correct starting point for the accidental event simulations. This approach sheds light on a problem strictly dependent on mesh refinement. Indeed, in the first seconds of simulations, the volumetric flowrate as well as the mean temperature of the core and the total reactor power show oscillatory behaviour that is never completely resolved as simulation time progresses. An example is shown in Fig.2.4.
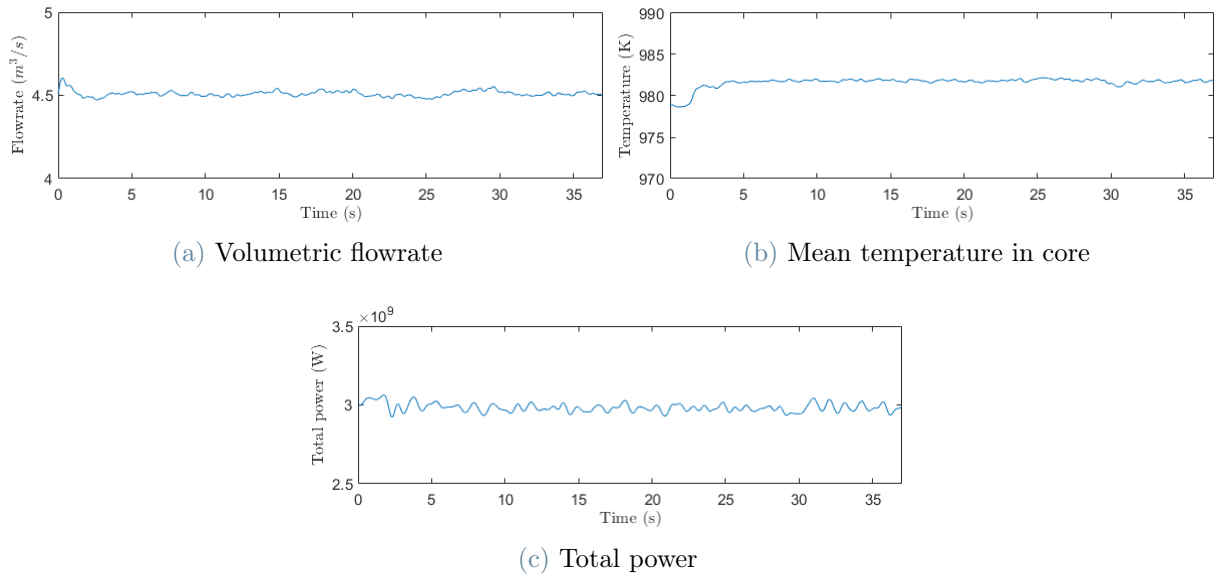

(a) Volumetric flowrate

(b) Mean temperature in core

(c) Total power

Figure 2.4: Oscillations of variables in *msfrPimpleFoam* simulation.

Part of these oscillations can be attributed to the turbulent flow, which is characterised by eddies and recirculations in different zones of the domain. The other contribution to this behaviour can be found in numerical issues. In order to investigate the nature of the oscillations, three meshes,obtained with the same generative algorithm but at different levels of refinement, are compared. The three meshes are shown in Fig.2.5, and the corresponding number of cells is reported in Table 2.3.

Mesh	N° of elements
(a)	155628
(b)	732984
(c)	1245024

Table 2.3: Number of elements for each mesh in Fig.2.5.
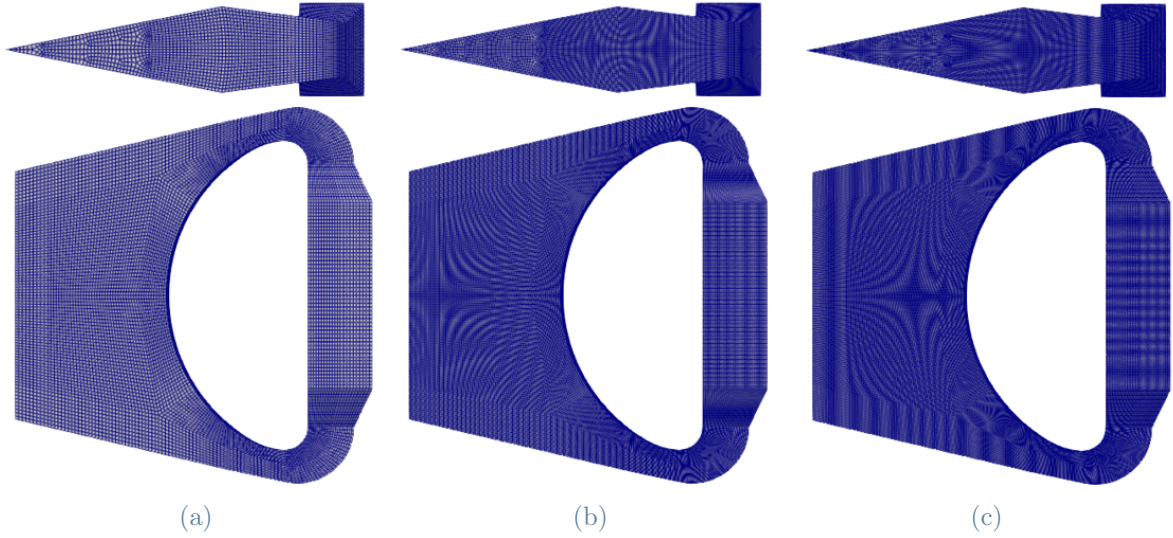
Figure 2.5: Three different levels of mesh refinement.

According to Table 2.4, by focusing on the amplitude of the oscillations, expressed by $\Delta(\pm\%)$, and ignoring the absolute values, which can always be adjusted by acting on the parameters of the sources, the mesh refinement reduces but does not eliminate the oscillatory behaviour. A further improvement could be made by refining the mesh, but the increase in computational cost lessens the benefits of the procedure. Another strategy could be to change the structure and the generative algorithm of the mesh without necessarily increasing the number of elements. In this thesis, a good compromise is found in the mesh with $\sim$1.2 million elements.

Mesh	Mean Power [MW]	$\Delta(\pm\%)$	Std Deviation [MW]
(a)	187.0	3.31	2.63
(b)	180.5	2.62	1.76
(c)	186.5	2.14	1.47
Mesh	Mean Flowrate [m^3/s]	$\Delta(\pm\%)$	Std Deviation [m^3/s]
(a)	0.2804	1.51	0.0016
(b)	0.2682	0.83	$7.80 \ 10^{-4}$
(c)	0.2818	0.68	$7.62 \ 10^{-4}$
Mesh	Mean Core Temperature [K]	$\Delta(\pm\%)$	Std Deviation [K]
(a)	982.46	0.073	0.30
(b)	981.14	0.047	0.21
(c)	981.81	0.031	0.17

Table 2.4: Comparison of oscillations for different levels of mesh refinements.

A deeper analysis deserves to be done to investigate the nature of these oscillations, for example, exploiting the Large Eddy Simulation (LES) instead of the RANS approach in order to inspect how the turbulence affects this behaviour. In any case, in the context of this work this oscillations does not compromise the results presented in the following chapters, since for those transient the time profiles are characterise by way more wide variations.

2.4. Sources sensitivity analysis

As anticipated at the beginning of this Chapter, the pump and the heat exchanger lack of prescriptive design specifications at the current state of the art. Therefore, these components are represented as a momentum source to account for the forced convection contribution and a heat sink to represent the thermal energy exchange with the intermediate loop of molten salt, respectively.

The OpenFOAM environment provides the tools required to manipulate the system of equations at run time via user-specified finite volume options, though the shorthand *fvOptions*, eliminating the need to compile the solver before each run. Among all the pre-implemented sources available in the toolkit, the two most general are tested in this work in order to promote the flexibility of the solver, allowing for the simulation of different accidental transient scenarios characterised by specific modifications of the sources. In fact, both the *SemiImplicitSource* and the *CodedSource* enable including time variant sources, both for scalar or vector equations, with a profile specified by the user. The *CodedSource* provides hooks to include sources and sinks, to constrain values before the equation is solved and to apply corrections after the equation has been solved. The *SemiImplicit-Source* allows to include a source term, $S(x)$, within a specified region decomposed into explicit and linearised implicit contributions in the form:

$$S(x) = S_u + S_p\,x \tag{2.4}$$

where S_u and S_p are the injection rate coefficients [26].

The sensitivity analysis presented in the following is performed on the momentum source representing the pump component because the implementation of a vector source results in being trickier than the heat sink needed in the scalar energy conservation equation to take into account the heat exchanger. The simulations are run to reach the steady state in order to highlight the discrepancies caused by different kinds of sources with fixed parameters without the influence of time evolution, which could superimpose and conceal

the source type dependence. The geometry adopted is the one shown in Fig.2.1a and the source parameters are tuned in order to respect the general requirements mentioned in Section 2.1.

In Table 2.5 the operational parameters of interest are reported. In this case, the differences in the temperature jump and the minimum temperature at the inlet of the core are also related to a rough tuning of the sources, as it is possible to deduce, for example, from the 2.02 % relative error in volumetric flowrates, which could be greatly reduced or even eliminated with more precise trial values for the sources' parameters.

Output	Units	$SemiImplicitSource$ (a)	$CodedSource$ (b)
$T_{min,inlet}$	K	922.77	915.26
$\Delta\bar{T}$	K	95.18	94.15
T_{max}	K	1130.16	1045.86
$\bar{T}_{core}$	K	981.81	981.91
$\dot{V}$	m^3/s	0.2817	0.2875
Q_{core}	MW	184.75	185.82

Table 2.5: Main operational parameters of molten salt for steady state simulations for *SemiImplicitSource* (Fig.2.6a) and *CodedSource* (Fig.2.6b).

This adjustment is not done since the main differences arising from two types of sources can be already identified by the velocity and temperature distributions depicted in Fig.2.6. First of all, even though the profiles in the zones representing the pump and the heat exchanger are not of interest for this thesis due to the significant simplifications and approximations made to describe these components, it is nonetheless useful to note that the forces the direction of the salt flow downward, as indicated by the flow arrows. This forced motion may be the cause of the strong recirculation trend next to the blanket wall in contrast to the *SemiImplicitSource*, which allows a smoother development of the fuel motion inside that zone. These strong recirculations lead to a stagnant zone where the temperature increases, worsening the thermal load on the blanket wall. Even if the *CodedSource* returns a more physically sensible distribution in the heat exchanger and pump zones, these undesirable outcomes lead to the selection of the *SemiImplicitSource* for both components, for steady state and accidental simulations. This choice is coherent with the design objectives pursued in favouring the entrance of the salt in order to suppress these recirculations. However, it is important to be aware that this approximate approach is only a preliminary description and that it allows a degree of freedom that will vanish once the design specifications are agreed upon.
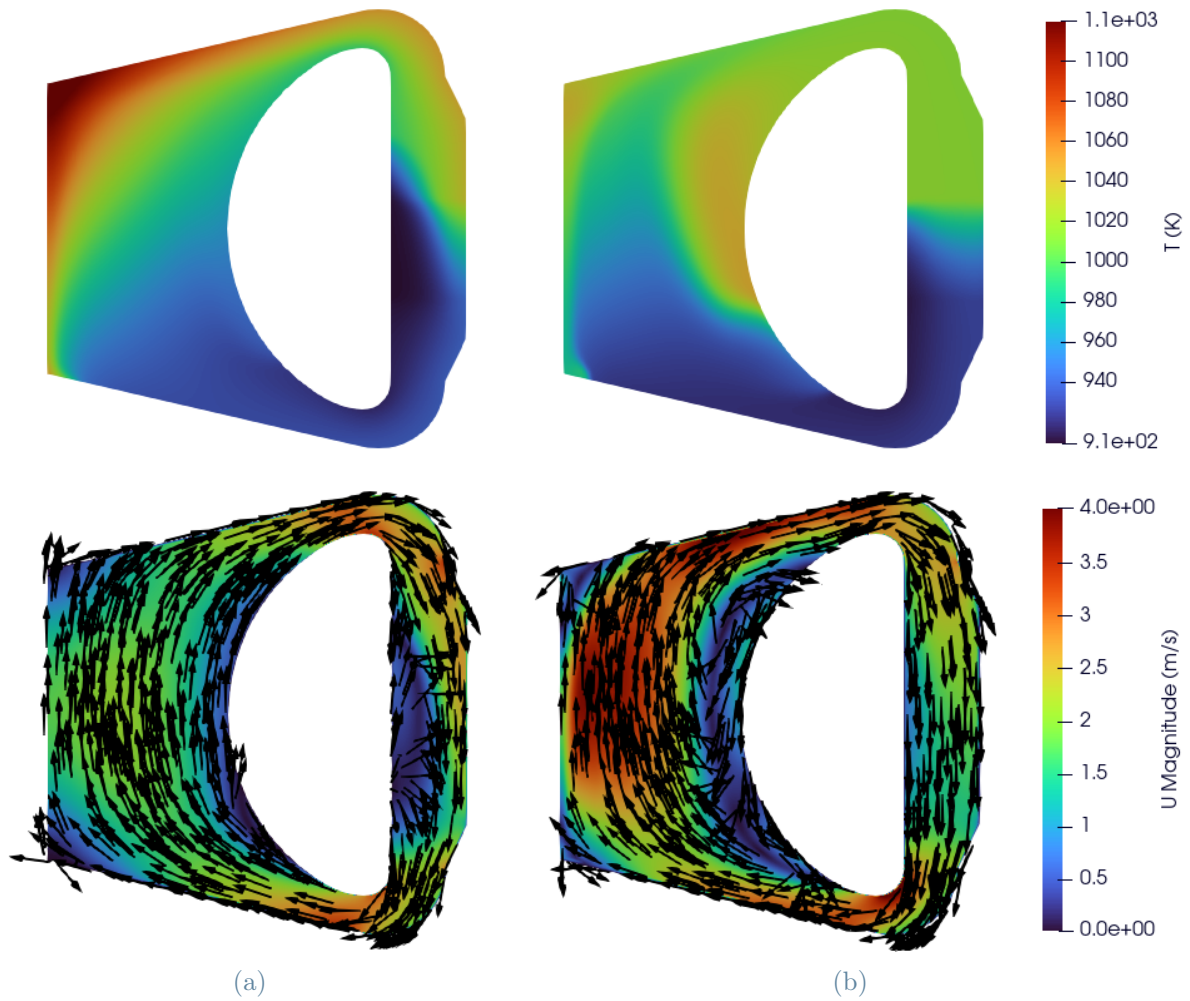
(a)   (b)

Figure 2.6: Temperature and velocity distributions at the steady state for *SemiImplicit-Source* (a) and *CodedSource* (b).

2.5.   Turbulence sensitivity analysis

Since the case study presented in this thesis involves the solution of a CFD problem, turbulence modelling must be taken into account in order to get a proper description of the fuel motion in the MSFR primary loop. Therefore, for the sake of completeness and without claiming to present a detailed analysis of turbulence, a sensitivity analysis compares two of the most commonly used turbulence models in industrial applications:

- *Realizable $k - \varepsilon$*

- *$k - \omega\,SST$*

The goal is to evaluate the order of magnitude of differences in the main operational parameters when selecting a particular two-equation eddy viscosity model already available

in OpenFOAM.

Considering a density $\rho = 4306.71$ kg/m^3, a diameter of 2.25 m, a velocity field of the order of 2 m/s as a mean representative value, and a dynamic viscosity of $\mu = 2.537 \cdot 10^{-2}$ Pa·s, the Reynolds number is approximately $8 \cdot 10^5$, indicating that the flow is fully turbulent. The simulations are run on the geometry depicted in Fig.2.9b using the same parameters for the sources to assess the influence of turbulence models alone. Wall functions are adopted for both $Realizable\,k - \varepsilon$ and $k - \omega\,SST$ models because the y^+ evaluated for all the reactor walls falls within the proper range to use these boundary conditions, namely $30 < y^+ < 300$.

Output	Units	$Realizable\,k - \varepsilon$	$k - \omega\,SST$
$T_{min,inlet}$	K	921.89	922.14
$\Delta \bar{T}$	K	95.81	94.23
T_{max}	K	1098.27	1120.63
$\bar{T}_{core}$	K	979.38	984.54
$\dot{V}$	m^3/s	0.2803	0.2857
Q_{core}	MW	184.68	184.59

Table 2.6: Main operational parameters of molten salt for steady state simulations for $Realizable\,k - \varepsilon$ and $k - \omega\,SST$.

The results of the two simulations are reported in Table 2.6, and it is possible to conclude that there is a good agreement using the two pre-implemented turbulence models with a maximum relative error of 2.04 % for the maximum temperature in the core, which can be considered a tolerable difference.

2.6. Boundary conditions sensitivity analysis

The last sensitivity analysis performed in this thesis regards the boundary condition (BC) imposed to the neutronic part of the simulation to represent the presence of the upper and lower reflectors and the blanket. Both the solvers for the steady state and transient problems allow to implement albedo boundary conditions as illustrated in Section 1.4 in the form of:

$$D_{n,g}\nabla\varphi_g = -\frac{1}{2}\left(\frac{1 - \alpha_g}{1 + \alpha_g}\right)\varphi_g \tag{2.5}$$

In this context, two simulations are run; the former fixes the ratio between outgoing and incoming neutron currents, α_g, to zero at walls for all the energy groups, thus implying

the exploitation of vacuum boundary conditions. The latter implements albedo boundary conditions thanks to α_g coefficients evaluated through a Monte Carlo simulation adopting the reactor physics and burnup code SERPENT 2 and the JEFF-3.1.1 cross section library and reported in Table 2.7. All the other parameters included ones related to the thermal-hydraulic part of the simulations are equal for the two cases in order to isolate the influence of these boundary conditions on the axial and radial power density profile which leads to a total power produced in the primary circuit of 187.5 MW_{th}.

Group	Blanket	Reflectors
(1)	0.124914	0.145499
(2)	0.384934	0.544018
(3)	0.674503	0.777057
(4)	0.759569	0.720572
(5)	0.847486	0.960246
(6)	1.095101	1.333553

Table 2.7: α_g parameters of each group for blanket and reflectors.

In Fig.2.8, the axial and radial profiles of the power density are represented along the centerlines AA' and BB' for both the boundary conditions under investigation. The imposition of albedo boundary conditions results in a more uniform profile with respect to the vacuum boundary conditions as it can be observed from the extremes of the profiles. In fact, both radially and axially in correspondence of the walls of the reactor the power rises, and since the total power produced in the primary loop is fixed the power density at the center part of the reactor lowers. Another consequence of the choice of boundary conditions can be found in the value of the effective multiplication factor, namely $k_{eff,vacuum} = 0.978399802$ and $k_{eff,albedo} = 1.00012995$, evaluated thanks to the power iteration routine.
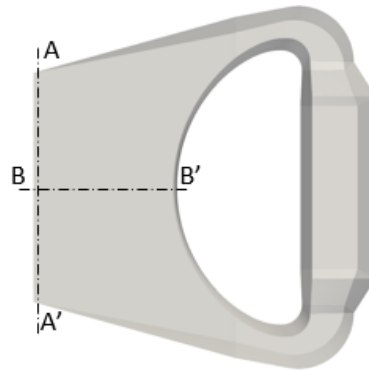
Figure 2.7: Centerlines AA' and BB' to compare axial and radial power density profiles.

(a) Radial power density profile.

(b) Axial power density profile.
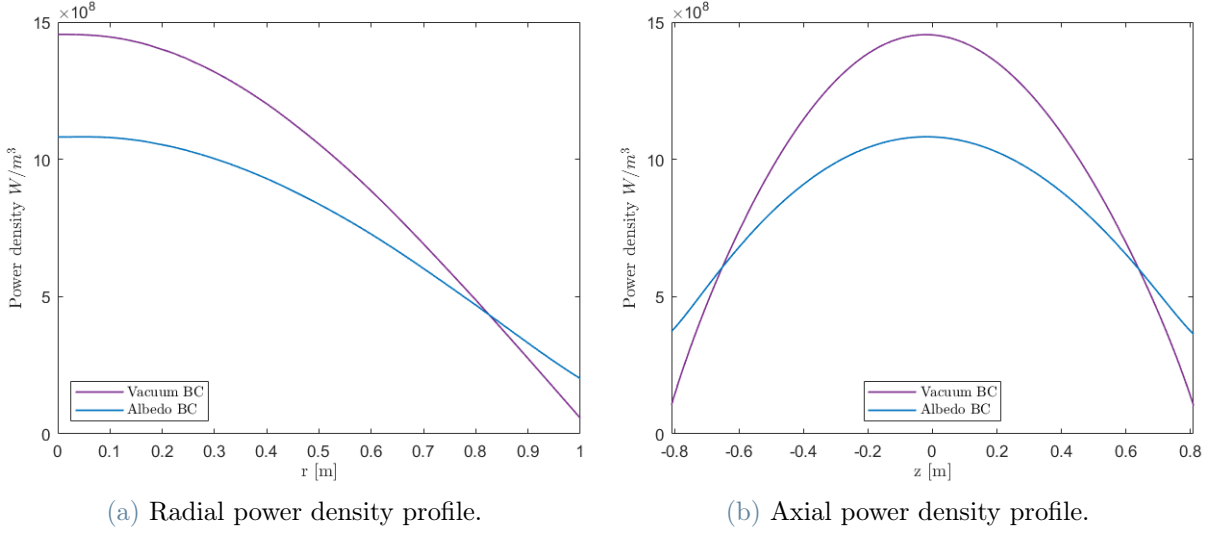
Figure 2.8: Axial and radial power density distributions for albedo and vacuum BC.

In Tables 2.8 and 2.9, the mean and maximum values for the each group flux at the walls are presented for the albedo and vacuum boundary conditions respectively. The fluxes for the albedo boundary conditions are higher with respect to the vacuum boundary conditions of factor ranging from 1.6 to 13.5. These factors, evaluated for each group, can be used to rescale the fluxes at the walls in other simulations with vacuum boundary condition. This estimate could provide an indication of the irradiation conditions that the reactor is subjected to, considering the influence of the blanket and reflectors.

	Blanket		Fuel Void		Upper Reflector		Lower Reflector	
Group	Mean	Max	Mean	Max	Mean	Max	Mean	Max
	$\times 10^{17}$	$\times 10^{18}$	$\times 10^{15}$	$\times 10^{16}$	$\times 10^{17}$	$\times 10^{18}$	$\times 10^{17}$	$\times 10^{18}$
(1)	1.59	0.35	0.76	0.91	1.12	0.66	1.14	0.68
(2)	4.93	1.08	3.72	3.02	3.49	2.11	3.54	2.17
(3)	8.56	1.87	7.19	5.85	6.09	3.82	6.16	3.93
(4)	6.30	1.38	3.45	3.86	4.46	2.79	4.53	2.87
(5)	3.48	0.76	1.42	2.04	2.45	1.54	2.50	1.59
(6)	0.47	0.10	0.17	0.27	0.33	0.21	0.34	0.22

Table 2.8: Mean and maximum flux for each nth energy group on each wall expressed in $\#neutrons/m^2\,s$ for vacuum boundary conditions.

Group	Blanket Mean $\times 10^{18}$	Blanket Max $\times 10^{18}$	Fuel Void Mean $\times 10^{15}$	Fuel Void Max $\times 10^{17}$	Upper Reflector Mean $\times 10^{18}$	Upper Reflector Max $\times 10^{18}$	Lower Reflector Mean $\times 10^{17}$	Lower Reflector Max $\times 10^{18}$
(1)	0.32	0.61	1.53	0.33	0.28	1.14	0.28	1.17
(2)	1.26	2.41	6.14	1.13	1.26	5.04	1.28	5.19
(3)	3.41	6.50	11.57	2.31	3.38	13.34	3.43	13.71
(4)	2.77	5.29	6.83	1.80	2.21	8.79	2.25	9.04
(5)	1.92	3.64	3.53	1.12	1.79	6.73	1.83	6.92
(6)	0.38	0.73	0.51	0.19	0.45	1.53	0.46	1.58

Table 2.9: Mean and maximum flux for each nth energy group on each wall expressed in $\#neutrons/m^2\,s$ for albedo boundary conditions.
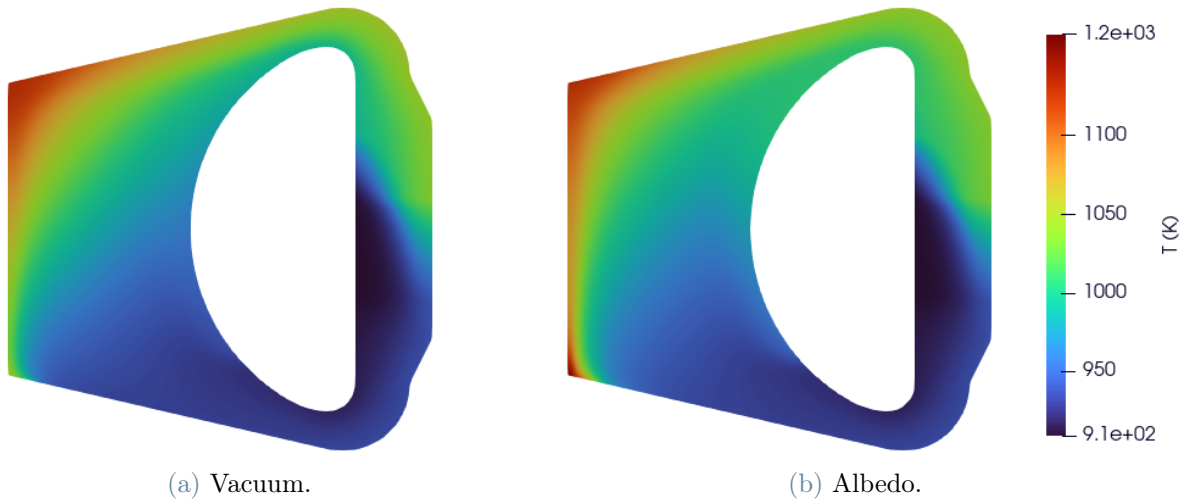
(a) Vacuum.   (b) Albedo.

Figure 2.9: Temperature distributions for albedo and vacuum boundary conditions.

Output	Units	Vacuum BC	Albedo BC
$T_{min,inlet}$	K	922.77	922.81
$\Delta \bar{T}$	K	95.18	95.22
T_{max}	K	1130.16	1164.34
$\bar{T}_{core}$	K	981.81	984.54
$\dot{V}$	m^3/s	0.2817	0.2819
Q_{core}	MW	184.75	184.69

Table 2.10: Main operational parameters of molten salt for steady state simulations for vacuum and albedo boundary conditions.

Finally, in Fig.2.9 the temperature distributions are illustrated, and in Table 2.10 the operational parameters evaluated for each boundary condition type are reported. The main difference consists of the value of the maximum temperature. This value is higher when imposing albedo boundary conditions instead of vacuum ones. Furthermore, in the albedo case, the hottest zone extends to the lower reflector, and there is a second peak of temperature in the bottom centre part of the core.

2.7.   Reference case steady state simulation results

In previous Sections, various sensitivity analyses have been presented. In order to assess the dynamic behaviour of the MSFR during an accidental scenario in a consistent way, a unique setup is selected. In particular the geometry shown in Fig.2.2a is chosen as reference, exploiting the *SemiImplicitSource* for both the pump and the heat exchanger, *Realizable $k - \varepsilon$* turbulence model and vacuum boundary conditions for the reflectors and blanket walls. The idea is to provide a case study that simultaneously satisfies the requirements for the nominal conditions of the reactor and ensures flexibility in terms of modelling the primary loop components.

As previously explained, the steady state condition is obtained by running a simulation with the *msfrSimpleFoam* solver till convergence, then feeding the *msfrPimpleFoam* solver with the outcomes of the former simulation, and letting the distributions develop for some tens of seconds, in this case 37 s, with a time invariant energy sink and momentum source.

2.7.1.   Thermal-hydraulics results

Even if the outcomes of this simulation have already been shown in previous sections to make some of the comparisons, in order to give a comprehensive view of the starting conditions for the transient simulation, the main parameters of interest are reported again in Table 2.13. In Fig.2.10 the velocity distribution is depicted, in particular in Fig.2.10a with 3D stream lines to highlight the recirculation trend next to the blanket wall and in Fig.2.10b with vectors that indicate the salt flow direction.

Output	$T_{min,inlet}$	$\Delta \bar{T}$	T_{max}	$\bar{T}_{core}$	$\dot{V}$	Q_{core}	Q_{total}
Units	K	K	K	K	m^3/s	MW	MW
Value	922.77	95.18	1114.49	981.81	0.2818	184.75	186.7

Table 2.11: Main operational parameters of reference case at steady state.

(a) Stream lines.

(b) Direction arrows.
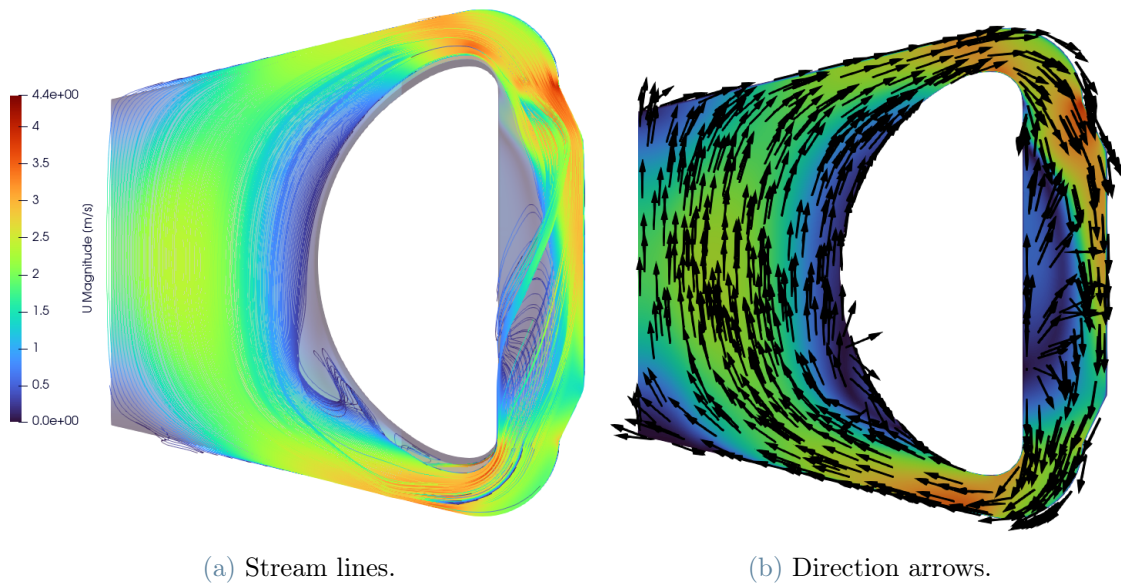
Figure 2.10: Velocity distribution of the reference case at steady state.
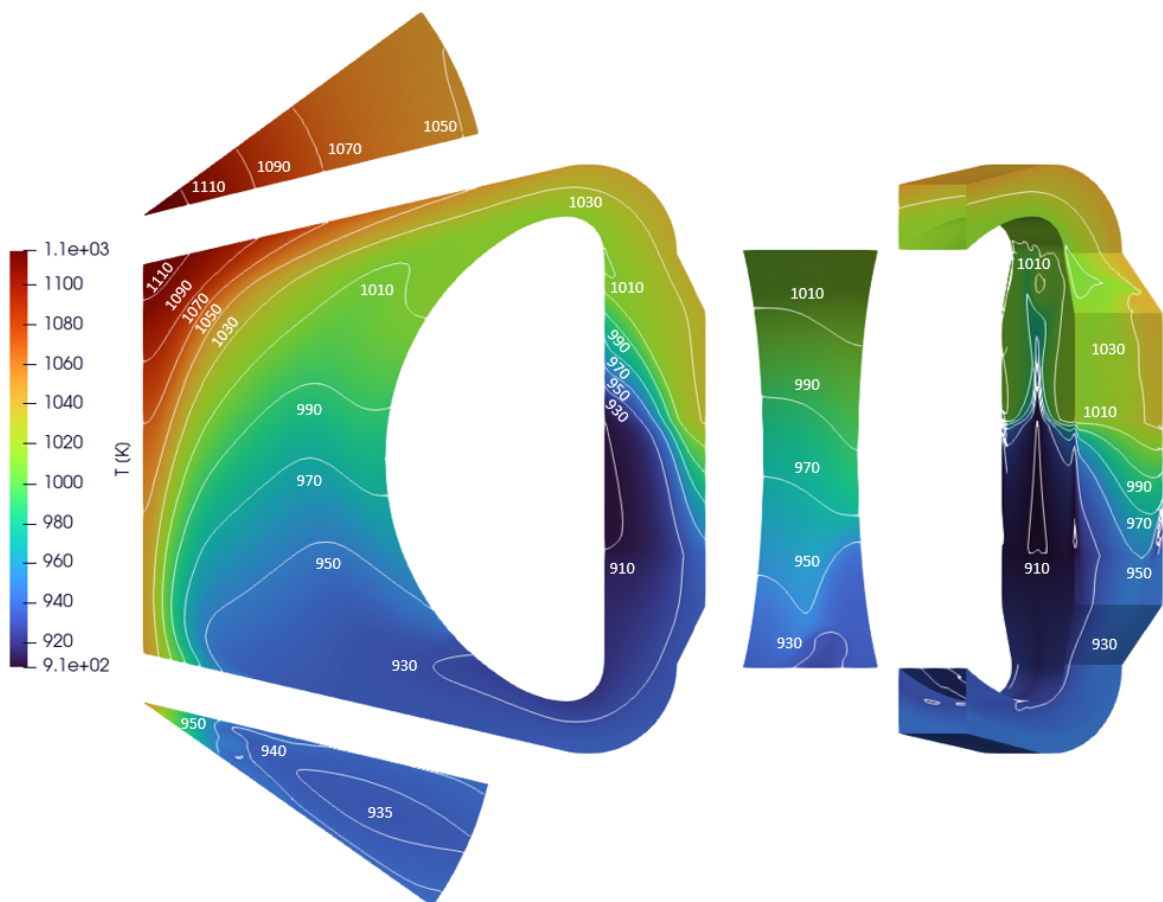
Figure 2.11: Temperature distribution of the reference case at steady state.

Since the current work also pursues the objective of providing useful values to evaluate the harsh conditions under which the reactor operates, with the ultimate goal of supporting the design phases, a cross section of the reactor walls is shown in Figs.2.11 and 2.12 with the mechanical and thermal load to which the walls are subjected, expressed in terms of temperature and total pressure, respectively. In Fig.2.11, isothermal lines are drawn on the wall cross sections and on a vertical midplane cutting the core. As expected from other works available in the literature [11, 12, 18], the maximum temperature is in the top centre part of the core while the minimum temperature, excluding the heat exchanger and pump zones which are not of interest in this work, is in correspondence of the core inlet. Since the solvers adopted in this thesis are meant for incompressible fluids, the output of pressure that OpenFOAM provides is the kinematic pressure, p_k, evaluated as the ratio between the static pressure, p_s (Pa), and the reference constant density, ρ (kg/m^3):

$$p_k = \frac{p_s}{\rho} \quad (m^2/s^2) \tag{2.6}$$

therefore, in order to get the value of the total pressure, a post-processing function pre-implemented in the OpenFOAM environment is adopted, selecting a reference value in order to get a minimum pressure in the fuel circuit of 10^5 Pa.

Figure 2.12: Total pressure distribution of the reference case at steady state.

2.7.2. Neutronic results

In terms of neutronic outcomes, fast spectrum reactors subject structural components to severe irradiation conditions, with fast neutrons being the primary, but not only, cause of radiation damage. In fact, a highly energetic neutron is able to displace an atom of the metallic structure, referred to as primary knocked-on atom, which in turn can trigger a collisional cascade or induce a thermal spike. The metrics typically adopted to measure radiation damage are the fluence and the displacement per atom, *dpa*, which embodies also information about the kind of material and the energy spectrum involved. In MSFRs, the fuel, which is also the coolant, being in direct contact with structural materials, exposes the components to conditions even harsher than in other fast spectrum reactors.

As a result, in order to provide useful data for an assessment of the potential radiation exposure damage on the structure, which is beyond the scope of this thesis, the mean and maximum fluxes for each energy group, Table 2.12, and the position where the maxima are reached, Fig.2.13, are reported. Please note that only one pink circle per wall is shown because the positions of the maximum total flux and maximum group fluxes coincide.
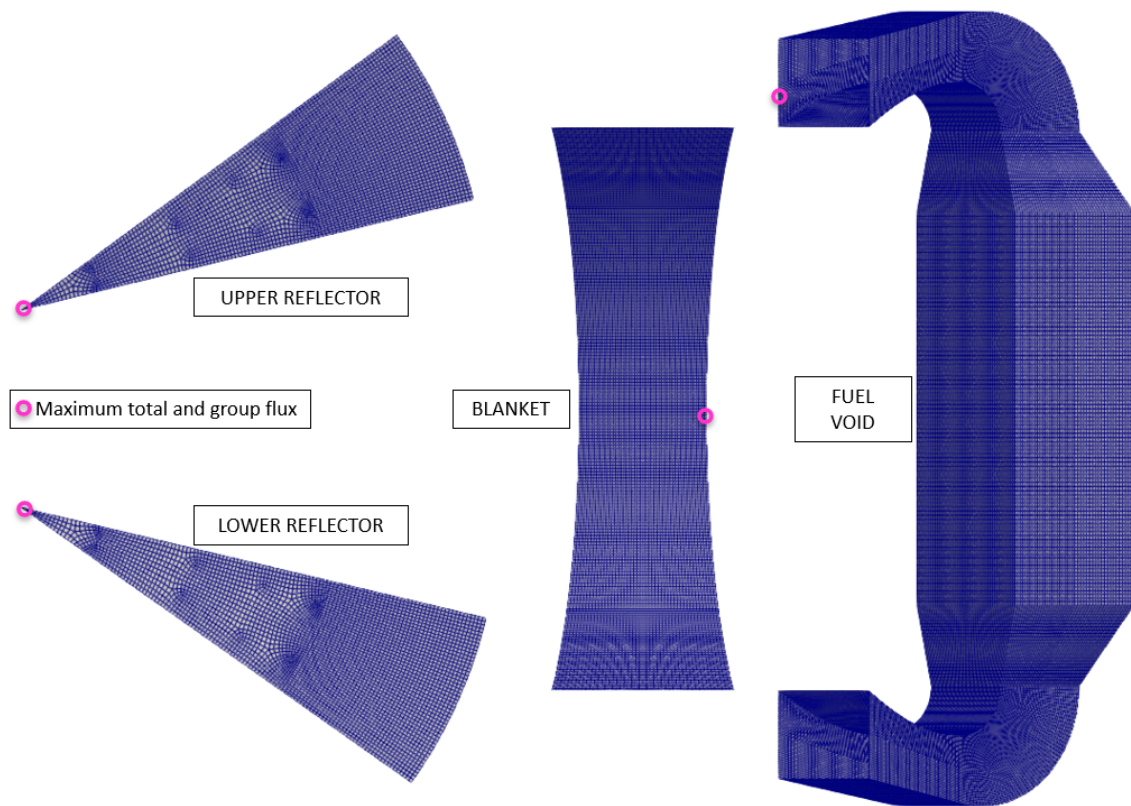
Figure 2.13: Positions of maxima for the fluxes on each wall.

Group	Blanket		Fuel Void		Upper Reflector		Lower Reflector	
	Mean $\times 10^{17}$	Max $\times 10^{18}$	Mean $\times 10^{15}$	Max $\times 10^{16}$	Mean $\times 10^{17}$	Max $\times 10^{18}$	Mean $\times 10^{17}$	Max $\times 10^{18}$
(1)	1.59	0.35	0.76	0.90	1.12	0.66	1.14	0.68
(2)	4.91	1.07	3.72	3.02	3.48	2.11	3.52	2.16
(3)	8.52	1.86	7.18	5.84	6.06	3.81	6.12	3.91
(4)	6.27	1.37	3.44	3.84	4.44	2.78	4.50	2.86
(5)	3.46	0.76	1.42	2.03	2.44	1.54	2.48	1.59
(6)	0.47	0.10	0.17	0.27	0.32	0.21	0.34	0.22

Table 2.12: Mean and maximum flux for each nth energy group on each wall expressed in $\#neutrons/m^2\,s$.

(a) Radial power density profile.

(b) Axial power density profile.
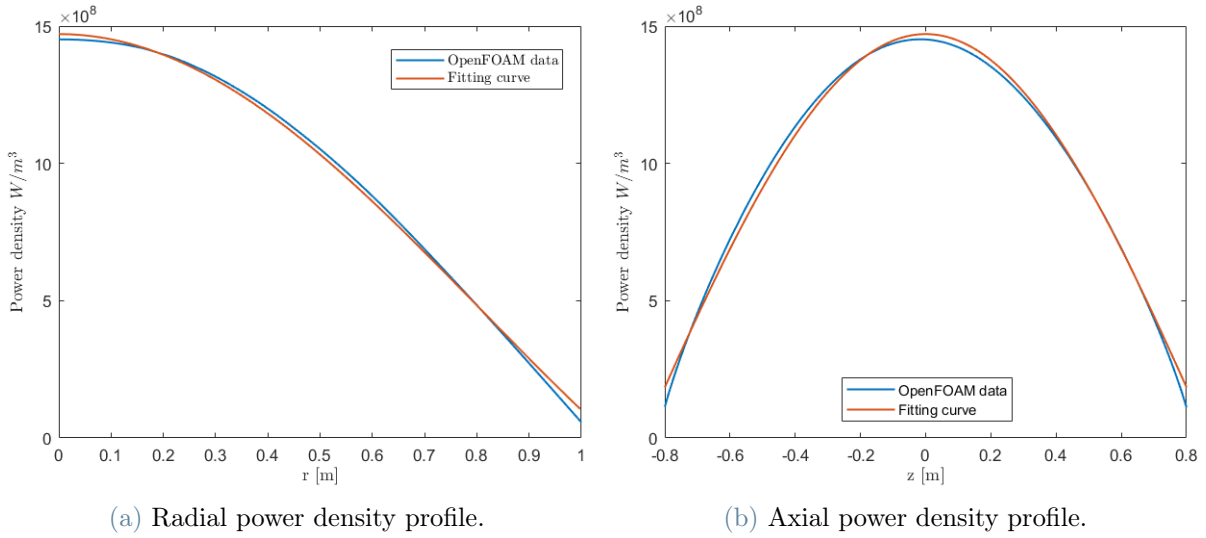
Figure 2.14: Axial and radial power density distributions for the reference case at steady state.

The power density distribution, which includes both the prompt and decay contributions, is shown in Fig.2.15. In Figs.2.14a and 2.14b, the power profiles radially at the mid-plane and axially in the proximity of the core centre part are represented, together with fitting curves obtained starting from a Bessel function for the radial profile and a cosine shape of the radial one, expressed in Eqs.(2.7a) and (2.7b). These functions strongly resemble the axial and radial solutions of the diffusion equation for a right cylinder with vacuum boundary conditions, keeping in mind that at the extremes of the real profiles, thus in proximity of the walls, there are differences due to the influence of the blanket and upper

and lower reflectors, which can be simulated with albedo boundary conditions.

$$f_r(r) = A\,J_0(Br) \tag{2.7a}$$

$$f_z(z) = C\,cos(Dz) \tag{2.7b}$$

where A, B, C, D, are the fitting parameters and the results show a $R^2 = 99.86\%$ for radial and $R^2 = 99.76\%$ for the axial profile.
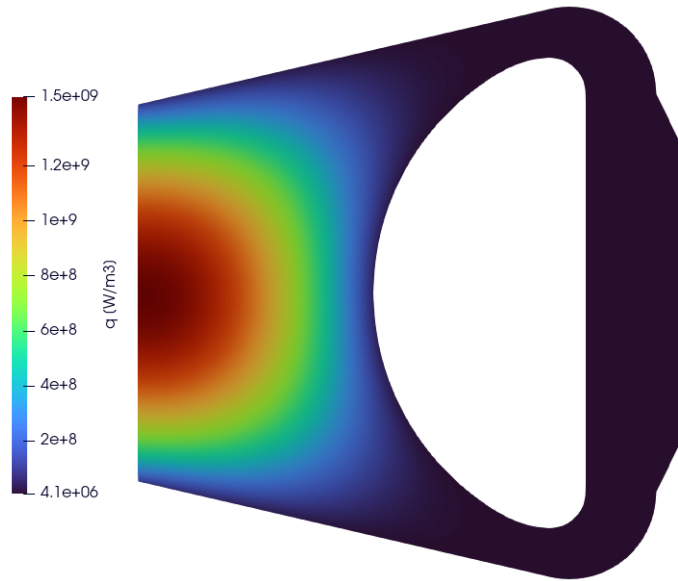
Figure 2.15: Volumetric power density distribution for the reference case at steady state.

Finally, the profiles of the longest and shortest lived precursors are shown in Figs 2.16a and 2.16b to highlight the effects of the circulating liquid fuel motion on the delayed neutron precursors distributions. As expected, the longest lived precursors are considerably influenced by the velocity distribution of the salt, while the shortest lived ones are less affected. The other six precursors groups evaluated in this thesis show intermediate behaviour. The dependence of these distributions on the velocity field is at the basis of the challenging aspect of the MSFR of reduced delayed neutron fraction, β, because the salt motion induces the drift of precursors that decay outside of the core and, therefore, lowers the delayed neutron fraction in the core with respect to a reactor where fuel is at rest. This parameter, β, drives the promptness of the system to modify its state in response to perturbations; a faster system, with a lower β, is more difficult to control.

(a) Longest lived.   (b) Shortest lived.
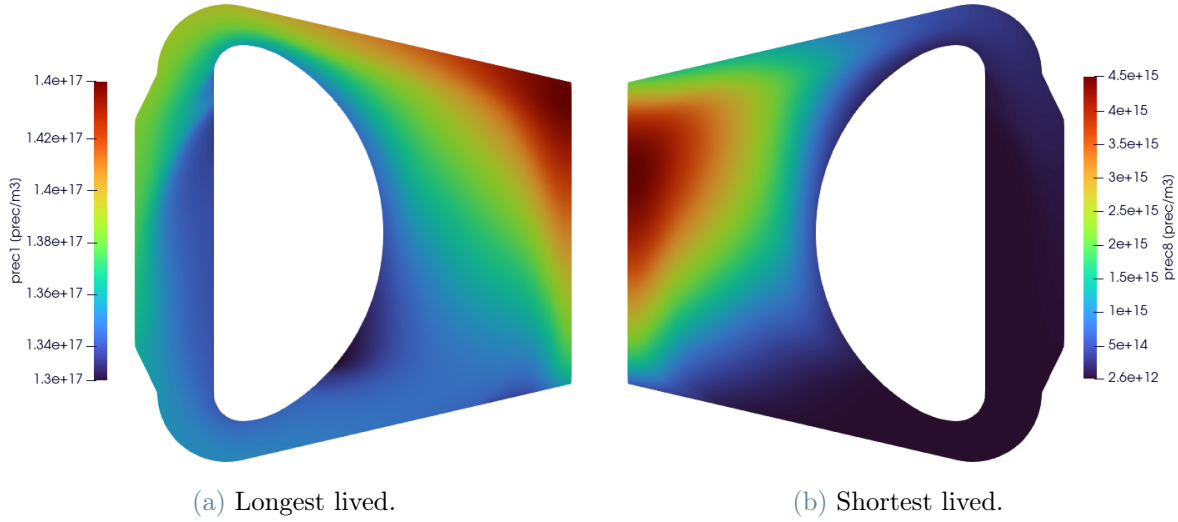
Figure 2.16: Shortest and longest lived precursors distributions for the reference case at the steady state.

2.8.   Feedback coefficient evaluation

The MSFR is characterised by strong negative feedback coefficients, which provide the attractive benefit of inherent safety. In this context, this reactor concept is even superior than other traditional solid-fuelled fast reactors since the feedback coefficients for the MSFR have a larger negative magnitude [27]. The reason lies in the major contributions of the Doppler effect and of the thermal expansion of the fuel. In response to a temperature increase, the former is enhanced by the combined action of a softer spectrum and thorium exploitation, while the latter results in augmented neutron leakages as a consequence of a density increase. Globally, the total thermal feedback coefficient can be associated with a reference value of -5 pcm/K [1].

In this thesis, to account for the feedbacks in the reactor, i.e., Doppler and thermal expansion effects, the neutronics parameters are corrected with temperature dependencies in the form reported in Eq.(1.16). Nevertheless, it seems useful to get a unique reference value for the thermal feedback coefficients to inspect the reactivity insertion in future chapters when dealing with accidental transient scenarios. To do so, two simulations are implemented with fixed constant temperature fields set at 900 and 1000 K. The velocity field is imposed as the one resulting from the steady state simulation presented in Section 2.6, and only the neutronics equations are solved, turning on the flag of the power iteration routine to get the multiplication factors, k_{eff}, corresponding to the two temperature levels imposing a target power of 187.5 MW.

The value of the feedback coefficient, $\alpha_{thermal}$ in pcm/K, is then estimated as:

$$\alpha_{thermal} = \frac{\varrho_{1000} - \varrho_{900}}{1000 - 900} \tag{2.8}$$

where ϱ is the reactivity evaluated as:

$$\varrho = \frac{k_{eff} - 1}{k_{eff}} \tag{2.9}$$

The outcomes of the two simulations are reported in Table 2.13.

T (K)	k_{eff} (-)	ϱ (pcm)
900	0.98314	-1714.9
1000	0.97771	-2279.4

Table 2.13: Reactivity and multiplication factors for steady state simulations at 900 and 1000 K.

These values result in an $\alpha_{thermal} = -5.645\ pcm/K$, in good agreement with the reference value found in literature $-5\ pcm/K$.

As was already discussed, the most appealing aspect of MSFR, i.e., the circulating liquid fuel, also presents significant challenges due to phenomena that are absent from conventional solid-fueled reactors, such as delayed neutron precursors drift. When dragged by the fuel salt, a part of the precursors decay outside the core; therefore, the delayed neutron fraction, β, is reduced. Given the connection between this parameter and the promptness with which the reactor responds to perturbations, this phenomenon raises certain concerns about the control and safety of the reactor. Furthermore, in the case of a reduced mass flowrate, the precursors hold-back implies a positive reactivity insertion. Given that, in the light of the purpose of this thesis, it seems essential to get a first estimation of the effect of the liquid fuel motion in terms of the positive reactivity insertion deriving from the precursors hold-back. Adopting the same strategy to evaluate the $\alpha_{thermal}$ coefficient, a simulation is run with a velocity field imposed at zero, with the aim of representing the worst case and thus adopting a conservative approach. To provide a comparison with the simulation presented above, the temperature field is fixed uniformly at 1000 K. The reactivity insertion caused by the precursors hold-back from the velocity field of the reference steady state to the fuel completely at rest is evaluated as:

$$\varrho_{1000,zerovelocity} - \varrho_{1000,steadystate} = -2105.8 - (-2279.4) = 173.6\ pcm \tag{2.10}$$

3 | Unprotected Loss of Fuel Flow

The possibility to simulate transient scenarios that would require experimental campaigns unacceptable in terms of safety requirements or economic expenses is one of the major benefits intrinsic to the numerical approach. Therefore, after the description of the steady state, obtained with the effort to represent at best the nominal operating conditions of the MSFR, the investigation proceeds with the simulations for the accidental scenarios to interrogate the reactor dynamic behaviour when it comes to potentially harmful situations.

In the case of MSFRs, it is possible to identify main functions for which, if the component delivering them fails, partially or completely, the non-fulfillment could potentially trigger an accidental event. To begin with, the cooling function, which is provided by heat transfer to the intermediate loop via the heat exchanger and enhanced by the forced convective motion imposed by the pump, can exhibit anomalies in both directions: a boost or a worsening of the heat exchange capabilities for the former and an overspeed or a coast-down for the latter. The malfunctioning of the reprocessing system may then result in an unwanted positive reactivity insertion, which can be classified as a different category of transient initiators [17, 28]. Finally, the emergency draining tank, which delivers the storage and cooling safety functions, may be subjected to abnormal operating conditions that affect heat removal or core salt discharge in the storage, leading to an unintended and potentially dangerous event. These examples highlight the critical significance of identifying the most relevant initiators and the resulting accidents, as well as assessing the reactor's dynamic response in those undesirable cases. This kind of analysis and enumeration process is out of the scope of this thesis, but in the context of the Horizon 2020 Euratom SAMOFAR project, some of the most concerning accidental scenarios were identified and listed [29]. Based on this classification, this thesis first investigates a primary loop malfunction by simulating the loss of fuel flow caused by the failure of the pumps.

In Section 3.1 the transient case is described along with the modelling assumptions to represent the unprotected loss of fuel flow, and in Section 3.2 the outcomes of the simulation are reported.

3.1.   Accidental scenario modelling

The unprotected loss of fuel flow (ULOFF) refers to an accident such that the primary pumps are no longer able to deliver their function of imposing a forced convection, due to a shortage of electrical power or a fuel circuit blockage, for example. In this work, this transient scenario is assumed to be symmetric, so the failure affects equally all the sixteen pumps, and unprotected, so no mitigating counteractions are contemplated to limit the harmful consequences of the malfunction.

The transient coast-down of the pump is simulated through an exponential reduction of the momentum source with a time constant, τ, of 5 seconds [30]. Thanks to the versatility of the *SemiImplicitSource* implemented in the solvers, it is possible to impose a source in the form:

$$f(t) = f_0 \, e^{-t/5} \tag{3.1}$$

where f_0 is the source parameter applied in the reference steady state simulation. The parameters characterising the heat sink, which allows for the heat transfer between the primary and intermediate loops, are kept constant at their steady state values. The hypothesis is supported by the assumption that the intermediate and power conversion loops are meant to manage a natural circulation regime, at least for the first few minutes of the transient, thanks to flexibility in their design [17, 27]. Due to the lack of design prescriptions and the subsequent strong approximations to describe the heat exchanger, this assumption is deemed acceptable for the purpose of this preliminary analysis. In future developments this approach should be abandoned in favour of a more accurate model of the heat transfer phenomena for the primary and intermediate loops in order to get a more accurate evaluation also of temperature extremes.

The starting conditions are given by the distributions of the variables obtained from the steady state simulation presented in Section 2.6. The transient case is run for 40 s, hence $8\,\tau$, with the ultimate goal is to examine as exhaustively as possible the new conditions at which the reactor stabilises after the transient. Thanks to the counteraction of the Doppler and thermal expansion feedbacks, the reactor should reach a new steady state in a given amount of time that could overcome the selected computational interval. Indeed, these coefficients provide the reactor with the appealing characteristic of inherent safety.

3.2.   Numerical results

Please note that, as previously mentioned, the time profiles for the transient cases are represented for the full core values, so the results of the power and the volumetric flowrates

obtained as outputs of numerical simulations of a 16th of the reactor are multiplied by 16, thereby exploiting the symmetry hypothesis underlying the choice of focusing only on a portion of the reactor.

The figure of merit for the transient ULOFF case is:

- volumetric flowrate time profile

- total power and power to flowrate ratio time profiles

- maximum temperature in the primary loop time profile

- mean temperature in the core time profile

- minimum temperature at the core inlet time profile

- temporal evolution of velocity and temperature distributions

- shortest and longest lived precursors distributions

First of all, the correct implementation of the pump coast-down in terms of the time dependence of the momentum source can be observed in Fig.3.1. In this figure, an exponential decay with a time constant of 5 s is also represented. It is possible to appreciate the difference in the profiles resulting from the inertia of the pump as well as the contribution provided by the natural circulation. This comparison corroborates the choice of imposing the time profile on the parameters of the momentum sources rather than the volumetric flowrate itself, as was discussed in Section 2.1.
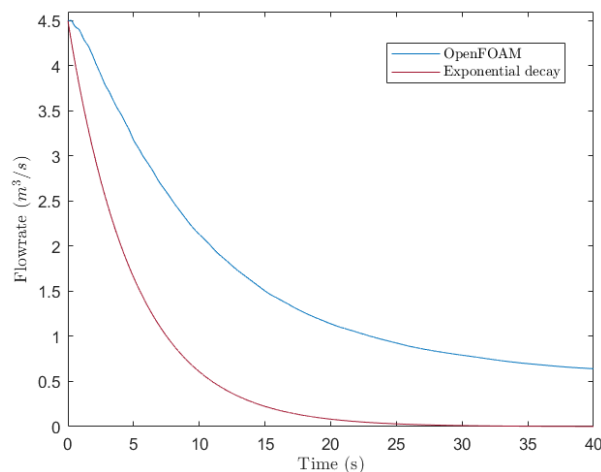
Figure 3.1: Volumetric flowrate time profile during the ULOFF transient.

The volumetric flowrate, indeed, exhibits an exponential drop that is not expected to fall to zero due to the buoyancy contribution that supports the onset of a natural circulation

regime. After 40 s,the value reaches 14.3 % of the initial nominal steady state value. It is worth reminding that this result is strictly dependent on the approximation made to represent the pump and the heat exchanger. A more accurate description should involve, for example, the modelling of pressure drops that influence the final steady state supported by the natural circulation. Therefore, once the design prescriptions are given, a more reliable value for the final volumetric flowrate can be assessed.

In the first instants of the transient, the failure of the pump leads to a reduction in the volumetric flowrate, an shown in Fig.3.1. According to the energy conservation equation this drop translates into an initial increment in the power-to-flow ratio, Fig.3.2b, causing the mean temperature of the core to increase, Fig.3.3c. Thanks to the negative temperature and density feedback effects triggered by the temperature rise in the core, the total power produced in the primary loop starts to decrease, but at a milder rate than the volumetric flowrate, also due to the precursors holding back. In fact, the time profile in Fig.3.2 reveals an ongoing increase with a declining rate in the final part of the transient for the normalised power-to-flow ratio, which is defined as:

$$\frac{\dfrac{Q}{\dot{V}\,\rho\,c_p}}{\dfrac{Q_{steady-state}}{\dot{V}_{steady-state}\,\rho\,c_p}} = \frac{Q}{\dot{V}}\,\frac{\dot{V}_{steady-state}}{Q_{steady-state}} \tag{3.2}$$

(a) Total power.   (b) Normalised power-to-flow ratio.
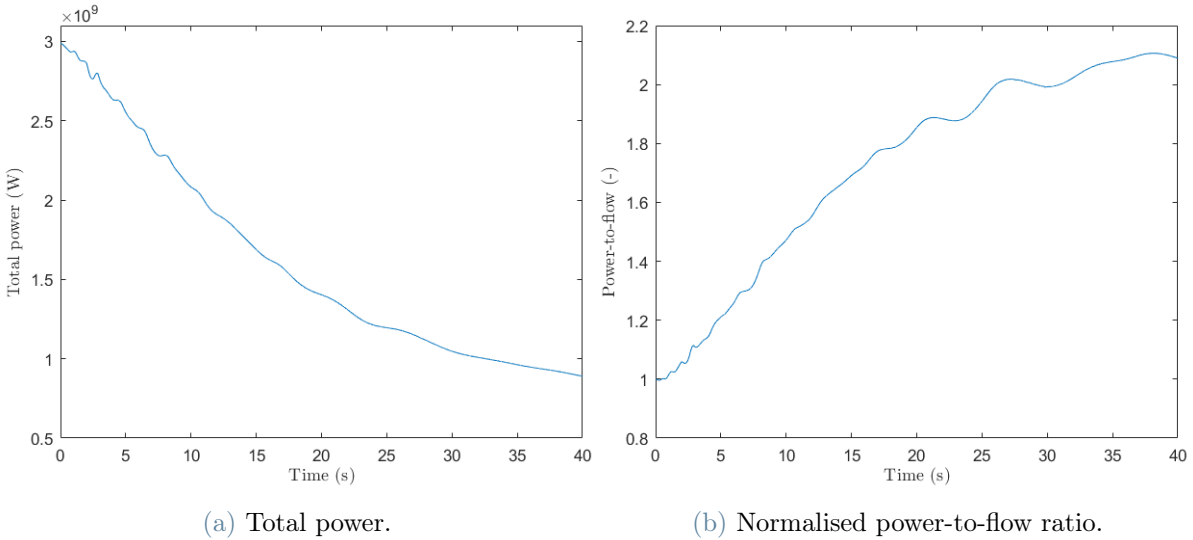
Figure 3.2: Power time profiles during the ULOFF transient.

According to the continuous rise of the normalised power-to-flow ratio, the mean tem-

perature keeps growing, as detailed in Fig.3.3c. As time progresses, the reduction of the total power persists, caused by the feedback effects, while the heat transfer to the intermediate loop is supported by the heat exchanger fixed properties and the development of the natural circulation regime, which drives the salt circulation despite the pump coastdown. These combined actions cause the mean temperature increase rate to slow down. Consequently, also the power slope decreases, as illustrated in the final part of the total power time profile in Fig.3.2a. Unfortunately, 40 s are not enough to reveal the level at which the reactor stabilises thanks to the thermal feedback coefficients, and at the end of the simulation, the power reaches 29.8 % of the steady state value, still with a negative slope.
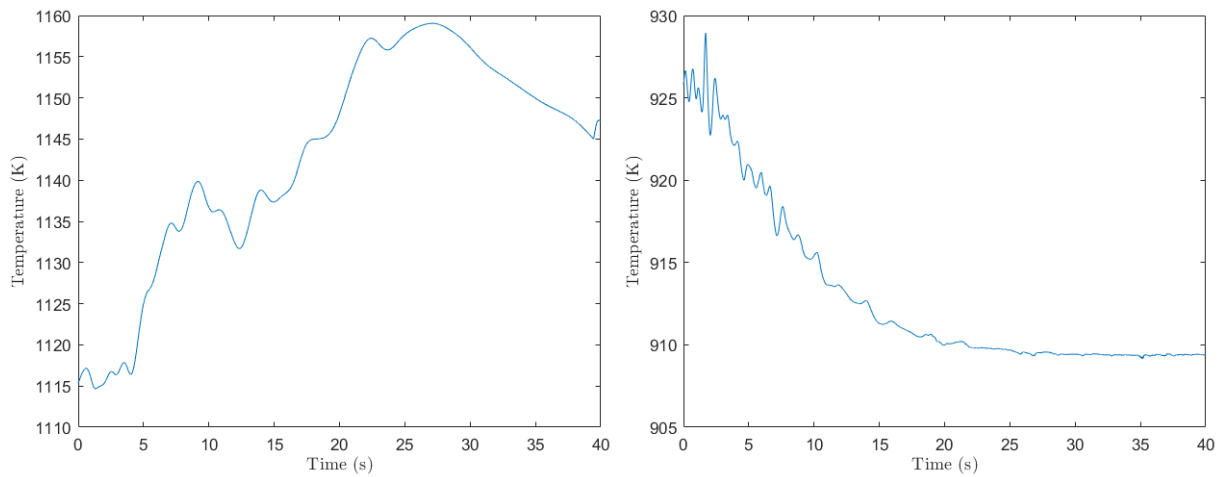
(a) Max temperature in the primary loop.

(b) Min temperature at the core inlet.
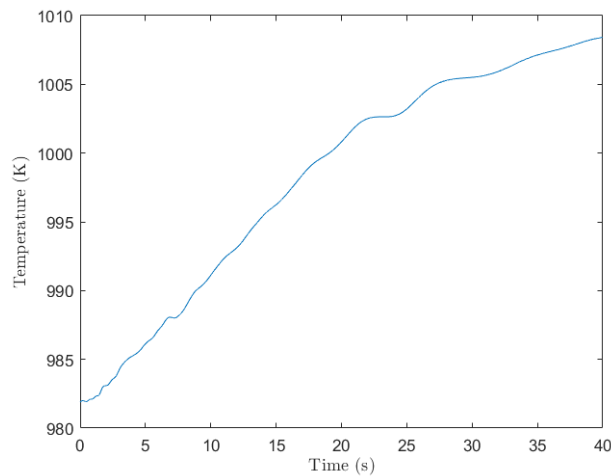
(c) Mean temperature in the core.

Figure 3.3: Temperature time profiles during the ULOFF transient.

The same consideration can be made for the mean temperature of the core, which at the end of the transient has not stabilised yet. Nonetheless, the approach to a new steady condition is suggested, in addition to the slower rate of change of the variables, by the time profile of the maximum temperature in the core, Fig.3.3a, which reaches a peak at $\sim$ 27 s and then begins to fall, indicating that the counteraction of the feedback coefficients has started to reverse the trend induced by the accidental event. The last plot of interest showns in Fig.3.3b the minimum temperature at the core inlet. During the transient, this temperature drops and stabilises at a value close to the constant intermediate salt temperature, $T_{ext} = 908\,K$ which acts as a constraint for the minimum temperature in the core. This tendency takes place as a result of the heat sink parameters remaining constant while the residence time of the fuel salt in the heat exchanger increases due to the reduced flow rate. It is worth noting that the modelling of the heat exchanger with a heat sink characterised by γ and T_{ext} allows to appreciate the reduction in heat removal provided by the heat exchanger. This degradation of the heat transfer, even with a constant global heat transfer coefficient, is coherent with the reduced power produced in the primary circuit.

The differences between the steady state values and the maximum (or minimum) value reached during the simulation are shown in Table 3.1, as well as the percentage increment (or decrement) with respect to the initial value for the minimum at the core inlet and the maximum and mean temperatures in the core.

		$T_{min,inlet}$	$\bar{T}_{core}$	T_{max}
ΔT	K	-16.66	+26.57	+43.72
$\Delta(\%)$	%	-1.80	+2.71	+3.92

Table 3.1: Temperature differences, absolute and percentage, between the steady state values and the extremes during the ULOFF transient.

As was previously discussed in Section 2.3, different oscillations are superimposed on the primary trends in each of the time profiles illustrated so far. Moreover, the curves demonstrate a more pronounced fluctuating behaviour where the dynamics of the reactor is faster and the rates of change of the variables are more accentuated. A deeper analysis deserves to be done in order to investigate and assign these oscillations to a specific cause, whether dependent on numerical and mesh issues or on the approximations intrinsic to the pump and heat exchanger representation and pre-implemented sources utilization. This inspection would provide the opportunity to assess if the oscillations could be reduced by adjusting the mesh or with a more realistic and detailed description of the two components.
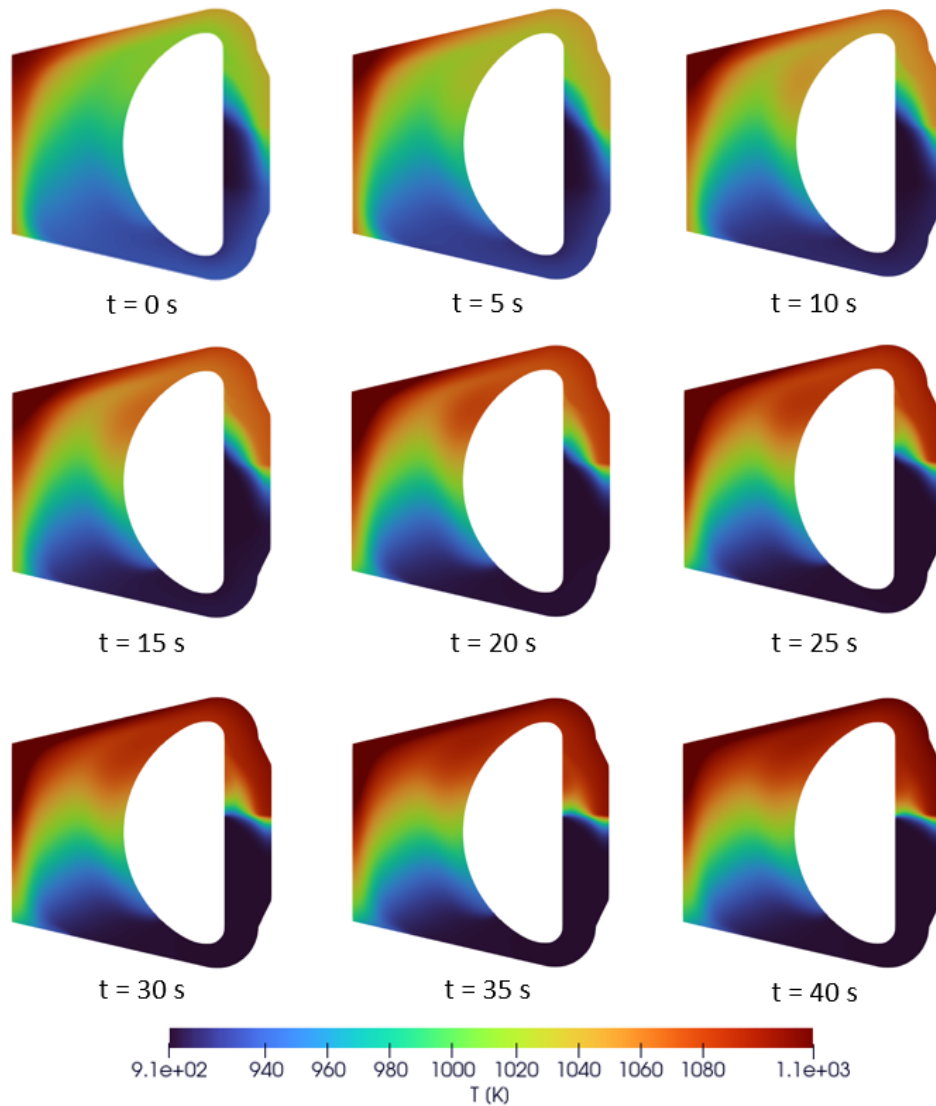
Figure 3.4: Temperature distribution for ULOFF accidental scenario taken every 5 s.

From the temperature distribution evolution, depicted in Fig.3.4 at the vertical midplane every 5 s, it is possible to infer that the maximum remains in the top centre part of the core throughout the transient. The region of higher temperatures expands as time progresses, leading to a boost in the thermal load to which the upper reflector is subjected. Also, the blanket wall is exposed to harsher thermal conditions. These outcomes emphasise the potential of exploiting a numerical simulation of a 3D domain with time dependent sources. Indeed, when dealing with safety assessment, the opportunity to evaluate the zones that would be more affected by an unintended event is extremely valuable for the design phase. The cold leg and the zone near the inlet of the core cool down but remain far from the freezing point of the fuel salt, where the melting point is 838 K [1]. Nevertheless, even this conclusion should be confirmed by an analysis involving a more detailed description

of the degradation of heat transfer capabilities including the response of the intermediate loop to the accidental event. From 30 to 40 s, the temperature distribution evolution is less evident, with the hottest zone in the top centre part of the core slightly fading away. As previously stated, the variable distributions in the pump and heat exchanger are not relevant in this thesis; but even so, it is interesting to note the net temperature jump between these two zones at 40 s, remarking the importance of design specifications to represent the distributions of variables accurately also in this critical interfacial region.
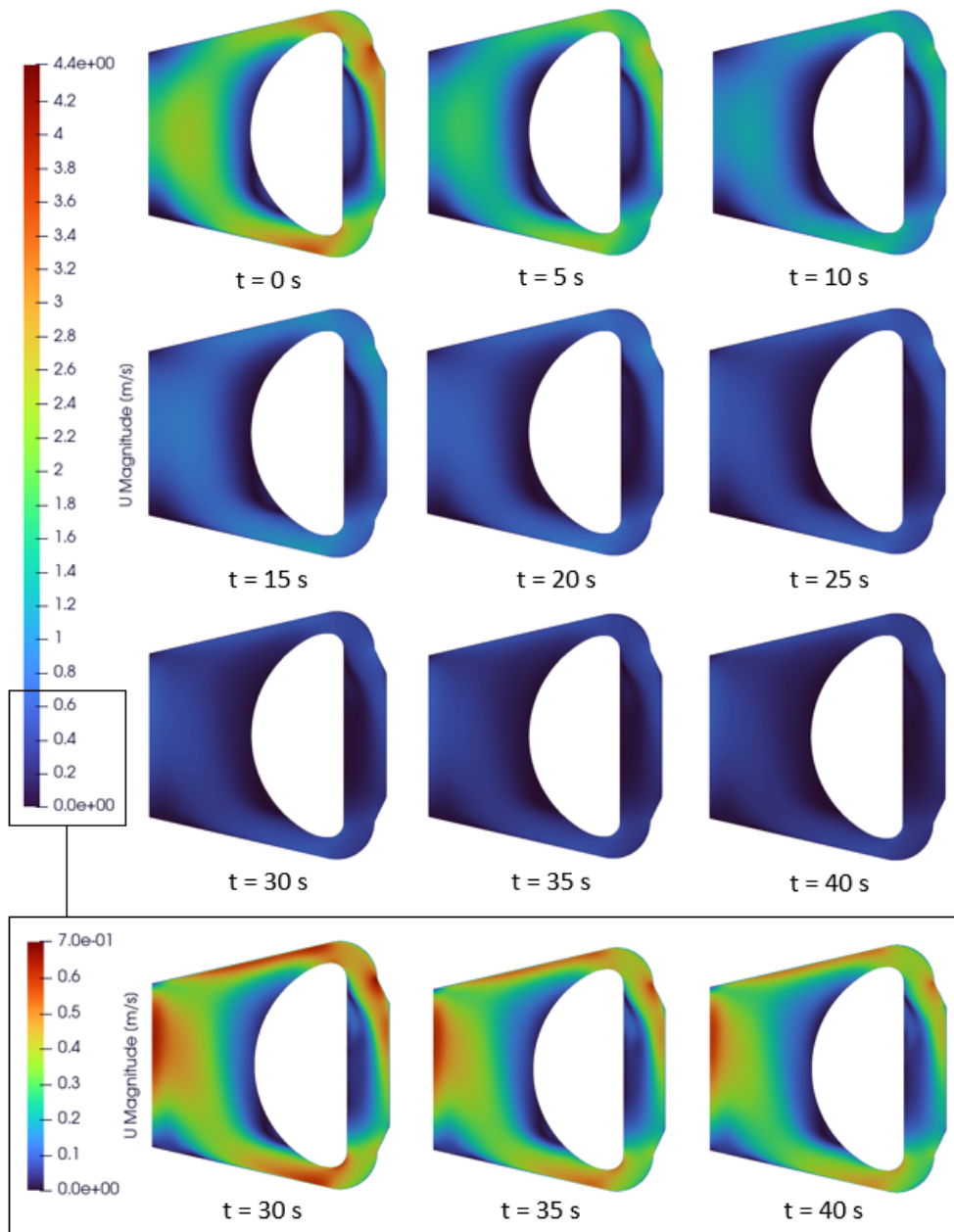
Figure 3.5: Velocity distribution for ULOFF accidental scenario taken every 5 s.

(a) Longest lived precursors. (b) Shortest lived precursors.
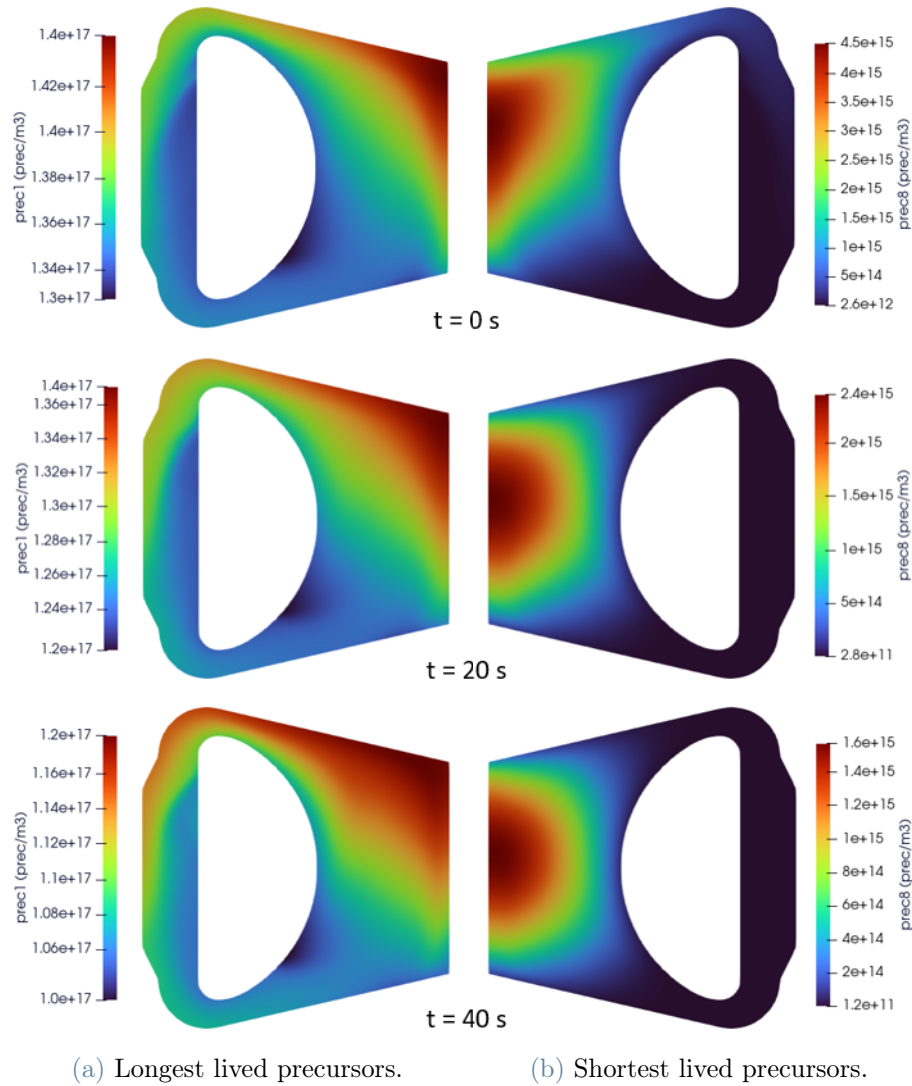
Figure 3.6: Precursors concentrations at 0, 20 and 40 s.

In Fig.3.5, the evolution of the velocity distribution at the midplane every 5 s is shown. The slowing down of the overall field is evident during the ULOFF accidental scenario, and a zoom in rescaling the colour legend for the last 10 s of simulation allows to highlight the contribution arising from the onset of natural circulation. Indeed, as the transient develops, the highest velocities move towards the central and upper parts of the reactor in correspondence with the hottest zones more affected by the temperature increase. At 40 s, the recirculation zone is still visible in the core, even if in this case the fluid salt is almost at rest next to the blanket wall.

The circulating liquid fuel, peculiar to the MSFR, results in delayed neutron precursors drift. Since the precursors are dragged by salt, a part of them will decay outside of the

core, causing a reduction in the delayed neutron fraction, β, with respect to a reactor with fuel at rest. When dealing with the ULOFF accidental scenario, the decline of the volumetric flowrate implies the precursors hold-back phenomenon. The subsequent minor loss of delayed neutrons from the core, related to the reduction of delayed neutron precursors decaying outside the core, contributes to the increase in the power-to-flow ratio. Therefore, in Fig.3.6, it is worth showing the change in the delayed neutron precursors distribution throughout the transient, at 0, 20 and 40 s. For the shortest lived precursor group, Fig.3.6a, the effect is to move the distribution toward the centre of the core, and at the end of the transient, the distribution assumes an almost symmetric shape, very similar to the distributions of the neutron fluxes. The longest lived precursor concentration, on the other hand, is more affected by the slowing down of the flow, Fig.3.6b, and at 40 s, this precursors group concentration occupies a large portion of the reactor core, expanding from the top centre part.

Finally, according to the thermal feedback coefficient estimation described in Section 2.7 which resulted in $\alpha_{thermal} = -5.645$ pcm/K it is possible to calculate the negative reactivity introduced by the Doppler and thermal expansion contributions. This evaluation is performed by multiplying the $\alpha_{thermal}$ coefficient by the mean temperature increase in the core from 0 to 40 s, namely $\Delta \bar{T}_{core} = 26.57$ K. The outcome is a reactivity variation of -150 pcm. In principle, when the new steady state is reached, this calculation should provide a value compensating the positive reactivity inserted by the precursors hold-back. In this regard, the evaluation discussed in Section 2.7 led to a positive reactivity insertion of 173.6 pcm when passing from a volumetric flowrate of 0.2818 m^3/s in the 16th of the reactor to 0 m^3/s, hence fuel salt at rest. Given that the natural circulation ensures a minimum fuel motion in this scenario, the flowrate never drops to zero, so a small part of the precursors dragged by the fuel can decay outside the core, implying that the positive reactivity insertion should be lower. The transient ends when these two reactivity variations are perfectly balanced.

4 | Unprotected Loss of Heat Sink

When dealing with safety assessment, a remarkable purpose of the accidental scenarios design is to embrace wide and representative case studies of dynamic reactor responses to unintended transient events, thus implying the necessity of spanning over the potential failure of all the components that constitute the power plant. In this perspective, after the simulation of a malfunction involving the primary circuit components, namely the Unprotected Loss of Fuel Flow, the investigation moves forward with an accident concerning the intermediate salt loop. In this case, the initiators could be a blockage or leakage in the intermediate circuit or a failure of the secondary pumps, all of which would result in a reduced mass flowrate as well as an increase in the intermediate salt temperature due to damage in the power conversion loop. In these cases, the heat transfer between the primary and intermediate salts deteriorates, or, in other words, the heat removal capabilities of the heat exchangers are lost, and the resulting accident is identified as Unprotected Loss of Heat Sink (ULOHS). In this thesis, two scenarios will be implemented: the former, more severe, will see an instantaneous drop to zero of the global heat transfer coefficient, while the latter, more realistic, will involve a time evolution of both the global heat transfer coefficient and the external intermediate temperature.

In Section 4.1 the simulation conditions and assumptions for both scenarios are detailed, while in Sections 4.2 and 4.3 the numerical results are separately commented.

4.1. Accidental scenario modelling

The degradation of cooling capabilities in the heat exchanger that is embedded in the ULOHS accident is simulated in this chapter according to two scenarios, referred to as *Case A* and *Case B*. Since this work focuses on the primary loop, which is also the simulation domain under consideration, these unintended transient events must be represented by imposing a given time profile on the heat sink parameters imposed in the heat exchanger zone of the 16th of the reactor, i.e., γ and T_{ext}. The other *SemiImplicitSource* parameter, which represents the primary pumps, is left at its steady state value for both cases, since the failure is assumed to affect only the components of the external loops. As

for the ULOFF, previously described in Chapter 3, both these accidental scenarios are considered unprotected and symmetric.

The starting conditions for both simulations are given by the distributions of the variables obtained from the steady state simulation presented in Section 2.6, and the cases are run for 40 s, hence 8 τ, with the intention to inspect the reactor's dynamic response and eventually verify the new steady state reached after the unintended transients. The outputs of interest presented in the following sections are:

- volumetric flowrate time profile

- total power time profile

- maximum temperature in the primary loop time profile

- mean temperature in the core time profile

- minimum temperature at the core inlet time profile

- temporal evolution of temperature and velocity distributions

4.1.1. *Case A*

The first scenario aims to represent a loss of flow for both sets of pumps that belong to the intermediate and power conversion loops. The combined failures cause a simultaneous flowrate reduction in the intermediate circuit, resulting in a deterioration of the global heat transfer coefficient, which is again taken into account in γ, and an increase in the intermediate salt temperature due to the loss of heat removal provided by the power conversion loop. In this more realistic case, which accounts for the inertia of the components undergoing malfunctions, the heat sink parameters, representing the heat removal concentrated in the heat exchanger zone, follow exponential time dependent profiles with a time constant, $\tau = 5$ s, for both γ and T_{ext}.

$$\gamma(t) = \gamma_0 - (\gamma_0 - \gamma_{end}) \cdot (1 - e^{-t/\tau}) \tag{4.1a}$$

$$T_{ext}(t) = T_{ext,0} + (T_{ext,end} - T_{ext,0}) \cdot (1 - e^{-t/\tau}) \tag{4.1b}$$

where $T_{ext,0} = 908\ K$, $T_{ext,end} = 961\ K$, $\gamma_0 = 5{\cdot}10^6\ W/m^3K$ and $\gamma_{end} = 1.68{\cdot}10^6\ W/m^3K$, so a reduction up to 33.6 % of the initial value, in accordance to previous simulations performed in the context of Horizon 2020 Euratom SAMOFAR project [30].

The numerical results of this simulation are presented in Section 4.2.

4.1.2. *Case B*

In the second scenario, a step reduction is imposed on the global heat transfer coefficient, which in this thesis is accounted for in the energy conservation equation by the parameter γ of the heat sink, which is forced to instantaneously fall to zero. This assumption implies that the heat removal provided by the heat exchangers is completely eliminated. This severe accident is intended to examine the reactor dynamics in the light of a conservative approach, at the expense of disregarding a realistic description of the unintended event, because a conductive mechanism could still provide a minimum heat transfer to the structural materials [30].

The numerical results of this simulation are presented in Section 4.3.

4.2.   Numerical results: *Case A*

First of all, in order to verify the correct implementation of the accidental scenario, with the primary pump working correctly, the volumetric flowrate in the primary circuit is shown in Fig.4.1. The constant value targeted at 4.5 m^3/s is superimposed by the oscillations mentioned in the previous chapters. The evolution in time of the velocity distribution, illustrated at 0, 20, and 40 s in Fig.4.2, allows to identify the origin of these fluctuations. In fact, despite the fact that the distribution in the core zone remains unaffected throughout the transient, a slightly different distribution at 20 s can be observed in the pump and heat exchanger zones, and this variation can be associated with flowrate oscillations. As previously indicated for the ULOFF simulation, a deeper investigation into the primary cause of this trend is necessary to identify appropriate improvement strategies, for example, modifying the mesh or more accurately characterising the primary loop components.
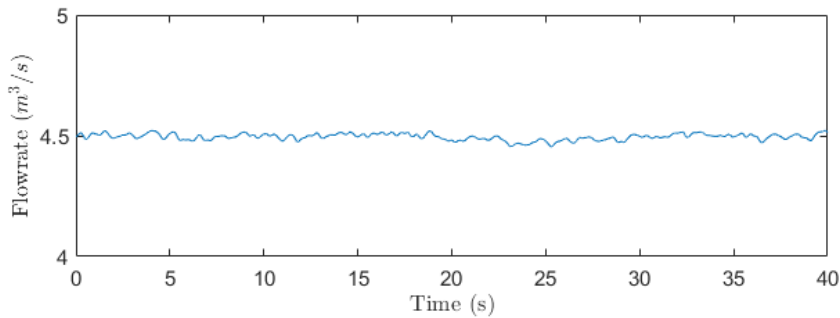
Figure 4.1: Volumetric flowrate time profile during the ULOHS (*Case A*) transient.
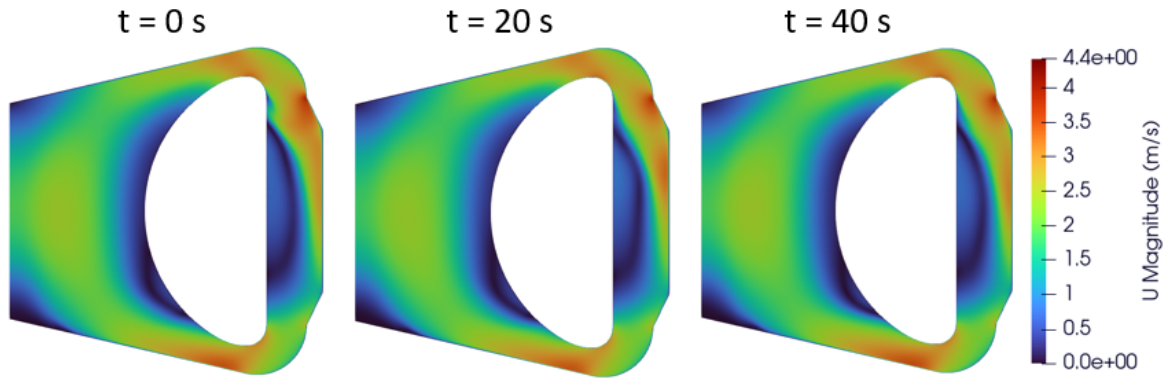
Figure 4.2: Velocity distribution for ULOHS (*Case A*) transient at 0, 20 and 40 s.

The first variable affected by the deterioration of the heat transfer between the primary and intermediate loops is the minimum temperature at the core inlet, which, as can be inferred from Fig.4.4b, starts to increase steeply in the first seconds of the transient. This increment is followed by the rise of the mean temperature in the core, which triggers the thermal feedback effects. Correspondingly, the total power produced in the primary circuit begins to decrease, and at 40 s, it reaches 20.82% of the initial steady state value, Fig.4.3. Since the flowrate is constant in this case, the power-to-flow ratio follows the same temporal evolution as the power, so it is not illustrated.
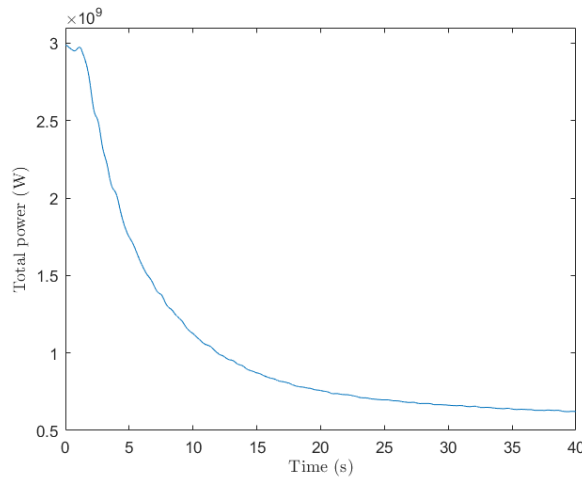
Figure 4.3: Total power time profile during the ULOHS (*Case A*) transient.

As time progresses, the decreasing power-to-flow ratio, induced by the feedback coefficients, contrasts with the increase in the mean temperature related to the progressive loss of cooling capabilities of the heat exchanger. As a result, Fig.4.4c demonstrates that the mean temperature in the core reaches a maximum at 15 s, then starts to decline but at

a milder rate with respect to the increasing part of the curve caused by the accident. To further inspect this tendency, Fig.4.5 presents mean temperature profiles at the core inlet and outlet, evaluated every 1 s, with the objective of describing the combined effect of the opposing phenomena of heat transfer deterioration and feedback counteraction rather than providing precise values. In this perspective, it is possible to verify that the curve of the average between the inlet and outlet temperatures replicates the profile of the mean temperature in the core. This plot shows how the increase in mean temperature at the core inlet, which dominates for the first 15 s, combined with the progressive decrease in mean temperature at the outlet results in a decreasing temperature difference between inlet and outlet, which is consistent with the lower power-to-flow ratio.
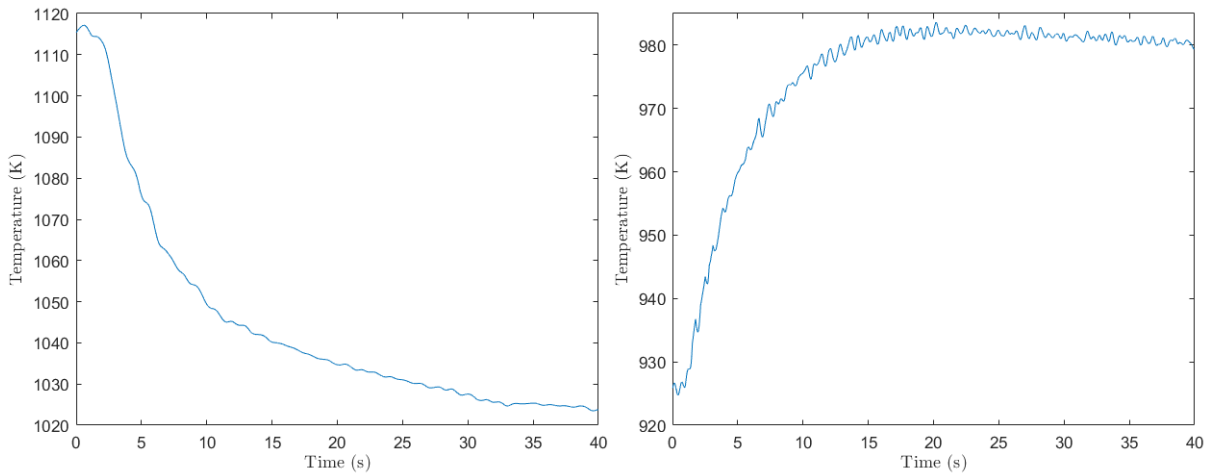
(a) Max temperature in the primary loop.   (b) Min temperature at the core inlet.
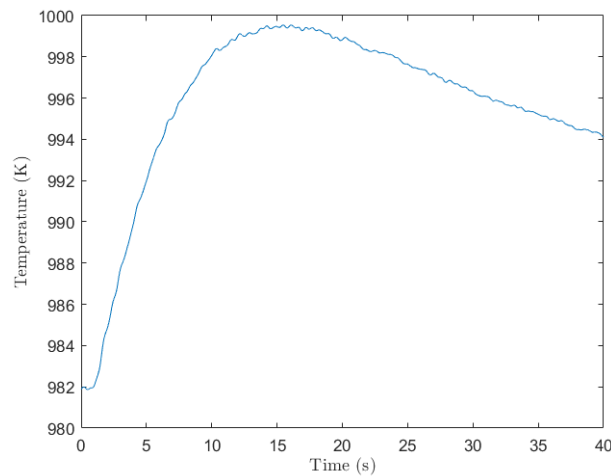
(c) Mean temperature in the core.

Figure 4.4: Temperature time profiles during the ULOHS (*Case A*) transient.
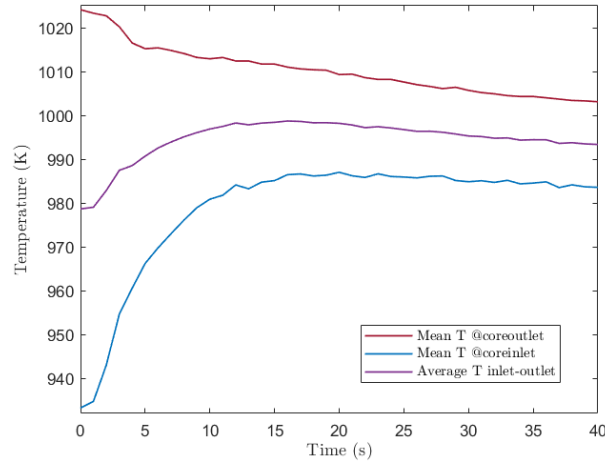
Figure 4.5: Mean temperature at the core inlet and outlet, and average between the two time profiles evaluated every 1 s for the ULOHS (*Case A*) transient.

Unfortunately, as for the ULOFF scenario, in this case 40 s are not enough to verify accurately the new steady state reached after the accident, since the mean temperature in the core is still decreasing at the end of the transient. In any case, the slopes for the time profiles of power and minimum at the core inlet and maximum temperatures are nearly flat at the end of the simulation, implying the approach to the new steady conditions. Furthermore, safety concerns are reduced because all the temperatures are decreasing at 40 s.

The differences between the steady state values and the maximum (or minimum) value reached during the simulation are shown in Table 4.1, as well as the percentage increment (or decrement) with respect to the initial value for the minimum at the core inlet and the maximum and mean temperatures in the core.

		$T_{min,inlet}$	$\bar{T}_{core}$	T_{max}
ΔT	K	+57.80	+17.65	-91.83
$\Delta(\%)$	%	+6.24	+1.80	-8.23

Table 4.1: Temperature differences, absolute and percentage, between the steady state values and the extremes during the ULOHS (*Case A*) transient.

A further comment can be focused on the maximum temperature in the primary loop which is definitely more influenced by the power-to-flow ratio reduction due to the feedback coefficients than the degradation of the heat removal that in any case is partially satisfied by the heat exchanger. As depicted in Fig.4.4a, after a small peak increase in the first 5 s of the transient, the curve demonstrates a decreasing trend.

Finally, it is worth mentioning that the minimum temperature at the core inlet is strongly affected by the choice of scenario modelling. In fact, the time functional dependence as well as the extreme values selected for the sink parameters, which are directly imposed on the fluid in the heat exchanger region, drive the evolution and the temperature level of the minimum temperature at the core inlet and, in turn, all the other temperatures. As a result, it is critical to carefully select these parameters and their temporal evolution, which embed the accidental scenarios, in order to obtain meaningful outcomes in terms of reactor dynamic behaviour and to accurately predict whether the safety limits for a variable of interest are met.
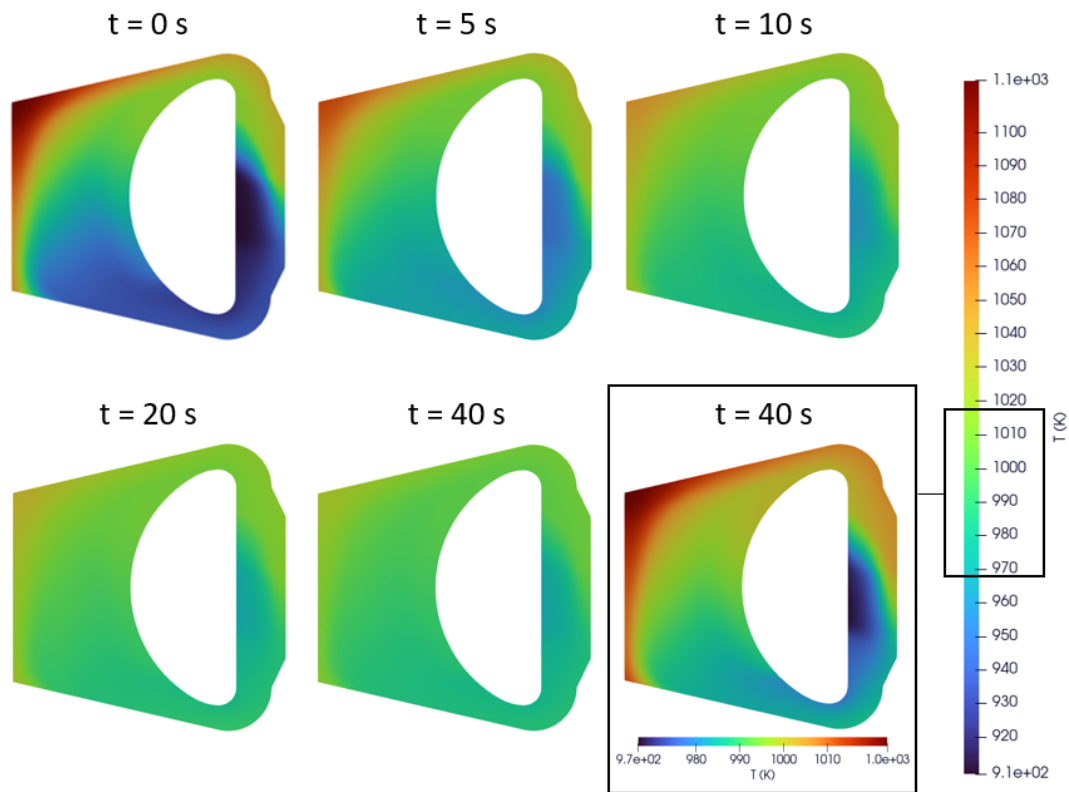
Figure 4.6: Temperature distribution evolution for ULOHS (*Case A*) accidental scenario taken at different time instants.

From the temperature distribution evolution, illustrated in Fig.4.6 at different time instants, it is possible to highlight how the temperature distribution becomes more uniform during the transient as the power-to-flow ratio decreases. Furthermore, it captures the decrease in maximum temperature in the circuit linked to the temperature drop at the core outlet. Finally, a zoom in on a smaller temperature interval at 40 s demonstrates that the distribution maintains its shape thanks to the proper operation of the primary pump, which forces the liquid fuel to circulate.

4.3.   Numerical results: *Case B*

As previously mentioned, the case study involves a step reduction of the global heat transfer coefficient that simultaneously drops to zero, leading to a fully adiabatic condition. This scenario is taken into account to interrogate the reactor with the most severe condition conceivable for a ULOHS, thus adopting a conservative approach, with the awareness that in a real scenario the heat conduction mechanism should provide anyway a minimum power removal through the structural material surrounding the reactor core.

First of all, as for the *Case A*, the volumetric flowrate time profile is plotted in Fig.4.7a together with a representative velocity distribution, evaluated at 20 s in Fig.4.7b, to demonstrate the correct implementation of the working state of the primary pump.
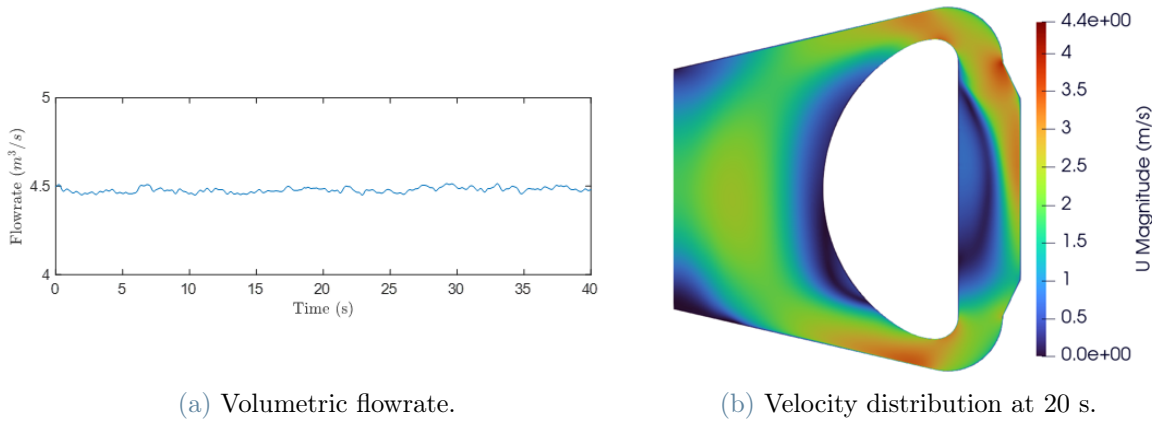
(a) Volumetric flowrate.

(b) Velocity distribution at 20 s.

Figure 4.7: Volumetric flowrate time profile during the ULOHS (*Case B*) transient.
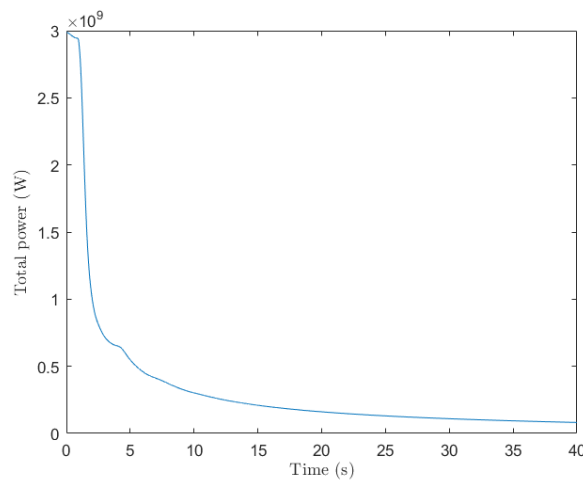
Figure 4.8: Total power time profile during the ULOHS (*Case B*) transient.

In Figs.4.9b and 4.9c, the minimum temperature at the core inlet and, as a result, the mean temperature in the core rise sharply, with a delay governed by the thermal inertia of the volume of salt contained in the primary circuit, which smooths out the effects of a sharp instantaneous discard of the heat sink. The temperature increase activates the counteraction of the thermal feedback effects, resulting in a rapid decline of the power produced in the primary loop as illustrated in Fig.4.8. From the initial part of this curve the effect of recirculation time of the MSFR can be appreciated. In the first 5 s of the transient the power drops to 18.35 % of the initial steady state value and gradually reaches 2.73 % at the end of the simulation.
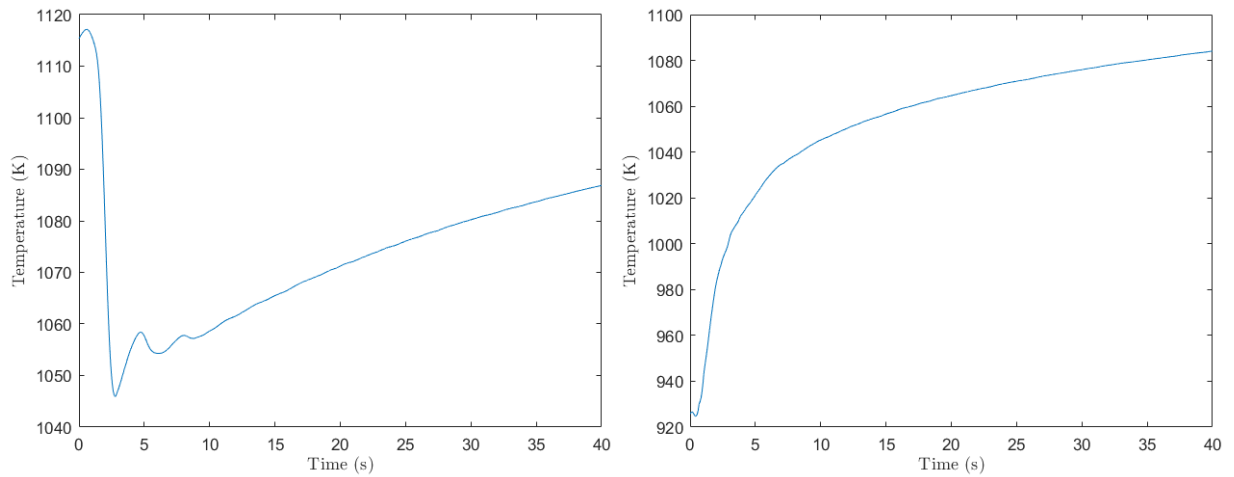
(a) Max temperature in the primary loop.

(b) Min temperature at the core inlet.
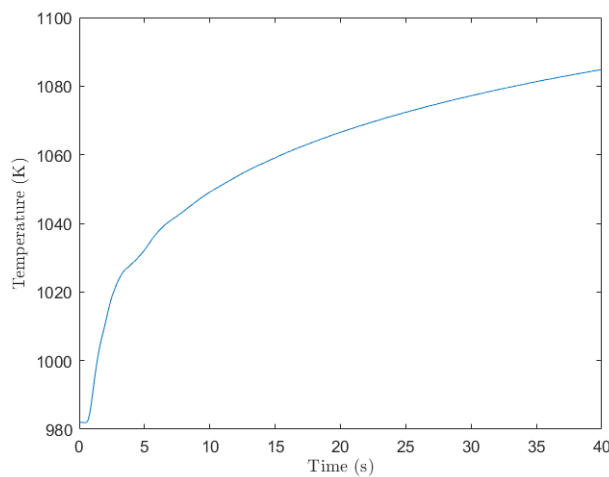
(c) Mean temperature in the core.

Figure 4.9: Temperature time profiles during the ULOHS (*Case B*) transient.

The absolute and percentage increments for the core mean and minimum temperature at the core inlet from steady state to the value reached at 40 s are reported in Table 4.2.

		$T_{min,inlet}$	$\bar{T}_{core}$
ΔT	K	+158.26	+102.93
$\Delta(\%)$	%	+17.09	+10.84

Table 4.2: Temperature differences, absolute and percentage, between the steady state values and the extremes during the ULOHS (*Case B*) transient.

Fig.4.9a demonstrates how the dramatic drop in power production in the primary loop leads to a marked decrease in the maximum temperature in the core. This temperature reaches 1046 K at ~2.8 s and then its trend reverses, showing a continual rise after 10 s up to 1087 K at 40 s. This initial decline coherent with the decrement in the temperature distribution at the core outlet shown in Fig.4.11.

As for the *Case A*, the plot shown in Fig.4.10 is meant to highlight the tendency of the mean temperature at the inlet and outlet of the core rather than to provide precise values. For this reason and for proper readability of the lines, the profiles are represented for the central part of the simulation interval. From this figure, it is possible to appreciate the curve of the average between inlet and outlet, which resembles the evolution of the mean temperature in the core and the progressive reduction in their difference in agreement with the reduction in the power-to-flow ratio resulting from a decreasing power and a constant flowrate.
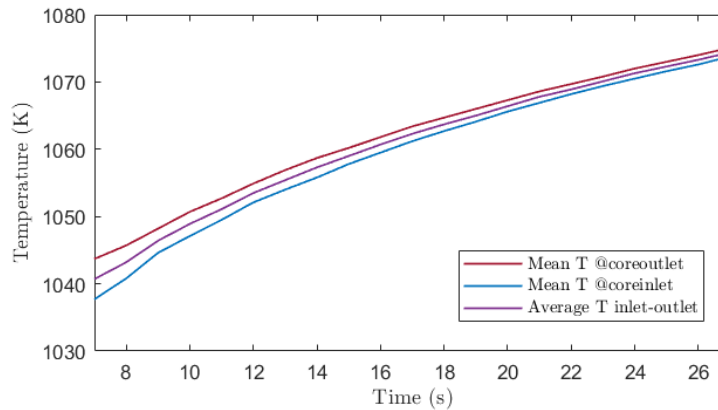
Figure 4.10: Mean temperature at the core inlet and outlet, and average between the two time profiles evaluated every 1 s for the ULOHS (*Case B*) transient.

Because the primary circuit is completely adiabatic and a residual amount of power is

still produced at the end of the accidental scenario, all the temperatures described so far are expected to maintain their increasing trend also after the 40 s, which is considered the simulation time interval. In any case, it is worth mentioning that the outcomes of this case study at the end of the transient still satisfy the safety limits imposed by the deterioration of the structural material performances subjected to harsh thermal working conditions. It would be interesting to let the simulation develop further in order to get an idea of the time required, or, from another perspective, the period allowed for maintenance intervention or safety mechanism activation, prior to actually overcoming selected safety requirements in the most hazardous conditions conceivable for a ULOHS event.

In Fig.4.11, the temperature distribution evolution is illustrated at different time instants during the accidental scenario. These time instants are chosen with the aim of highlighting the fast dynamic behaviour of the core in the first seconds of the transient. From the distribution evaluated at 1 s, the effect of the suppression of the heat transfer coefficient is clearly evident in the proximity of the core inlet and heat exchanger zone, where the temperature is subjected to a rapid increase. At 2 s, the decrease in the maximum temperature in the top centre part of the core along with an increase in the temperature field that expands from the inlet and involves all the core volume can be appreciated. From 10 s on, it is possible to note how the distribution becomes almost uniform in coherence with the reduced power-to-flow ratio and, in turn, the reduced temperature difference between the outlet and the inlet of the core. The zoom in, represented at 40 s in a range of a few K degrees, shows that the shape of the distribution, even in a reduced interval, maintains the same structure stemming from the primary pump working correctly, sustaining the circulation of the liquid fuel salt.

A final consideration to discuss is the comparison of the three accidental scenarios described in Chapters 3 and 4. Both the ULOFF and ULOHS scenarios demonstrate compliance with the safety limits imposed by the performance degradation of structural material subjected to unintended loads. Anyway, from all the graphs presented so far, it is possible to infer that the most concerning scenario from the safety point of view is the Unprotected Loss of Fuel Flow. This is due to the fact that in the case of the Unprotected Loss of Heat Sink at 40, the temperatures prove to be under control in the realistic case. Furthermore, the temperature distribution, even in a different range resulting from the loss of cooling capabilities, keeps its structure during the transient. On the contrary, in the case of a failure of the primary pump, the thermal loads affect non uniformly different parts of the reactor structural materials, subjecting a wider portion of the upper reflector and the blanket to harsher thermal conditions.
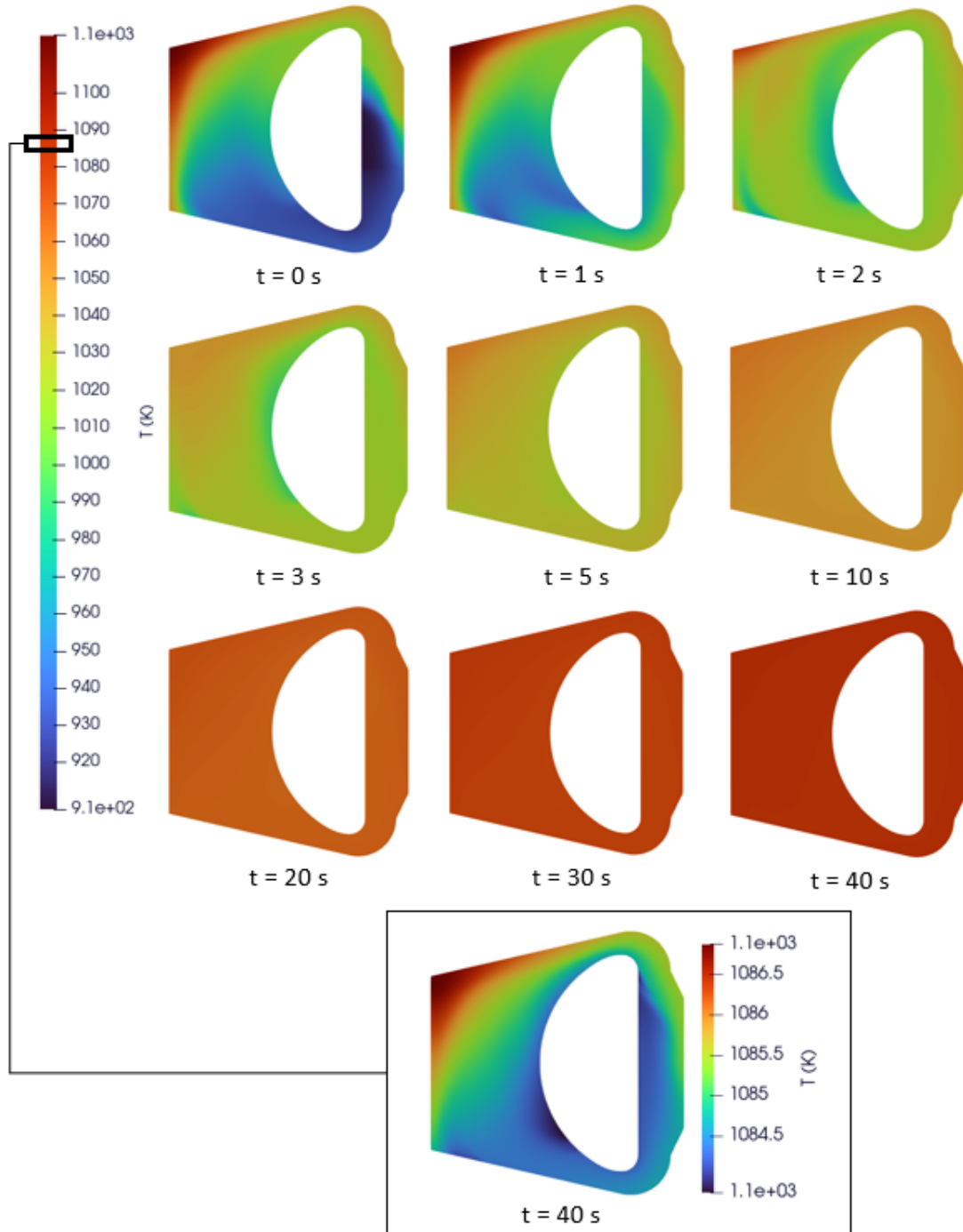
Figure 4.11: Temperature distribution evolution for ULOHS (*Case B*) accidental scenario taken at different time instants.

5 | Melting and solidification: preliminary analysis

This chapter is thought to provide a preliminary investigation into the correct implementation of the *phaseChangeMsfrPimpleFoam* solver presented in Section 1.6. In this new solver, the *msfrPimpleFoam*, which already embraces the multiphysisc approach by including in the same environment thermal-hydraulics and neutronics, is coupled with the solver that models the melting and solidification phenomena. The ultimate objective is to obtain a tool that could offer insight into one of the safety barriers with which the MSFR is equipped, namely the freeze valves. These solid plugs of salt are expected to melt in the case of an unintended temperature rise, allowing the discharge of the liquid fuel in Emergency Drain System. The dependence of the valve state and its progressive opening on the temperature evolution aligns with the concept of passive safety, thus justifying the interest in extending the numerical simulations in the direction of modelling the melting and solidification phenomena. An unique solver such as the *phaseChangeMsfrPimpleFoam* could provide a valuable tool to simulate simultaneously both the evolution of variables in the primary loop, with the *msfrPimpleFoam*, and the behaviour of the activated freeze valves. The possibility of assessing the reactor and freeze plug behaviours in the same simulation allows for an all-encompassing view of the accidental scenario.

The combined solver, implemented for OpenFOAM version 8, integrates two solvers previously developed at Politecnico di Milano and presented in Chapter 1 [3, 11, 13, 19]. The new *phaseChangeMsfrPimpleFoam* incorporates both the peculiarities of the *msfrPimpleFoam* solver as well as the numerical models to represent the latent heat and the velocity transition phenomena. Sections 5.1 and 5.2 test separately the two subsolvers, verifying them against case studies already available in the literature. In Section 5.3, a case study of a 2D cavity is proposed in order to perform a simulation that simultaneously implements all the physics involved.

5.1. Thermal-hydraulics and neutronics subsolver

Firstly, it seems useful to verify the *phaseChangeMsfrPimpleFoam* solver against a benchmark designed in the context of the Horizon 2020 Euratom SAMOFAR project, which aims to compare the performances of four multiphysics tools developed in different institutes, namely the Centre national de la recherche scientifique-Grenoble (CNRS), the Politecnico di Milano (Polimi), the Paul Scherrer Institute (PSI) and the Delft University of Technology (TUD)[21]. Since all the simulations resulted in good agreement, this case study is perfect to test the thermal-hydraulic and neutronic parts of the solver presented in this chapter.

5.1.1. Case study

The case study focuses on a 2D cavity where the different physics were coupled using a step-by-step approach in order to give an comprehensive comparison of the monophysics as well as the full coupling strategy adopted by the different institutes. In this section, the reference case corresponds to the step that simultaneously involves the thermal-hydraulics and neutronic parts of the solver, referred to as *Step 1.4: Full coupling* [21].

The salt under inspection is $LiF\text{-}BeF_2\text{-}UF_4$, whose properties, shown in Table 5.1, are considered constant with temperature and uniform throughout the domain. The salt is considered incompressible and laminar. Even if in this case the salt is kept in a liquid state, the *phaseChangeMsfrSimpleFoam* solver requires as input the melting parameters of the salt, i.e., the latent heat, L, and the melting temperature, T_m. The properties chosen for this simulation are considered representative values of a more complex phase transition [31, 32].

Parameter	Symbol	Value	Units
Density	ρ	$2.0\ 10^3$	kg/m^3
Volumetric Heat Capacity	c_p	$6.15\ 10^5$	J/ m^3 K
Laminar Viscosity	ν	$2.5\ 10^{-2}$	m^2/s
Latent Heat	L	$3.0\ 10^5$	J/kg
Melting Temperature	T_m	838	K
Thermal Expansion Coefficient	β	$2.0\ 10^{-4}$	1/K
Prandtl Number	Pr	$3.075\ 10^5$	-
Schmidt Number	Sc	$2.0\ 10^8$	-

Table 5.1: Thermal properties of $LiF\text{-}BeF_2\text{-}UF_4$.

As previously mentioned, the simulation domain is a 2D square cavity where the cooling is taken into account through a volumetric heat sink implemented with a *semiImplicitSource* in the form of:

$$q = \gamma \left(T_{ext} - T \right) \tag{5.1}$$

All the walls are considered adiabatic, and no slip boundary conditions are imposed except on the top wall, where a constant uniform velocity is fixed. For the neutronic part of the simulation, vacuum boundary conditions are imposed on the six energy groups in the multi-group diffusion approximation. In this case, the decay heat precursors are not solved, while eight groups represent the delayed neutron precursors. The relevant simulation parameters are reported in Table 5.2.

Parameter	Symbol	Value	Units
Nominal Power	Q	1000	MW_{th}
Top wall velocity	U_{lid}	0.5	m/s
External Temperature	T_{ext}	900	K
Heat sink parameter	γ	$1 \cdot 10^6$	K
Cavity side	l	2	m

Table 5.2: Simulation parameters [21].

5.1.2. Numerical results and verification

Fig.5.1 illustrates a comparison for different variables between the cavity treated with the *phaseChangeMsfrPimpleFoam* and the Polimi benchmark case in the *Full coupling* step. The outcomes for temperature, velocity, 1st and 5th delayed neutron precursors groups show an essential agreement in terms of the distributions of variables marked by stream lines and iso-lines with the same intervals. Minor discrepancies can be highlighted for the decay neutron precursors 1st and 5th families but they can be attributed to slightly different power produced in the cavity due to the fact that the *phaseChangeMsfrPimpleFoam* solver, being based on the *msfrPimpleFoam* transient solver, does not implement the power iteration routine. To overcome this issue, a steady state simulation is run in advance with the *msfrSimpleFoam* solver in order to get an estimate of the effective multiplication factor, which is then imposed on the actual cavity simulation.

(a) Temperature   (b) Velocity

(c) Precursors 1st group   (d) Precursors 5th group
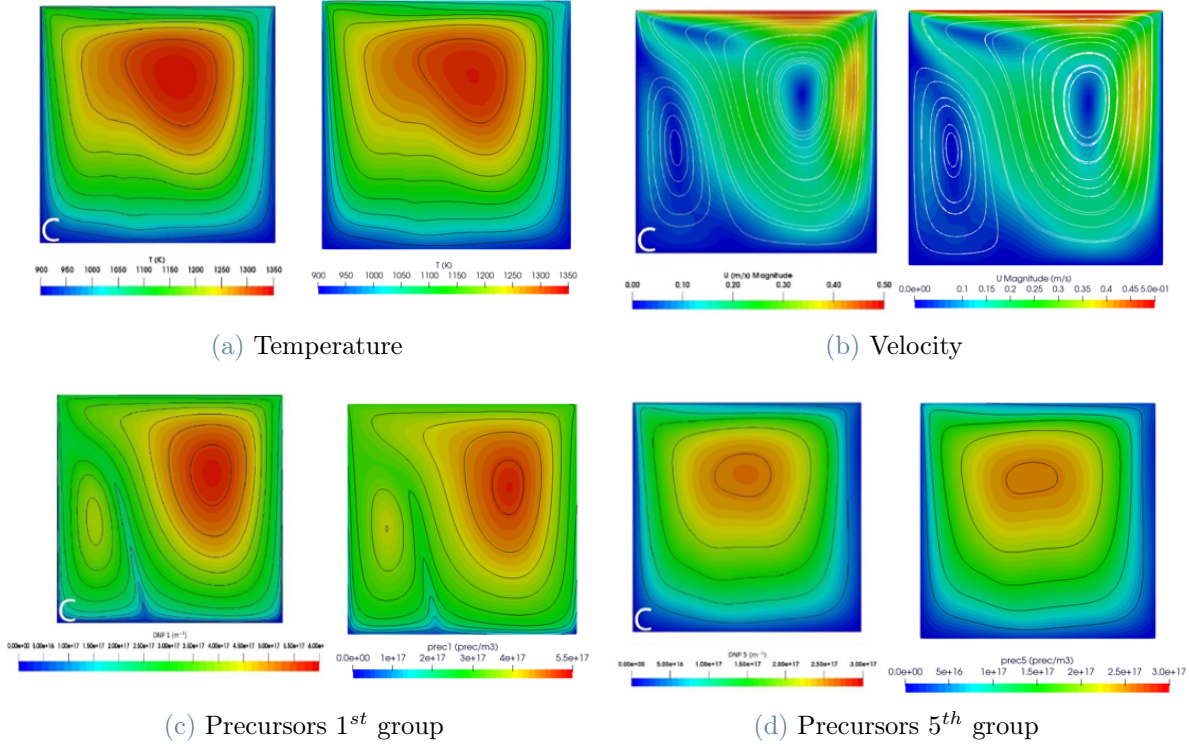
Figure 5.1: Comparison of different variables between the benchmark case (marked by a C [21]) on the left and the *phaseChangeMsfrPimpleFoam* on the right.

5.2.   Melting subsolver

For what concerns the modelling of melting and solidification phenomena, the original solver was presented in Section 1.5. In this section, the unified *phaseChangeMsfrPimpleFoam* is tested against a case study meant as a reference numerical solution for phase change problems involving convection modelled through an enthalpy based approach [33]. This selected benchmark is the same as that adopted at the Politecnico di Milano [13] to verify the correct implementation of the convection melting subsolver, which is instead temperature based. The choice of exploiting the same benchmark is done to ensure that while coupling the two subsolvers, neither of them is corrupted.

5.2.1.   Case study

The case study consists of a square tin heated from the left side at a fixed temperature of T_h starting from an internal temperature of T_0, corresponding to the melting temperature, T_m. In this case, the initial temperature is slightly lower in order to favour the development of the mushy zone, in accordance with what was done also at the Politecnico di Milano.

The temperature of the right side of the cavity is kept constant.

The relevant simulation parameters are presented in Table 5.6, whereas the material properties are reported in Table 5.4, and they are taken to be equal for solid and liquid phases. The flow is assumed to be incompressible and laminar, and the *Source Term Method* is adopted in combination with a linear relation between temperature and volume liquid fraction. For what concerns the neutronic part of the simulation, the *phaseChangeMsfrPimpleFoam* solver allows to decouple the neutronic and therm-hydraulics physics by turning off a flag that imposes in the energy equation the neutronic power produced as a volumetric source. Moreover, all the fluxes and precursors concentrations must be fixed to zero in order to prevent the divergence of the simulation.

Parameter	Symbol	Value	Units
Hot Wall Temperature	T_h	508	K
Cold Wall Temperature	T_c	504.49	K
Internal Temperature	T_0	504.49	K
Mushy zone width	dT	0.5	K
Cavity side	l	0.1	m
Darcy source term constant	C	$2.8 \ 10^{10}$	$1/\text{m}^2$

Table 5.3: Simulation parameters [13].

Parameter	Symbol	Value	Units
Density	ρ	$7.5 \ 10^3$	kg/m^3
Specific Heat Capacity	c_p	$2.0 \ 10^2$	J/ kg K
Thermal conductivity	k	60.0	W /m K
Dynamic Viscosity	μ	$6 \ 10^{-3}$	kg/ m s
Melting Temperature	T_m	505.0	K
Latent heat	L	$6.0 \ 10^4$	J/kg
Thermal Expansion Coefficient	β	$2.67 \ 10^{-4}$	1/K
Prandtl Number	Pr	$2.0 \ 10^{-2}$	-
Schmidt Number	Sc	$2.0 \ 10^6$	-

Table 5.4: Tin parameters for the melting problem [33].

5.2.2.   Numerical results and verification

As the temperature on the left side is set 3 K higher than the melting temperature at the beginning of the simulation, it is possible to appreciate the phase change of the solid

cavity. The buoyancy effects support the onset of the natural circulation, which results in the development of a roll pattern characterised by a different number of rolls, starting from a growing convection cell that splits into other cells as the time progresses.

Fig.5.2 depicts a comparison between the simulation run with the *phaseChangeMsfrPimpleFoam* solver and the benchmark case. Stream lines are added to Fig.5.2b in order to highlight the multiple eddies developed during the simulation. The evolution of the liquid structure is in great agreement, as is the wave-like advancing melting front. The only difference can be found in the time at which the "three-rolls" pattern is fully established, namely 50 s earlier for the reference case.
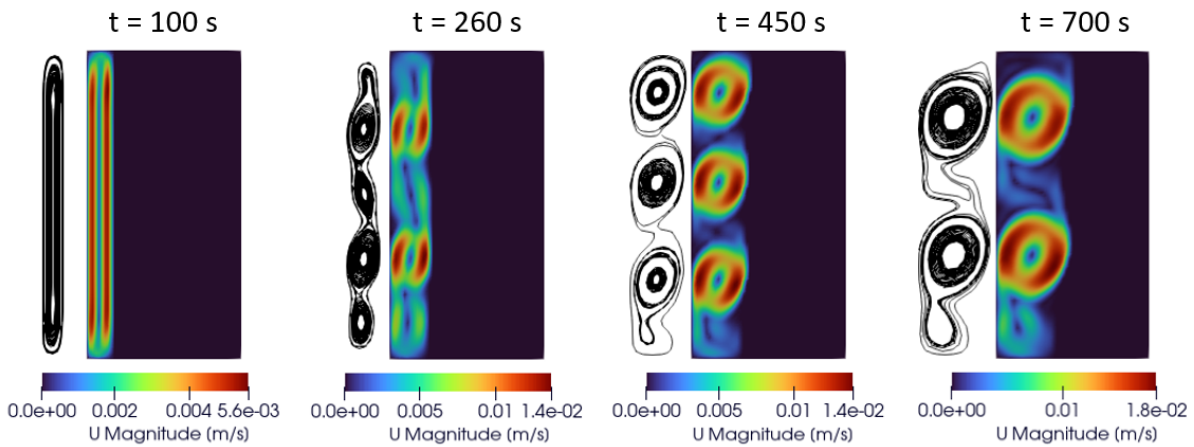
(a) *phaseChangeMsfrPimpleFoam*
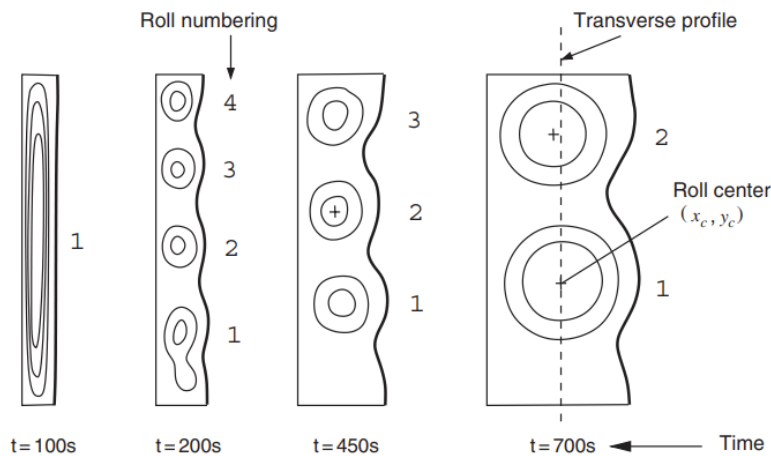
(b) Reference case [33].

Figure 5.2: Comparison of roll patterns in the melt at several times.

5.3.   Cavity solidification

This section is meant to verify the correct coupling performed by the *phaseChangeMs-frPimpleFoam* solver through a simulation that requires the solution of all the physics involved. The objective is to assess whether the multiphysic solver returns physically reasonable outcomes. In this light, the parameters of the sources and the thermal properties are chosen in order to highlight the various phenomena modelled.

The case study consists of a 2D cavity, inspired by the benchmark presented in Section 5.1, with some ad hoc modifications. The properties of the salt and of the cavity considered are the same as the benchmark ones, and changes are made aiming to favour the development of the solid layer due to the solidification of the salt next to the walls. In order to obtain an overall lower temperature distribution in the cavity, closer to the melting temperature, the nominal power is reduced, as shown in Table 5.6. Furthermore, the external temperature characterising the heat sink is lowered, and on the bottom wall, a uniform temperature of 733 K is fixed. On the top wall, a uniform velocity of 0.5 m/s is imposed.

Parameter	Symbol	Value	Units
Nominal Power	Q	500	MW_{th}
Bottom wall temperature	T_{bottom}	733	K
External Temperature	T_{ext}	835.85 K	K
Melting Temperature	T_m	838	K

Table 5.5: Parameters for the coupled problem [33].

A step-by-step approach is employed in order to emphasise the influence of the melting parameters on the distribution of variables. Table 5.6 represents the variation of the melting temperature and the heat sink temperature from one simulation to another.

		(a)	(b)	(c)
T_m	K	838	852	852
T_{ext}	K	835.85	835.85	829.7

Table 5.6: Melting temperature and external temperature of the heat sink for the coupled solidification simulation.

The first simulation, referred to as *Case (a)*, is run while keeping the salt in a liquid state, thus ensuring a temperature field higher than 838 K. In this case, the only salt that

undergoes a phase transition is in correspondence of the the cold bottom wall. Indeed, in Fig.5.3a, it is possible to appreciate that in the first layer of cells the liquid fraction is zero, corresponding to a solid state for the salt. The temperature distribution is similar to the benchmark in Section 5.1, but scaled to lower values as expected. The fission power produced in the cavity is 517 MW, so the neutronic part is solved properly. Then, in order to test that the solidification numerical model reproduces coherently the stratification of the solid layer, the melting temperature is raised to 852 K. In this condition, the region where the temperature is lower than T_m is extended. As a result, a solid layer also develops on the sides of the cavity and in the lower corners, as shown in Fig.5.3b. Correspondingly, the velocity in this region drops to zero, leaving unaffected the distribution in the internal part of the cavity.

(a)   (b)   (c)
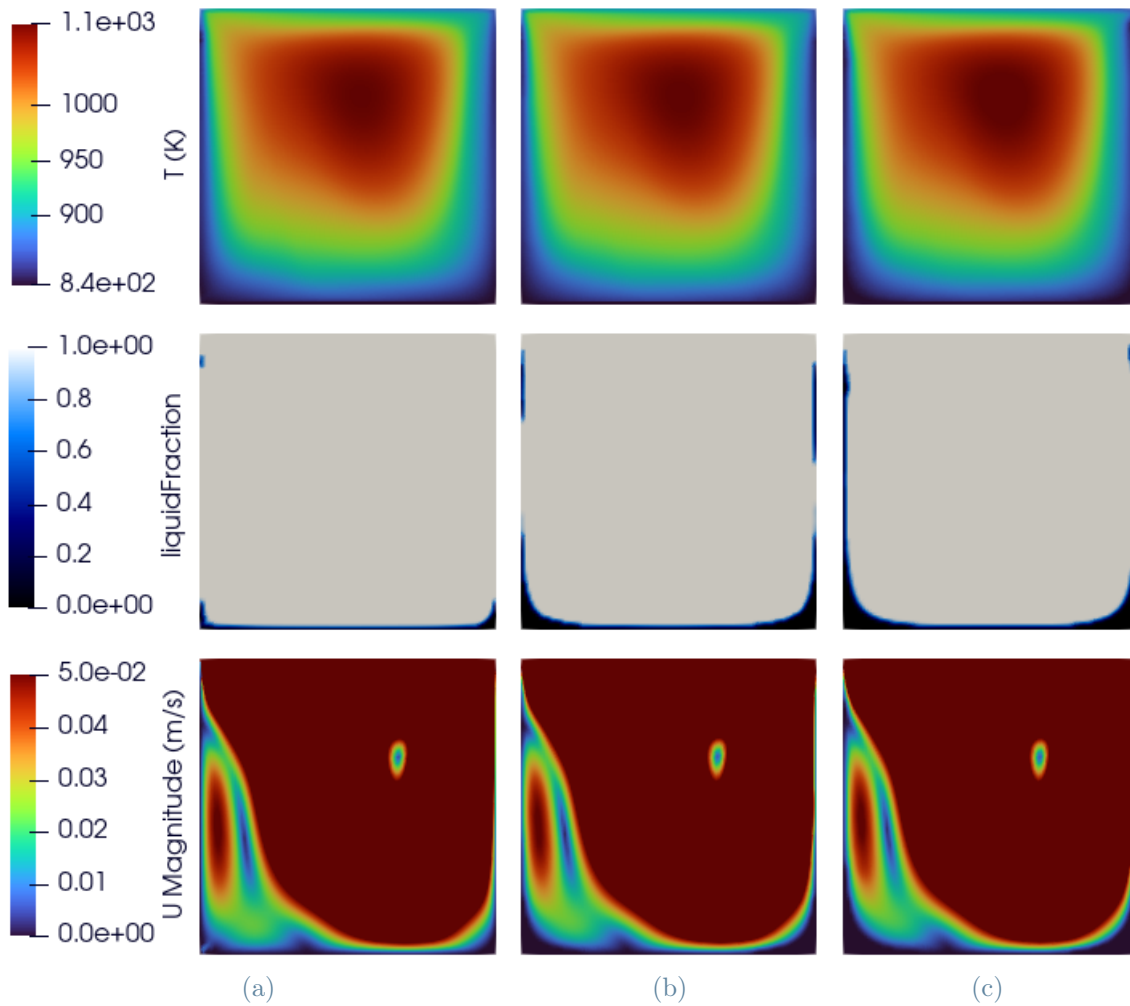
Figure 5.3: Temperature (on top), liquid fraction (in the middle), and velocity (on bottom) distributions of the cavity solidification simulation.

At 300 s, the external temperature, T_{ext}, is lowered to 829.7 K. This decrement leads to a higher heat removal by the heat sink and thanks to feedback coefficients the power produced inside the cavity follows, stabilising at a higher value of 539 MW. The advancement of the solid front is shown in Fig.5.3c due to a lower temperature at the walls. The solid layer covers a more extended part of the bottom corners and almost all the sides of the cavity, with the exception of the upper part next to the wall where a non null the velocity is imposed. Also in this case, the *Darcy Source Term* forces the velocity to zero in correspondence to the solid layer.

This analysis set the ultimate goal of verifying the correct implementation of the unified *phaseChangeMsfrPimpleFoam* solver. The attractiveness of including the melting and solidification phenomena in the transient solver is based on the potential to investigate the behaviour of the freeze valves. As previously mentioned, this innovative safety barrier could provide an essential counteraction to an unintended temperature rise, allowing the discharge of the fuel salt in the Emergency Drain System. In order to give an idea of what could be a first case study on this safety component, Fig.5.4 illustrates a geometry including the 16th of the reactor with a cylinder attached on the bottom in correspondence with the cold leg to mimic the presence of the solid plug. The *phaseChangeMsfrPimpleFoam* should be able to simulate simultaneously the accidental scenario in the core and the melting of the state of the freeze plug, activated in response to the unintended event.
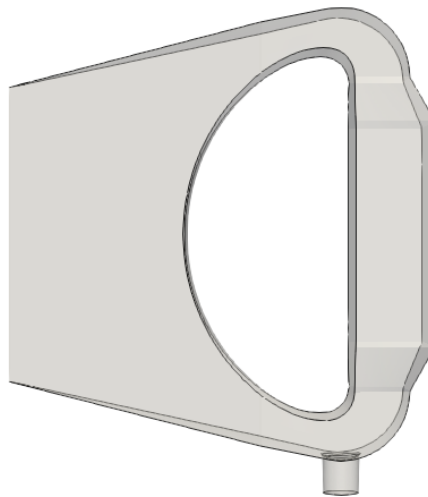
Figure 5.4: Geometry of the 16th with a freeze plug.

6 | Conclusions and future developments

In this thesis, the behaviour of the MSFR in nominal operation and accidental scenarios is analysed in order to assess the conditions on the containment of the reactor. The efforts are pursued to evaluate the harsh working requirements to which the reactor is subjected, in terms of thermo-mechanical loads and irradiation. To achieve this goal, multiphysics solvers, coupling in the same environment thermal-hydraulics and neutronics, are employed for transient and steady state simulations. In this context, to best exploit the time dependent pre-implemented sources available in the OpenFOAM toolkit, all the solvers are updated to version 8. Furthermore, starting from two solvers developed at the Poliecnico di Milano, a new solver, i.e., *phaseChangeMsfrPimpleFoam*, is implemented. This tool allows for the treatment of both the reactor dynamics and the melting and solidification phenomena in the same case study. This coupling provides the valuable opportunity to extend the simulation domain from the primary circuit only by incorporating in the same simulation also the behaviour of freeze valves. The solid plugs constitute a safety barrier that can be activated during an accidental event. As a result, the shortlist of case studies that can be investigated with numerical simulations could be extended. The simulation domain consists of a 3D representation of the primary loop that allows for the capture of flow structures and the positions of the most critical points in steady state and accidental scenarios.

For what concerns the steady state simulations, aimed at evaluating the nominal operating conditions, it is possible to draw some conclusions in terms of modelling choices. Firstly, a proper choice of the geometry of the domain allows to reduce the salt recirculations present inside the core. Nevertheless, for the cases analysed, only minor differences are found in the distributions of variables. Furthermore, the flexibility to inspect different geometries can be a valuable tool during the design phase and optimisation. Secondly, a proper mesh refinement and generative algorithm not only lighten the computational burden of the simulation but also allow for a decrease in the amplitude of numerical oscillations that may spoil the operative parameters even at steady state. Thirdly, the turbulence

models k-ω *SST* and *Realizable* k-ϵ prove to be in good agreement in terms of volumetric flowrate magnitude and velocity distribution. Finally, the boundary conditions imposed on the neutronic part of the simulation affect the shape of the power density profile both radially and axially. Albedo boundary conditions, which mimic the presence of the reflectors and the blanket, lead to more flat profiles with respect to vacuum boundary conditions. These steady state simulations allow also to verify that the thermal feedback coefficient, accounting for the Doppler and the thermal expansion effects, is coherent with the reference found in the literature. Moreover, the reactivity insertion resulting from the precursors hold back in a stagnant condition with respect to the drift induced by the circulating fuel is evaluated. In summary, the multiphysics solver, together with the mesh and the tools pre-implemented in the OpenFOAM version 8 toolkit, allows to appreciate the thermo-mechanical loads and irradiation conditions of the reactor. Indeed, the steady state distribution of variables compliant with the requirements designed for the nominal operating conditions can be satisfactorily assessed.

In order to evaluate the dynamic behaviour of the reactor in response to an accidental event, the transient solver is exploited. Moreover, time variant formulations are employed for the parameters characterising the source and sink, representing the pump and heat exchanger, respectively. In the event of an Unprotected Loss of Fuel Flow, so a failure of the primary pumps, the power drops due to the counteraction of the thermal feedback coefficients. The feedback effects are triggered by the mean temperature rise due to an initial increase in the power-to-flow ratio and the contribution of the precursors hold back. As time progresses, the mean and maximum temperatures keep rising, whereas the minimum temperature at the core inlet decreases. The region of hottest temperatures extends during the transient, affecting a larger portion of the upper reflector and the blanket. At the end of this accidental scenario, the slopes of the profiles are milder as a result of the counteraction of the feedback coefficients. In 40 s, it is not possible to define the new steady state reached thanks to a balance between the reactivity inserted by the precursors hold back and the counteraction of feedback coefficients. The Unprotected Loss of Heat Sink is simulated with an exponential reduction of the global heat transfer coefficient and an increase in intermediate salt temperature. In this case, the increase in the minimum temperature at the core inlet and, in turn, the mean temperature in the core trigger the feedback effects. As a result, the power declines. The mean temperature in the core shows an increasing trend, which is then reversed due to the drop in the power-to-flow ratio, contrasting the deterioration of cooling capabilities. All temperatures evaluated stay well below the safety limits required for structural material subjected to unintended harsh thermal loads. On the other hand, an instantaneous drop to zero of

the global heat transfer coefficient results in a steep power decrease. This decline is related to the marked increase in the mean temperature, caused by the absence of heat removal by the heat exchanger. The maximum temperature in the core shows an initial violent drop. Anyway, all the temperatures after some seconds demonstrate an increasing trend and are expected to keep rising as time progresses, even after the 40 s simulation interval. For all the scenarios mentioned, the 3D geometry and the multiphysics solver, able to include time variant sources, allow to catch the main phenomena resulting from the response of variables to an unintented event. In all cases, the safety limits imposed by the performance degradation of structural materials subjected to accidental thermal loads are respected within the simulation interval of 40 s. The most concerning scenario involves the failure of the primary pumps, i.e., ULOFF, since at the end of the realistic ULOHS all the temperatures are decreasing and the distribution of temperature keeps its original structure.

In the final part of the thesis, the preliminary verification of the correct implementation of *phaseChangeMsfrPimpleFoam* solver is assessed. Firstly, the simulations run to test single parts of the solver demonstrate a great deal of agreement with the selected benchmark cases. Then a case study involving the solution of all the physics involved proves the correct coupling of the neutronics, thermal-hydraulics, and phase change phenomena. The interest in extending the solver in the direction of melting and solidification phenomena is related to the objective of analysing the behaviour of the freeze valves. This innovative safety barrier is based on the possibility of melting the solid salt plugs in the event of an unwanted rise in temperature. The mechanism based on the state of the plug aligns with the approach of passive safety, justifying the attractiveness of deepening the knowledge of the behaviour of freeze valves.

Regarding future developments, the sensitivity analyses performed on the primary loop 3D domain state the necessity of design prescriptions for the pump and the heat exchanger. A more accurate description of these components would allow first to evaluate the distributions of variables and the pressure drops in those zones. Furthermore, it could lead to a more detailed description of the transient accidental scenarios and, in turn, provide more precise values of the extremes reached during the transients. In this context, it could be useful to represent the dynamic behaviour of the intermediate and power conversion loops in order to improve the assessment of the evolution of the main operational parameters of the core. A more realistic geometric representation of the pipelines and inlet and outlet of the core could help to deepen the knowledge of the flow structures developed inside the core, among which recirculation and almost stagnant zones. In this regard, a detailed analysis of turbulence, for example by exploiting LES, could allow the source of

the oscillations previously discussed to be identified. A material prescription could lead to a closer examination of the harsh working conditions to which the structural material is subjected, evaluating the thermo-mechanical loads and irradiation conditions in order to favour the design phase. Finally, for what concerns the melting and solidification, a possible future development lies in building a geometry that includes a region that mimics the presence of the solid plug attached to the lower part of the reactor in correspondence with the cold leg. In this case, a proper selection of boundary conditions could allow for the simulation of the melting of these valves during an accident where the discharge of salt is necessary. As a result, the shortlist of case studies that can be investigated with numerical simulations would be extended. In this context, it could be interesting to extend the solver with a multiphase approach in order to simulate the melting of the valves and the discharge of the molten salt.

Bibliography

[1] M Allibert, M Aufiero, M Brovchenko, S Delpech, V Ghetta, D Heuer, A Laureau, and E Merle-Lucotte. Molten salt fast reactors. In *Handbook of generation IV nuclear reactors*, pages 157–188. Elsevier, 2016.

[2] W B Cottrell, H E Hungerford, J K Leslie, and J L Meem. Operation of the aircraft reactor experiment.

[3] Eric Cervi. An innovative multiphysics modelling approach for the analysis and the development of the generation iv molten salt fast reactor. 2020.

[4] Jérôme Serp, Michel Allibert, Ondřej Beneš, Sylvie Delpech, Olga Feynberg, Véronique Ghetta, Daniel Heuer, David Holcomb, Victor Ignatiev, Jan Leen Kloosterman, et al. The molten salt reactor (MSR) in generation IV: overview and perspectives. *Progress in Nuclear Energy*, 77:308–319, 2014.

[5] GIF, 2017. Annual Report 2017, Available from:. `https://www.gen-4.org/gif/jcms/c_102083/gif-annual-report-2017-210918`.

[6] Generation IV International Forum. A Technology Roadmap for Generation IV Nuclear Energy Systems. 2002.

[7] Mariya Brovchenko, Elsa Merle Lucotte, Hervé Rouch, Fabio Alcaro, M Allibert, M Aufiero, Antonio Cammi, S Dulla, O Feynberg, L Frima, O Geoffroy, D Heuer, V Ignatiev, J.L. Kloosterman, D Lathouwers, A Laureau, L Luzzi, B Merk, P Ravetto, A Rineiski, P Rubiolo, L Rui, M Szieverth, S Wang, and B Yamaji. Optimization of the pre-conceptual design of the MSFR . 2013.

[8] SAMOFAR official website. `http://samofar.eu/`.

[9] SAMOSAFER official website. `https://samosafer.eu/`.

[10] Sylvie Delpech, Céline Cabet, Cyrine Slim, and Gérard S Picard. Molten fluorides for nuclear applications. *Materials Today*, 13(12):34–41, 2010.

[11] Manuele Aufiero. Development of advanced simulation tools for circulating fuel nuclear reactors. 2014.

[12] Eric Cervi, Stefano Lorenzi, Antonio Cammi, Lelio Luzzi, et al. An euler-euler multiphysics solver for the analysis of the helium bubbling system in the msfr. In *NENE 2017 26th International Conference Nuclear Energy for New Europe. Bled, Slovenia*, 2017.

[13] Davide Tartaglia. Numerical modelling and simulation of melting phenomena for freeze valves analysis in molten salt reactors. 2021.

[14] Jean C. Ragusa and Vijay S. Mahadevan. Consistent and accurate schemes for coupled neutronics thermal-hydraulics reactor analysis. *Nuclear Engineering and Design*, 239:566–579, 2009.

[15] Lelio Luzzi, Valentino Di Marcello, and Antonio Cammi. *Multi-Physics Approach to the modeling and analysis of Molten Salt Reactors*. Nova Science Publishers, Inc., 2012.

[16] Antonio Cammi, V Di Marcello, C Guerrieri, and Lelio Luzzi. Transfer function modeling of zero-power dynamics of circulating fuel reactors. *Journal of Engineering for Gas Turbines and Power*, 133(5), 2011.

[17] Carlo Fiorina, Danny Lathouwers, Manuele Aufiero, Antonio Cammi, Claudia Guerrieri, Jan Leen Kloosterman, Lelio Luzzi, and Marco Enrico Ricotti. Modelling and analysis of the msfr transient behaviour. *Annals of Nuclear Energy*, 64:485–498, 2014.

[18] Federico Caruggi. Multiphysics modelling approach for the analysis of xenon removal via helium bubbling in the molten salt fast reactor. 2021.

[19] Andrea Di Ronco, Stefano Lorenzi, Francesca Giacobbo, and Antonio Cammi. An eulerian single-phase transport model for solid fission products in the molten salt fast reactor: Development of an analytical solution for verification purposes. In *Frontiers in Energy Research*, 2021.

[20] Andrea Di Ronco, Stefano Lorenzi, Francesca Giacobbo, and Antonio Cammi. Multiphysics analysis of rans-based turbulent transport of solid fission products in the molten salt fast reactor. *Nuclear Engineering and Design*, 391:111739, 2022.

[21] Marco Tiberga, Rodrigo Gonzalez Gonzaga de Oliveira, Eric Cervi, Juan Antonio Blanco, Stefano Lorenzi, Manuele Aufiero, Danny Lathouwers, and Pablo Rubiolo. Results from a multi-physics numerical benchmark for codes dedicated to molten salt fast reactors. *Annals of Nuclear Energy*, 142:107428, 2020.

[22] A Santamarina, Dea Bernard, P Blaise, M Coste, A Courcelle, TD Huynh, C Jouanne, P Leconte, O Litaize, S Mengelle, et al. The jeff-3.1. 1 nuclear data library. *JEFF report*, 22(10.2):2, 2009.

[23] Jaakko Leppänen, Maria Pusa, Tuomas Viitanen, Ville Valtavirta, and Toni Kaltiaisenaho. The serpent monte carlo code: Status, development and applications in 2013. *Annals of Nuclear Energy*, 82:142–150, 2015.

[24] George I Bell and Samuel Glasstone. Nuclear reactor theory, van nostrand reinhold company. *New York,,* 1970.

[25] Vaughan R. Voller and Chittur Ramanathan Swaminathan. Eral source-based method for solidification phase change. *Numerical Heat Transfer Part B-fundamentals*, 19:175–189, 1991.

[26] OpenFOAM C++ Source Code Guide. `https://cpp.openfoam.org/v8/`.

[27] Carlo Fiorina. The molten salt fast reactor as a fast spectrum candidate for thorium implementation. 2013.

[28] Claudia Guerrieri, Manuele Aufiero, Antonio Cammi, Carlo Fiorina, and Lelio Luzzi. A preliminary study of the msfr dynamics. In *International Conference on Nuclear Engineering*, volume 44991, pages 229–238. American Society of Mechanical Engineers, 2012.

[29] D. Lathouwers, M. Tiberga, S. Lorenzi, A. Cammi, L. Luzzi, and J. L. Kloosterman. Definition and selection of transients. *Deliverable D4.1 of the SAMOFAR Project, Horizon 2020*, 2016.

[30] A. Cammi, E. Cervi, J. Krepel, D. Lathouwers, D. LeCarpentier, S. Lorenzi, M. Massone, R. de Oliveira, S. Poumerouly, A. Rineiski, M. Tiberga, and S. Wang. Analysis of accidental transients. *Deliverable D4.4 of the SAMOFAR Project, Horizon 2020*, 2017.

[31] E Il'ina, P Mushnikov, S Pershina, A Rudenko, A Redkin, Yu Zaikov, A Kholkina, and V Voronin. Thermal properties of lif-bef2 and lif-bef2-uf4 systems as applied to molten salt reactor technologies. *Journal of Molecular Liquids*, 344:117731, 2021.

[32] A Redkin, A Khudorozhkova, E Il'ina, S Pershina, P Mushnikov, A Isakov, Yu Zaikov, A Kataev, and M Laptev. Density and heat capacity of some molten mixtures in system lif-bef2-uf4. *Journal of Molecular Liquids*, 341:117215, 2021.

[33] N Hannoun, V Alexiades, and TZ Mai. A reference solution for phase change with

convection. *International Journal for Numerical Methods in Fluids*, 48(11):1283–1308, 2005.

[34] Henry G. Weller, Gavin R. Tabor, Hrvoje Jasak, and Christer Fureby. A tensorial approach to computational continuum mechanics using object-oriented techniques. *Computers in Physics*, 12:620–631, 1998.

A | Appendix A

The OpenFOAM library

Created by Henry Weller in 1989 under the name "FOAM", the Open-source Field Operation And Manipulation (OpenFOAM) [34] is a C++ library based on object-oriented programming, which exploits the Finite Volume Method (FVM). Its purpose is to spatially discretize and to solve partial differential equations, by means of interpolation and differencing schemes specified by the user. Thanks to its flexibility, it results suitable to face any kind of continuum mechanics problem, since it allows for proper handling of complex phenomena such as turbulence, chemical reactions, heat transfer, acoustics and solid mechanics or electromagnetics. This open-source software proved to be the ideal toolkit for implementing multiphysics models, ensuring the coupling of different physics through Picard iterations and solving with the segregated fashion strategy scalar and vector equations once at a time. Furthermore, the high-level C++ implementation of operators, which mimics their mathematical form, makes the code particularly straightforward for the user to visualise when it comes to enriching the problem with new constitutive equations to better represent the phenomena involved. As an example, it is reported the neutron diffusion equation for each energy group in mathematical description, Eq (A.1)):

$$\frac{1}{v}\frac{\partial \varphi}{\partial t} - \nabla \cdot (D\nabla\varphi) - (\chi_p(1-\beta_{tot})\nu\Sigma_f - (\Sigma_a + \Sigma_s))\varphi = neutron source \qquad (A.1)$$

and the respective OpenFOAM implementation:

```
(
fvm::ddt(invVel[i], fluxi)
- fvm::laplacian(D[i], fluxi)
- fvm::Sp(M[i], fluxi)
==
neutronSource[i]
);
```

where

```
M[i] = chiPrompt[i]*(1-precBetaTot)*Nu[i]*Sf[i] - (Sa[i] + Ssi);
```

where `M[i]` represents neutrons produced from fissions in i-th group minus neutrons removed, `neutronSource[i]` the contribution by other groups and by precursors, while `fluxi` stands for the neutron flux of i-th group.

B | Appendix B

As previously mentioned in Chapter 2, the multigroup diffusion approximation is implemented in the neutronic part of the simulations performed in this thesis, and six energy groups are considered for the neutronic flux. The parameters characterising these groups are reported in Table B.3 and they are evaluated through a Monte Carlo simulation adopting the reactor physics and burnup code SERPENT 2 and the JEFF-3.1.1 cross section library [30]. In addition, eight delayed neutron precursors and three decay heat precursors groups are assessed. Tables B.2 and B.1 show the decay constants and the fractions for both categories. Please note that the β coefficients related to the decay neutron precursors groups represent the fraction of decay power density for each group [12].

Group	β (-)	$\lambda\,(s^{-1})$
1	$1.86 \cdot 10^{-2}$	$3.580 \cdot 10^{-4}$
2	$1.29 \cdot 10^{-2}$	$1.680 \cdot 10^{-2}$
3	$1.17 \cdot 10^{-2}$	$1.973 \cdot 10^{-1}$

Table B.1: Decay constant and delayed neutron fraction for the 3 decay heat precursors groups.

Group	β (-)	$\lambda\,(s^{-1})$
1	$1.22426 \cdot 10^{-4}$	$1.24667 \cdot 10^{-2}$
2	$7.57005 \cdot 10^{-4}$	$2.82917 \cdot 10^{-2}$
3	$3.76047 \cdot 10^{-4}$	$4.25244 \cdot 10^{-2}$
4	$8.13656 \cdot 10^{-4}$	$1.33042 \cdot 10^{-1}$
5	$1.47910 \cdot 10^{-3}$	$2.92467 \cdot 10^{-1}$
6	$5.19854 \cdot 10^{-4}$	$6.66488 \cdot 10^{-1}$
7	$4.62852 \cdot 10^{-4}$	1.63478
8	$1.57447 \cdot 10^{-4}$	3.55460

Table B.2: Decay constant and delayed neutron fraction for the 8 delayed neutron precursors groups.

Group	Energy range MeV		Diffusion coefficient D_g m	Inverse neutron speed $1/v_g$ s/m
1	20	2.23	$2.31456 \cdot 10^{-2}$	$3.98114 \cdot 10^{-8}$
2	2.23	$4.98 \cdot 10^{-1}$	$1.53990 \cdot 10^{-2}$	$7.52053 \cdot 10^{-8}$
3	$4.98 \cdot 10^{-1}$	$2.48 \cdot 10^{-2}$	$9.75996 \cdot 10^{-3}$	$2.68798 \cdot 10^{-7}$
4	$2.48 \cdot 10^{-2}$	$5.45 \cdot 10^{-3}$	$1.18004 \cdot 10^{-2}$	$6.62039 \cdot 10^{7}$
5	$5.45 \cdot 10^{-3}$	$7.49 \cdot 10^{-4}$	$1.10261 \cdot 10^{-2}$	$1.49469 \cdot 10^{-6}$
6	$7.49 \cdot 10^{-4}$	0	$1.02629 \cdot 10^{-2}$	$3.65757 \cdot 10^{-6}$

Table B.3: Energy range, diffusion coefficient and inverse of neutron speed for each of the six group of the multrigroup diffusion approximation.

List of Figures

List of Tables

List of Symbols

Greek symbols

Variable	Description	SI unit
α	Thermal diffusivity	$m^2\,s^{-1}$
α_g	Albedo coefficient for g^{th} group	-
$\alpha_{thermal}$	Thermal feedback coefficient	$pcm\,K^{-1}$
β	Neutron fraction	-
β_t	Thermal expansion coefficient	K^{-1}
γ	Heat source parameter	$W\,m^{-3}\,K^{-1}$
λ	Decay constant	s^{-1}
μ	Dynamic viscosity	$Pa\,s$
ν	Kinematic viscosity	$m^2\,s^{-1}$
$\bar{\nu}$	Mean number of neutron per fission	-
ρ	Density	$kg\,m^{-3}$
ϱ	Reactivity	pcm
Σ	Macroscopic cross section	m^{-1}
ϕ	Volumetric face flux	$m^3\,s^{-1}$
φ	Neutron flux	$m^{-2}\,s^{-1}$
χ	Neutron yield	-

Latin symbols

Variable	Description	SI unit
A	Cross section coefficient	-
c	Delayed neutron precursors concentration	m^{-3}
c_p	Specific heat capacity	$J\,kg^{-1}\,K^{-1}$
C	Darcy source term constant	m^{-2}
d	Decay heat precursors concentration	$J\,m^{-3}$
D	Neutron diffusion coefficient	m
$\bar{E}$	Average energy released per fission	J
f	Mass liquid fraction	-
g	Volume liquid fraction	-
$\boldsymbol{g}$	Gravitational acceleration	$m\,s^{-2}$
h	Specific enthalpy	$J\,kg^{-1}$
H	Volumetric enthalpy	$J\,m^{-3}$
k	Thermal conductivity	$W\,m^{-1}\,K^{-1}$
k_{eff}	Effective multiplication factor	-
L	Latent heat of fusion	$J\,kg^{-1}$
p	Pressure	Pa
Q	Total power	W
q	Volumetric power source	$W\,m^{-3}$
$\boldsymbol{u}$	Velocity	$m\,s^{-1}$
t	Time	s
T	Temperature	K
Pr	Prandtl number	-
Re	Reynolds number	-
S	Neutron source	$m^{-3}\,s^{-1}$
Sc	Schmidt number	-
$\dot{V}$	Volumetric flowrate	$m^3\,s^{-1}$
v_g	Neutron group velocity	$m\,s^{-1}$